DESIGN OF SPECTRALLY SELECTIVE SURFACES

by

MUHAMMED ALİ KEÇEBAŞ

Submitted to the Graduate School of Sabanci Univesity in partial fulfilment of the requirements for the degree of Doctor of Philosophy

Sabancı University

August 2020

ENGINEERING OF THE ELECTROMAGNETIC SPECTRUM FOR BROADBAND APPLICATIONS

APPROVED BY:

Prof. Dr. Kürşat Şendur
(Thesis Supervisor)

Prof. Dr. Ali Koşar

Prof. Dr. Burç Mısırlıoğlu

Prof. Dr. Hakan Ertürk

Prof. Dr. Pınar Mengüç

DATE OF APPROVAL: 17/08/2020

ABSTRACT

ENGINEERING OF THE ELECTROMAGNETIC SPECTRUM IN BROADBAND FOR ENERGY APPLICATIONS

Muhammed Ali Keçebaş

PhD Thesis, August 2020

Supervisor: Prof. Dr. İbrahim Kürşat Şendur

Keywords: electromagnetic spectrum, radiative cooling, adjoint method, black silicon

Tailoring the spectral reflection, absorption, and transmission of the surfaces, as well as their emission, in broadband has been attracted great attention with the recent advancements in micro/nanotechnology. Such advancements provide the opportunity of realizing structures that are comparable to wavelength in terms of geometrical dimensions, which allow manipulation of incident or emitted waves from visible to infrared spectrum in small scale. Therefore, understanding the physical mechanisms that are responsible from altered spectral behaviors achieved by various type of optical filters/coatings and designing those become equally important. Aim of this thesis is to propose design methods to selected energy and thermal applications, including daytime passive radiative cooling, broadband reflectance with refractory metals, absorption mechanisms of black silicon and high temperature broadband thermal emitter, all of which require engineering of electromagnetic spectrum in broadband. Various phenomena are considered during the design stages and utilized to evaluate the resulting characteristics. Methods used in this thesis generate novel designs to be considered in various applications.

ÖZET

TAYFSAL OLARAK SEÇİCİ YÜZEYLERİN TASARIMI

Muhammed Ali Keçebaş

Doktora Tezi, Ağustos 2020

Tez Danışmanı: İbrahim Kürşat Şendur

Anahtar Kelimeler: Elektromanyetik tayf, siyah silikon, ışınımsal soğutma, adjoint metodu

Son yıllarda mikro/nano teknolojideki gelişmelerle birlikte yüzeylerin geniş bantta tayfsal yansıma, emilim, iletim ve yayınım davranışlarının mühendisliğinin yapılmasına olan ilgi çok artmıştır. Bu gelişmeler, geometrik boyutları ilgilenilen dalga boyuna yakın olan yapıların mühendisliğine olanak sağlamış olup, görülebilir ve kızılötesi tayfalarda gelen veya yayılan dalgalara karşı yüzeylerin davranışlarının şekillendirilmesine imkan vermiştir. Bu sebeple, yüzeyin tayfsal cevaplarını değiştiren farklı tip optik filtreler ve kaplamaların tasarımı ve ilgili mekanizmaların anlaşılması da aynı derecede önem kazanmıştır. Bu tezin amacı, pasif ışınımsal soğutma, dayanıklı metallerle geniş bantlı yansıma elde edilmesi, siyah silikon'un emilim mekanizmaları ve yüksek sıcaklıklı geniş bantlı yayıcılar, gibi geniş bantta tayfsal mühendislik gerektiren seçili enerji ve termal uygulamaları için farklı tasarım yöntemleri önermektir. Tasarım ve analiz aşamalarında, farklı elektromanyetik mekanizmaların etkileri düşünülüp, sonuçlara olan etkileri incelenmiştir. Bu tezde kullanılan yöntemler, seçili uygulamalar için yenilikçi tasarımlar önermektedir.

To My Family,

TABLE OF CONTENTS

LIST OF FIGURES

LIST OF TABLES

1. INTRODUCTION

1.1 Background & Motivation

Thanks to advances in nanotechnology, engineering of spectral behaviors by using various type of structures and coatings has been possible over the past decades [1]–[3]. Recent studies show that it is possible to control the spectral behaviors of surfaces by utilizing thin-film layers [4], [5] or nanostructures [6]–[10]. Such engineered structures are widely used in various applications including passive radiative cooling [11]–[16], thermophotovoltaics [17], [18] and solar-thermophotovoltaics [19], [20]. Different spectral requirements demanded by these different applications determines the properties of the coatings. These properties are determined by the several factors, such as aim of the coatings and operating conditions. Among many other, thermal radiation is one of the most important factors for the determination of spectral requirements for energy applications [21]. Spectral distribution of thermal radiation determines the wavelength of interests for any application. Thermal radiation is mathematically expressed via Planck's formula [22] which includes temperature and wavelength dependence of it. Thermal radiation intensity at different temperatures over the electromagnetic spectrum is depicted in Fig. 1.1.

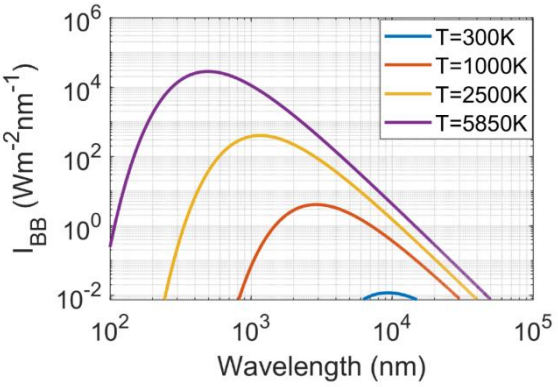

Figure 1.1. Blackbody radiation at different temperatures with respect to wavelength

As demonstrated in Fig. 1.1, with increasing temperature peak value of thermal radiation shifts toward shorter wavelengths. For instance, peak radiation for an object with temperature around 5850 K (which is the approximate temperature of the sun) is around 500 nm, whereas it is around 10 μm for an object with temperature around 300 K. In addition, objects with higher temperatures have higher radiation intensity in broadband spectrum when compared to radiation intensity of objects with lower temperatures. Based on these, spectral requirements are determined, e.g. solar collectors should absorb incident radiation around 500 nm where solar irradiance has high intensity or to radiate heat away from the surfaces which are at temperatures around 300 K coatings should be designed to engineer spectral behaviors around 10 μm spectrum. Therefore, it is important to understand the distribution of thermal radiation, which is a crucial factor for the determination of the coatings' spectrum of interest in applications where radiative heat transfer is the dominant mode for heat exchange.

In several applications, e.g. energy, either reflecting incident radiation, removal of heat for cooling or absorption of the incident power for heating purposes are of interest. Depending on the application and corresponding conditions, either conduction, convection or radiation heat transfer becomes the dominant mode of the heat transfer. In solar/thermophotovoltaic or aerospace applications, radiative transfer becomes a significant mode of interest, therefore thermal radiation and its interaction with the systems become important. Thermal radiation is linked to spectral behaviors with Kirchhoff's law of absorption which relates emittance and absorptance. The most important implication of this relationship is the fact that by engineering the spectral absorptivity of the surfaces, which is based on interaction of electromagnetic waves with the surfaces, rate of radiative heat transfer between objects can be altered. For example, increased reflectance on a surface prevents the absorption by the structure therefore reduces the heat dissipation and prevents temperature increase. On the contrary, reduced reflectance and increased absorption of the incident power results in temperature increase, which is essential in radiative heating applications. Therefore, good control of thermal radiation results in increased efficiency in the systems and reductions in maintenance costs due to extended lifetime of the components by reducing the thermal loads.

In addition to thermal applications, high emission is also desired in photodiodes [23-26] and photodetector [27-28] applications. Demand for broadband high emission/absorption in such applications results in extensive research to develop structures that highly absorbs/emits in broadband spectrum. Various type of structures is reported in the literature that exhibits high absorption/emission in broadband spectrum especially with silicon [29-34] due to its

applicability in practical devices. Parallel to the progress in the field, understanding the origins of the broadband absorption/emission in these structures becomes equally important to design superior structures. However, explanation of the fundamental mechanisms for broadband absorption in silicon requires detailed electromagnetic analysis.

As mentioned above, coatings are used to shape the spectral characteristics of the surfaces. Due to the wide variety of promising applications, some of which briefly summarized above, design and analysis of coatings become extremely important. Coatings can be categorized as homogeneous and inhomogeneous in terms of their structure. Homogeneous coatings are generally in the form of films which covers the entire surface, whereas inhomogeneous coatings are distributed on the surface either randomly or with a pattern. In general, homogeneous coatings alter the spectral response of the surfaces, on which they are coated, by collective responses of multilayer films. By adjusting thicknesses of the layers, phases of resulting waves from the interaction of incident waves with individual layers can be altered. These resulting waves with different phases interfere with each other either constructively or deconstructively. These interference effects are the fundamental mechanism that alter the spectral response of the structures. Depending on these interference effects, highly reflective, in narrowband or broadband, filters can be designed. Inhomogeneous coatings on the other hand, in general, are not multilayer structures and interference effects are not the fundamental mechanism in their responses. Inhomogeneous structures generally coated on the surface with a periodicity to excite certain resonance modes. Due to this resonant nature, they are excellent for narrowband applications which demand selective spectral characteristics. By tuning the periodicity or pattern geometry bandwidth or central wavelength of the resonance modes can be tuned. In addition to spectral characteristics of coatings, their thermomechanical characteristics are also important depending on the operating conditions.

Both homogenous and inhomogeneous type of coatings can be designed for optical/thermal applications once wavelengths of interest are determined. Design and analysis of the coatings are of great importance in daytime passive radiative cooling, broadband reflectance with refractory materials, black silicon, and high temperature broadband thermal emitters. All these applications require different spectral characteristics in broadband spectrum. Material constraint also come into the picture in the structures with refractory metals and high temperature broadband thermal emitters due to the operating conditions. Although several studies have been reported in the literature related to these subjects, there are still points which should be explored. In this dissertation, design and analysis methods are proposed and tested

for the selected applications with both homogenous and inhomogeneous type of filters in which material requirements are also considered. Proposed methods throughout the dissertation are proven to be effective solutions to the selected problems and can be adapted to different coating design problems.

1.2. Literature Survey

In this section, related literature for the selected problems described in the previous sections are given. With the literature survey, missing points in the related literature are summarized and possible solutions are described which are studied in this dissertation.

1.2.1. Passive Radiative Cooling

Undesired heating of many semiconductor devices, either due to the energy they generate or due to their heating by external heat sources, is detrimental for their performance. One of the significant sources of heating in an open environment is the solar irradiance, which causes undesired heating on solar cells, or, at much larger scale, the buildings themselves [35-36]. Alternative to an active cooling technique, passive radiative cooling can achieve cooling of objects even below ambient temperature [11]. Passive radiative cooling designs are based on tailoring the spectral emission and absorption at different wavelength intervals. These approaches can be divided into nighttime or daytime cooling design concepts based on the targeted operation times. Radiative cooling for nighttime operations has been studied extensively in the literature and high cooling performances were reported [37-43]. This is achieved by increasing emission in the 8-13 μm spectrum, where atmosphere is transparent and radiation from terrestrial objects is maximum. The 8-13 μm spectral transparency window allows radiative heat transfer between sky and objects, and therefore, provides opportunities for effective passive radiative cooling.

However, emission in atmospheric transparency window located in 8-13 μm spectrum interval is not sufficient to achieve radiative cooling below ambient air temperature during daytime. Due to the presence of incident solar irradiation, which is strong in the visible and near-infrared spectrums, radiative daytime cooling requires effective reflection of incident solar radiation in those spectrums. Previous designs use a foil made of ZnS, ZnSe or polymers and pigments, which has high reflection in the solar spectrum (visible and near infrared), and still able to achieve an emission in the 8-13 μm spectrum for cooling. However, radiative cooling below ambient could not be achieved in those designs, since overall reflection in the solar spectrum is reported to be below %85 percentage, which results in a higher absorption of the solar irradiance in the visible and near-infrared spectrums compared to thermal emission to sky in the 8-13 μm spectrum. To achieve a successful passive cooling, the reflection in the visible and near-infrared spectrums should be above % 90-95 percentage. By doing so, absorption of the solar irradiance in the visible and near-infrared spectrums can be balanced by thermal emission in the 8-13 μm spectrum.

In addition to these, negative contributions from atmospheric thermal radiation should also be reflected to achieve radiative cooling which is strong at wavelengths at which atmosphere is transparent. Therefore, for daytime passive radiative cooling a surface should be non-emitting (zero emittance and absorptance) at wavelengths shorter than 8 μm, and highly emitting (up to 100% emittance) in the atmospheric transparency window, i.e., between the 8-13 μm wavelength range. These stringent requirements are satisfied experimentally for the first time and reported in [11], where radiative cooling potential below ambient air temperature of a coating under direct sunlight is proven for the first time. After that point, several types of coatings are developed which achieve radiative cooling during daytime under the presence of significant solar irradiance. Single layer films, nanoparticles and photonic crystal or metamaterial type of radiative cooling devices are some examples. All type of coatings may benefit from different phenomena and utilize different materials.

The simplest type of coatings composed of films are the ones coated on top of back reflector. While coated single layer of material absorbs, therefore emits, thermal radiation at mid-infrared spectra and transmitted, solar irradiance is reflected by the metallic reflector. Optical characteristics of the coated material is crucial in these types of devices. They should have high emittance in atmospheric transparency windows, while having very low absorption at other wavelengths. Coatings based on polymers like poly-dimethylsiloxane (PDMS) [44] and polyethylene terephthalate (PET) [45] are tested and their radiative cooling potential is demonstrated. However, large scale application and durability of these type of coatings should also be studied for real time applications. In addition to polymer films,

silicon-based films are also reported for passive radiative cooling. For this purpose, SiO, SiO_2, SiC and Si_3N_4 are considered in radiative cooling devices. SiO [38-39,46], Si_3N_4 [47] and $SiO_{0.6}N_{0.2}$ [48] films and radiative cooling potential is reported.

By the aid of nanoparticles, higher radiative cooling performances compared to bulk films are achieved. When particles like SiO_2, TiO_2 or SiC. When these particles are doped in films composed of polymers or other type of materials, selective emission that lead to radiative cooling occurs. Several examples of these type of coatings are reported in the literature with varying material configurations [49-51]. High reflection requirement is usually achieved by a metallic back reflector in these types of structures and emissive layers that contains particles are selected among non-absorbing materials in visible and near-infrared spectra.

In addition to particle based or single layer films, photonic structures composed of multilayer thin-films and patterned surfaces are also utilized for passive radiative cooling, thanks to advancements in nano/microtechnology [1-3]. Generally, designed thin-film filters composed of different layers with varying optical properties and thicknesses [11, 16, 52-53]. Different optimization methods are adapted to design thin-film coatings for passive radiative cooling [54-57]. Unless the sensitivity of the spectral emissivity to layer thicknesses is low, these types of structures can be heavily utilized. Finally, patterned surfaces composed of air holes [58] and triangles [14,59] are developed. Such patterned surfaces are also combined with multilayer structures [12, 60], which exhibit selective emission very close to ideal profile. Although elevated performance with these kinds of sophisticated topologies are achieved, difficulties in the fabrication steps may restrict their use in applications.

Several review papers have outlined the current progress in the field of daytime passive radiative cooling concepts are published in the literature [36,48,61-64]. In addition to design and performance evaluations, applicability of daytime passive radiative cooling in different application areas, e.g. thermal management in buildings [65-69] and thermophotovoltaics [70-72], are also reported.

Despite the extensive literature and promising results in the field of daytime passive radiative cooling, every proposed design methodology considers the problem as a purely spectral problem and ignores radiative aspects of the problem during the design stage. A new method which considers the both aspects of the problem will make a significant contribution to the literature. Such new method can be utilized to design thin-film optical filters specifically for daytime passive radiative cooling.

It is well known that interaction between the incident wave and thin-film system is significantly affected by the number of layers and material composition of individual layers. Previously reported thin film structures for daytime passive radiative cooling have been

designed by different approaches, which consider various parameters as design variables. Two major studies in this field [11, 73] utilize numerical optimization techniques essential for designing thin film filters for different applications. The goal of these approaches is to minimize the error between given and actual spectral behavior in the broadband spectrum. However, daytime passive radiative cooling is not purely a spectral problem and needs to be coupled to radiative heat transfer. Therefore, considering it as a spectral problem only results in an under-defined problem definition. For a more well-defined problem, the effects of spectral behavior on thermal radiation should be included in the problem definition. To address this need, a reformulated the daytime passive radiative cooling problem in which the effects of both the spectral and thermal parts are included, is required. Once implemented, developed methodology results in higher cooling powers and temperature reduction rates compared to previously reported thin-film design approaches. Obtained results show that considering the impact of spectral distribution on radiative transfer mechanisms, which determine the cooling power, lead to elevated performance. All the results are also interpreted by wave impedance analysis which supports spectral selectivity. Overall, proposed method shows the importance of specific design method for daytime passive radiative cooling.

1.2.2. Broadband Reflectance with Refractory Metals

Refractory metals, including Tungsten, Tantalum, Molybdenum and Niobium, are known for their good thermomechanical properties. Various applications require operations in extreme environments, where refractory metals can benefit the devices to withstand against thermally and mechanically harsh conditions. Among these applications, hypersonic applications [74-76], space applications [77], and solar/thermophotovoltaics [19, 78] are the most notable ones in which extreme temperature are observed. In addition to these applications, the absorption of the incident infrared radiation, which results in a temperature increase, is undesired in large infrared telescopes [79-80] and night-vision systems [81]. Absorption of the incident radiation in these applications brings thermal load to the system, therefore, thermal and mechanical damage can be observed. This damage in system components degrade the device performance due to heat dissipation in the components. To overcome such issues, reflectors that are composed of Al or Ag are utilized with protective coatings [82-86]. However, problems like adhesion, corrosion, durability and degraded reflectance performance due to damages are some

issues that are encountered in these coatings [83-84,86]. A possible solution to these issues is to use metals with higher hardness, also known as refractory metals. Although spectral behavior of W, which belongs to the family of refractory metals, is widely studied for high emissivity applications [87-88] and its oxide form for electrochromic applications [89-90], it is not widely studied for applications which demand broadband high reflectance.

For effective use in extreme environments, engineering the broadband reflection spectrum of surfaces composed of refractory metals is of great interest. A particular problem for aerospace materials in extreme environments is the exposure to high levels of infrared radiation. If absorbed, the incident radiation in aerospace materials creates high levels of heating, which can create structural and stability problems in materials. For radiative heating, broadband sources such as solar irradiance plays an important role in extreme environments. Solar radiation peaks around 500 nm, and it is strong in 300 – 3000 nm spectrum. Beyond 3000 nm, radiated power degrades and becomes relatively low [91]. For materials with high absorption in the spectral range of sources which radiate at visible and infrared spectrums, large temperatures and thermal stresses can occur. To overcome this problem, a detailed understanding of optical coatings, composed of thin-films, which impact the interaction of visible and infrared radiation with refractory metals is essential both to control/minimize the impact of the absorbed radiation and to design surfaces. Advances in nanotechnology which enables manipulation of electromagnetic waves at the visible and near-infrared spectrums, 2D and 3D optical filters are widely used to engineer spectral characteristics of the surfaces [92-96]. High emissivity coatings are widely studied, and results are reported in the literature [97-99]. In recent years, Ag is heavily utilized as broadband reflector for day time radiative cooling applications [11-12,16,100], due to its intrinsic broadband reflection in visible and near-infrared spectrums. Good reflectors in the visible spectrum, such as Ag, have relatively low Young's modulus and melting point.

Metals are widely used as solar irradiance reflectors [101-102], since they are intrinsically good and broadband reflectors in the visible and near-infrared spectra. Although metals like Ag, Au, Al or Cu are good reflectors in the visible and near-infrared spectra, they have relatively low melting points and Young's modules, whereas it is opposite for refractory metals such as W, Ta, Mo and Nb [103]. Despite their attractive thermomechanical properties, spectral reflectivity of these refractory metals cause setbacks for use in extreme environments. As we will discuss later in the manuscript, the reflectivity of the refractory metals in 1500-3000 nm spectrum is above 95% in average, whereas it is around 40% -50% range in 300-1500 nm

spectrum. Such low reflectivity in 300-1500 nm spectrum gives rise to increase of temperature, since a significant portion of the solar irradiance exists in the 300-1500 nm spectrum.

In the literature, there are several thin-film optical filter design approaches to engineer the spectral responses of the objects [54,73,104-106]. Materials, optical properties, and layer thicknesses are the main design parameters and are determined depending on the application. Essence of the design studies is to create the desired interference between the layers. Performance of the designed filter is highly influenced by the dielectric layers, arrangement of layers and layer thicknesses. Various filters with different material combinations can be developed and analyzed.

To generate high reflection in broadband spectrum individual periodic high-low index layers, which generate high reflection around a wavelength, are designed at different wavelengths and stacked together. Due to the low destructive interference of the reflected beams at the front surface, broadband reflection is achieved over the spectrum. Although sharp peaks at distinct wavelengths are observed over the spectra, they do not lead to reduction in reflection in broadband spectrum. Underlying mechanisms of resulting sharp peaks are explained with Fabry-Perot resonators. Effect of material properties on reflection is also studied. Overall, this study proposes structures that exhibits very high reflection in broadband spectrum, which can be used in aerospace applications, thermal management and thermophotovoltaics.

1..2.3. Black Silicon

Silicon devices with high absorptivity is heavily utilized in various applications of photonics including photodiodes [23-26], photodetectors [27-28, 107] and solar cells [108-112]. Demand for high absorptivity in these applications attracts the attention of the researchers, and therefore lead to various type of silicon based photonic structures with high absorptivity, which are also known as black silicon [29-30]. In the literature, black silicon is achieved by introducing geometrical textures on the surface of silicon. Although high absorptivity over a broad spectral band is reported with surfaces with various textures, the underlying physical mechanisms that lead to high broadband absorptivity, is still an area that requires further research.

Black silicon with high absorptivity in the 0.5 – 2.5 um spectrum band is demonstrated [29] for the first time by fabricating the surface textures using reactive ion etching (RIE). Random surface texture occurs as a result of the RIE process for silicon. Up to 90% percentage absorptivity is reported in the specified spectrum with generated random texture. Enhanced absorption is attributed to the increased light trapping effect due to the spikes with high depth to width ratio. A major drawback of the structures fabricated by RIE is the damaged surface by the laser irradiation. Damage and structural defects result in reduced electronic properties, thus affect the performance of the final design. Later, extensive reviews are reported in the literature, which summarize the progress made on micro/nano-structured black silicon [30-34]. While abundant several studies exist in the literature regarding the experiments and fabrication techniques for micro-structured black silicon [113-126], fundamental physical mechanisms that yields this behavior have not been equally investigated. Scattering characteristics of electromagnetic waves from such random rough surfaces for various applications have been studied in the literature. These studies include communication over rough ocean surfaces [117-118], remote sensing applications involving terrestrial applications and buried objects [119-120], surface texturing in solar cells [121-122], and surface plasmon excitation with rough surfaces [123-125]. Despite this established literature on rough surface scattering from surfaces, surface roughness effects leading to broadband absorption in black silicon have been largely ignored. In [126], response of the random texture is analyzed by calculating the field distribution of periodically arranged surface texture. Strong correlation between the absorptivity of the random and periodic textures are observed and enhanced absorptivity is attributed to increased field intensity in the geometry. However, underlying mechanisms responsible from high field intensity are not explored.

There are several publications for surfaces with deterministic textures for absorption/emission enhancement. In recent years, with the advancements in nanotechnology, periodically arranged surface textures are heavily utilized in the field of photonics due to the capability of resonance excitement. Plasmonic resonance effects in silicon in mid-infrared wavelengths is demonstrated for bio-sensing applications [127]. Frequency selective structures composed of silicon is also reported for mid-infrared applications [128-129]. Issue with these structures suffer from low bandwidth of absorption due to resonant based nature. To overcome low bandwidth issue, different structures that combines multi-resonances together are studied in the literature [130-133]. However, those structures suffer from reduced absorption efficiency due to the destructive interference of different resonance modes. Besides the mid-infrared

applications, periodically arranged surface textures are also developed for applications in visible and near-infrared spectrums [134-137]. In [134], structures are capable of strongly trapping the light in silicon for solar cell applications. Another study [135] proposed a hybrid structure, which sandwiches silicon structure between a polymer and a textured gold layer. Hybrid structure traps the light inside the silicon very effectively, thus resulting in high absorption in 0.3 -2 um interval reaching up to 90 % levels. However due to the hybrid nature, such structure requires several fabrication steps which makes it less feasible for fabrication. Black silicon devices composed of periodically arranged textures, for which some of the examples are given above, owe the absorptance enhancement to the field enhancement inside the silicon. High field enhancements in these devices are either attributed to resonance or light trapping effects due to sandwiched silicon. However, physics of the field enhancement in pure silicon structure, which neither support plasmonic resonances nor benefit from multiple reflections, is not clarified. Absorptance spectra of triangle like textures composed of pure silicon is approximated by a multilayer structure with effective medium theory in [136]. Although computational results well agree with the experimental results, such approach does not able to explain the underlying physics. It shows that absorptance spectra of periodic surface textures can be mimicked with a multilayer structure which benefits from destructive interference of the reflected beams on the front surface.

To analyze the physical mechanisms occurring in black silicon, electromagnetic characteristics of field distributions on random and deterministic textures are studied. Effect of doping concentration and geometrical parameters of the textures are studied in this thesis. With the aid of detailed analysis, it is found out that two separate electromagnetic phenomena occur inside the textures, which give rise to enhanced field intensity and therefore elevated absorption. Occurrence condition for these are studied. Results reveal that width of the individual textures play a crucial role in the absorption characteristics. Obtain findings shed a light on the origins of the broadband absorption in black silicon.

1.2.4. Broadband Thermal Emitter/Absorber & Inverse Design

Tailoring thermal emission spectra has attracted great attention due to its promising outcomes in energy harvesting [138-139], thermal camouflage [140-141] and sensor applications [142]. Among energy applications, recent advancements in thermophotovoltaics [5,17], solar absorbers/reflectors [87, 143-144] lead to increase in demand for thermal emitters operating in either narrowband or broadband spectrum. Metamaterials [145-147] and photonic crystals [148-149] are widely utilized to address this demand. Plasmonics are among one of the most favorable phenomena to design thermal emitters in visible [150-151] and infrared spectrums [152]. In addition, highly emitting thin-film structures based on interference effects in the mid-infrared spectrum are reported with recent advancements in daytime passive radiative cooling [11,16]. Epsilon-near-zero (ENZ) and epsilon-near-pole (ENP) phenomena are also widely studied, and their potential as thermal emitters/absorbers are also demonstrated [78, 153-154]. To make such phenomena to occur, deterministic textures/patterns are utilized for which some examples given above. In recent years, inverse design methods have been also adapted in electromagnetics to design superior and non-intuitive devices with more sophisticated topology [155-157].

Although there are various types of inverse design methods, belongs to category of heuristic [158-160] and gradient-based [161] optimization, adjoint method is one of the most favorable one among others [162-164]. Efficient calculation of the gradient with adjoint method, 2 simulations per iteration, allows to end up with designs in a much shorter time frame. Advantage of this method becomes prominent when there exist large number of design variables in the system. Although topology optimization with adjoint method is applied in various type of electromagnetic problems, including couplers [162,165-166], splitters [167] and non-linear devices [168-169], it is not applied to high temperature thermal emitters which should have high emission in broadband spectrum. However, besides the high emission/absorption behavior in broadband spectrum, high temperature stability requirement appears in high temperature applications [170]. Therefore, material selection becomes a higher priority, and this leads to attempts of designing high emitters composed of thermomechanically superior materials. For this purpose, III-IV A compounds are highly considered in coatings due to their excellent thermomechanical properties [171-173]. Among many other alternatives, various forms of ZrB_2, which belongs to family of ultra-high temperature ceramics, is studied to be used as high temperature emitters.

ZrB_2 is known in the literature by its high melting point, oxidation and ablation resistance, chemical reactivity and erosion resistance [174-175]. These characteristics make ZrB_2 a great candidate for coatings that should remain stable in extreme operating conditions. However, its emission in visible and near-infrared spectra requires enhancement to be used as a high temperature thermal emitter/absorber [176]. Emission of ZrB_2 is significantly enhanced by mixing and doping [177] and effect of rare-earth dopants also shown to be improving the emission rates while preserving thermomechanical stability [178-179] However, emission improvement by exciting electromagnetic phenomena supported due to optical properties of ZrB_2 has been largely ignored.

Dispersive characteristics and sign change in the dielectric function of ZrB_2 [176], from positive to negative, allows exciting different phenomena including ENZ/ENP and plasmonic modes. In this study, broadband thermal emitters/absorbers in 0.3-3 μm spectrum composed of ZrB_2 designed by adjoint based topology optimization are demonstrated. First, emission/absorption of periodically arranged rectangular gratings are evaluated and considered as initial intuitive designs. Initial structures exhibit nearly 65% emission/absorption in 0.3-3 μm spectrum with distinct peaks around 0.7 and 1 μm for which underlying mechanisms are analyzed. Variations in interested spectrum with changing geometrical dimensions are also reported. Next, initial designs are fed to adjoint based inverse design algorithm and topology optimization is conducted in 3D to increase emission/absorption in broadband spectrum. Resulting structures yield elevated emission by 20-25% in broadband spectrum, which cannot be achieved by a simpler topology. Our results show that textured ZrB_2 surface exhibits high emission in broadband spectra, comparable to the ones obtained by mixing and doping, which can be utilized as high temperature broadband thermal emitters.

1.3 Aims & Objectives

Main aim of this thesis is the broadband engineering of spectral characteristics of the surfaces for the selected applications. Various methods are used/proposed to design structures which combines the material properties and geometry of the coatings. Selected applications and contributions to the related field are given and briefly summarized:

- Daytime passive radiative cooling: Daytime passive radiative cooling is widely studied and various type of coatings have been proposed for this application. Several methods and optimization techniques are adapted to daytime passive radiative cooling problem which were previously used to design coatings. Although promising results were obtained with those methods, further improvements can be achieved with more sophisticated design methods developed specifically for this problem. Therefore, in this thesis, a design method with thin-film structures which considers both spectral and radiative aspects of the daytime passive radiative cooling problem during the design stage, differently from previous methods which only consider spectral aspect of the problem are intend to be developed.
- Broadband reflectance with refractory metals: Refractory metals are of great interest for applications in extreme environments, which require durable coatings. Although durable coatings with such materials are studied for high emission/absorption, especially for thermophotovoltaic applications, broadband reflectors with such materials are not widely studied. Such broadband reflectors are required in applications in which high thermal stresses occur due to absorption of incident radiation. To address this need, I study design of coatings composed of refractory metals which have high reflection in broadband spectrum.
- Black silicon: Although black silicon is proven to be broadband emitter/absorber in broadband spectrum, the fundamental mechanisms that are responsible from such behavior are not reported. Therefore, in this thesis, analysis of the fundamental mechanisms rather than a design approach for black silicon is considered.
- High temperature broadband thermal emitter: Broadband high temperature thermal emitters/absorbers are of great interest for applications in thermal management to energy harvesting. In these type of coatings thermomechanical characteristics of the coating is as important as its spectral characteristics. Therefore, there is an increasing attempt to design coatings with excellent thermomechanical properties. ZrB_2, which belong to family of ultra-high-temperature-ceramics, is one of those materials which have excellent thermomechanical properties. Although its emission characteristics is previously studied with different dopants, its emission as an inhomogeneous coating is not studied. To design such a coating, a recently proposed gradient based optimization method, adjoint based topology optimization, is adapted. With this study, the potential

of ZrB_2 as a thermal emitter in broadband spectrum as well as the impact of adjoint based optimization on broadband emitter design will be explored.

1.4 Contributions

This dissertation contributes to the field of absorption, thermal emission and reflection control which can be considered as a sub-category of photonics. Specifically, it introduces novel design approaches, and provides explanations to the resulting behaviors, for the field of optical coatings for energy harvesting, thermal management and nanophotonics. Solutions proposed to different problems and their contribution to the corresponding field is briefly summarized below:

- Daytime Passive Radiative Cooling: A design methodology with thin-films for daytime passive radiative cooling is implemented which carry out thickness optimization of the selected layers. Main difference of the proposed approach from the previous techniques is its problem formulation. Previous optimization techniques are based on minimizing the error between a pre-determined ideal spectral emissivity/absorptivity and actual emissivity/absorptivity profiles. Those approaches evaluate the cooling power and temperature reduction performances after the optimization. In the proposed approach, cooling power evaluation is embedded in the problem formulation and optimization is carried out such that cooling power is maximized, which is the main goal of the daytime passive radiative cooling. Since both spectral and radiative dynamics are considered during the design stage, higher cooling powers and temperature reduction rates are achieved, and comparisons are demonstrated in this thesis. Therefore, proposed method can be used to design passive radiative cooling coatings composed of thin-films with enhanced cooling powers.
- Broadband reflectance with refractory metals: Periodic high-low index segments, which generate high reflection around a central wavelength are stacked together and utilized to generate high reflection in visible and near-infrared spectra. Although individual segments for high reflection is widely utilized, stacking multiple segments to enhance reflection of refractory metals in broadband spectrum has not been studied. Reported results show that very high reflection in broadband spectrum can be achieved. Effect of parameters such as layer numbers, number of segments and layer materials are also

studied. Resulting sharp transmission peaks over the spectra are also analyzed and underlying mechanisms are approached. Given research in this field shows that reflection approaching to unity can be achieved with refractory metals.

- Black Silicon: Black silicon, which have broadband absorption in wavelength of interest, is achieved by introducing roughness on the surface, either in random or deterministic fashion, with various fabrication methods. Besides the vast literature regarding the design and fabrication of black silicon, origins of the absorption are not well explored. Research reported in this dissertation reveals the origins of the broadband absorption/emission of black silicon. Study reveals that two different electromagnetic phenomena occur in the textures which give rise to increased field intensity, therefore elevated absorption. Depicted results, explains the responsible mechanisms in detail and shed a light on the origins of the broadband absorption in black silicon.
- High temperature broadband thermal emitter: Emission of ZrB_2 when patterned is studied in broadband spectrum, due to its excellent thermomechanical properties to be utilized in high temperature applications. Although optical properties of ZrB2 are reported in the literature, its emission is not studied with patterning. Research given in this dissertation contributes to the literature in several aspects:
    - Adjoint method-based topology optimization is used to design patterns and final results exhibit elevated emission/absorption in broadband spectrum. Depicted results show the potential of adjoint based topology optimization in broadband emission/absorption enhancement, which enables non-intuitive patterns in computationally reasonable time frame.
    - Dispersion in dielectric function of ZrB_2 provides exciting different resonance modes over the spectra which result in distinct emission/absorption peaks. All the resulting peaks in the spectrum are analyzed and well-studied, which can be tailored for different applications, e.g. narrowband absorber/emitters for sensing.

Several scientific papers are already published as an outcome of the research given in this dissertation and more is about to be prepared. List of the published works are:

- Kecebas, M. A., Menguc, M. P., Kosar, A., & Sendur, K. (2017). Passive radiative cooling design with broadband optical thin-film filters. *Journal of Quantitative Spectroscopy and Radiative Transfer, 198*, 179-186.

- Keçebaş, M. A., & Şendur, K. (2018). Enhancing the spectral reflectance of refractory metals by multilayer optical thin-film coatings. *JOSA B, 35*(8), 1845-1853.
- Kecebas, M. A., Menguc, M. P., Kosar, A., & Sendur, K. (2020). Spectrally selective filter design for passive radiative cooling. *JOSA B, 37*(4), 1173-1182.

The submitted manuscripts to the scientific journals are:

- Keçebaş, M.A., Pirouzfam N., & Şendur, K. "Origins of the Broadband Absorption in Black Silicon".

1.5. Thesis Outline

The thesis is composed of 4 main chapters, in all which methods and corresponding results, discussions are given for the specific area and dissertation ends with final conclusions. In chapter 2, a spectrally selective thin-film optical filter design method for daytime passive radiative cooling is proposed. Proposed algorithm optimizes the film thicknesses for the selected number of layers and layer materials.. Spectral results are also evaluated by wave impedance analysis.

In chapter 3, multilayer thin-film structure is designed to enhance the spectral reflectance of selected refractory metals like, W, Ta, Mo and Nb. Effect of parameters like layer numbers and layer materials are analyzed. Also resulting dips over the spectra are analyzed.

Origins of the broadband high absorption in black silicon are studied in chapter 4. Absorption spectra and field distributions over the random textures are obtained and deterministic textures are analyzed to analyze the fundamental mechanisms. Occurrence condition of local high field enhancements and phenomenon that interfere with local enhancements are estimated by effective wavelength matching and waveguide modes.

Finally, in chapter 5, emission/absorption spectrum of rectangular gratings composed of ZrB_2 are studied for varying dimensions. Resulting resonances are analyzed by studying cavity and plasmon modes, as well as applying effective medium theory for metamaterials. Then, adjoint based inverse design method is utilized the further improve the emission/absorption in broadband spectrum. Final patterns are obtained by introducing topological changes in the gradient direction obtained by adjoint method in a computationally reasonable time.

2. SPECTRALLY SELECTIVE FILTER DESIGN WITH THIN-FILMS FOR DAYTIME PASSIVE RADIATIVE COOLING

In this section, a methodology to design a daytime passive radiative cooling structure with thin film filters is outlined. As opposed to previous approaches, this new formulation introduces broadband weighting on the spectral response based on the contribution to the cooling power. A step by step design procedure is given and explained throughout the manuscript. In Section 2, daytime passive radiative cooling problem is summarized, and the advantages of the new method are discussed. In Section 3, the formula for thickness and material and angle dependent spectral reflectance is given [180]. Then, the problem is reformulated as a cooling power maximization problem, which is obtained from the spectral response of the multilayer structures and radiative heat transfer equations. In the formulation, layer thicknesses are determined such that the cooling power of the structure is maximized for a selected number of layers with predetermined materials. Different designs with a varying number of layers are investigated, and their angular dependence, cooling powers and resulting temperature reductions are reported. To explain the underlying mechanisms that lead to broadband spectral selectivity, the change of surface impedance values is also demonstrated and analyzed. Previously, the surface impedances are used in radio frequency (RF) and microwave regimes [181-183] for design purposes. Here, surface impedances of the multilayers are used to evaluate the resulting spectral response of the designed structures. In the literature, surface impedance techniques have also been used in various thin film structures [4, 184-186]. In summary, this study presents a complete methodology both for design and analysis purposes, which can be utilized to design high performance daytime passive radiative cooling coatings.

2.1 Problem Definition

Passive radiative cooling for daytime applications is based on reflecting undesired radiative components and radiating heat away from the surface to the cold outer space. Since all radiative components are spectral quantities [21], it is necessary to consider the spectral distribution of radiation components over the electromagnetic spectrum. Thermal radiation from surfaces is expressed using Planck's equation given as in Eq. (2.1).

$$I_{BB}(T,\lambda) = \frac{2hc^2}{\lambda^5}\frac{1}{e^{hc/(\lambda k_B T)}-1} \tag{2.1}$$

In Eq (2.1), λ h, c and k_B are wavelength, Planck's constant, the speed of light and the Boltzmann constant, respectively. Spectral thermal radiation profiles from surfaces at 5850 and 300 K are depicted in the inset of Fig. 2.1. As shown, a surface with a temperature of 5850 K radiates strongly in the visible and near infrared spectrum, which approximates thermal radiation by the sun, whereas radiation from a surface with a temperature of 300 K is strongly confined in the 8-13 μm spectrum. The high transparency of the atmosphere in the 8-13 μm spectrum is shown in Fig. 2.1, and atmospheric transmittance is mathematically expressed as follows,

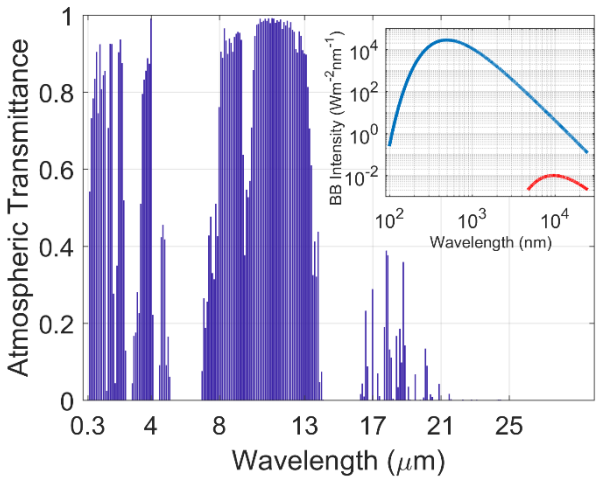

Fig. 2.1. Thermal radiation, expressed by Planck's law, from surfaces with temperatures of 300 K and 5850 K and atmospheric transmittance in 0.3 – 25 μm spectrum.

$$\varepsilon_{Atm}(\lambda,\theta) = 1 - t(\lambda)^{1/\cos\theta} \tag{2.2}$$

In Eq. (2.2), t(λ) is the atmospheric transmittance in the zenith direction [187], where 'θ' is the zenith angle. The distributions in Fig. 2.1 and Eq. (2.2) suggests that surfaces with temperatures around 300 K can radiate heat away from the surface to the cold outer space mostly within the 8-13 μm spectrum.

Besides emission in the atmospheric transparency window, low absorptivity at wavelength spectrum at which solar irradiance is strong (especially in the 0.3 – 2 μm wavelength range) is required. Therefore, spectrally selective filters are required to be highly emissive in the 8-13 μm spectrum interval and must have a very low absorption elsewhere for passive radiative cooling applications.

Cooling power of a surface is determined by evaluating the power in and outflow on the surface and expressed as,

$$P_{Cool} = P_{Rad} - P_{Atm} - P_{Sun} - P_{Cond+Conv} \tag{2.3}$$

where, P_{Cool} is the cooling power of the surface. P_{Rad} is the power radiated away from the surface and expressed as,

$$P_{Rad} = A2\pi \int_0^{\pi/2} d\Omega \cos\theta \int_0^{\infty} d\lambda I_{BB}(T,\lambda)\varepsilon(\lambda,\theta) \tag{2.4}$$

where, $\varepsilon(\lambda,\theta)$ is the emittance of the surface and $d\Omega = d\theta sin\theta$ is the angular integral over a hemisphere. P_{Atm} is the absorbed atmospheric thermal radiation given as,

$$P_{Atm} = A2\pi \int_0^{\pi/2} d\Omega \cos\theta \int_0^{\infty} d\lambda I_{BB}(T,\lambda)\varepsilon_{Atm}(\lambda,\theta)\varepsilon(\lambda,\theta) \tag{2.5}$$

absorbed solar power, P_{Sun}, is given as,

$$P_{Sun} = A\int_0^{\infty} d\lambda I_{Sun}(\lambda)\varepsilon(\lambda,\theta_{Sun}) \tag{2.6}$$

at a fixed incident solar irradiance angle θ_{Sun}. Finally, $P_{Cond+Conv}$ term is expressed as,

$$P_{Cond+Conv} = Ah_c(T_{Amb} - T) \tag{2.7}$$

to include the non-radiative heat fluxes in the system. In Eq. (2.6), ISun is the AM1.5 Global tilt spectrum, which is given in [11]. Eq. (2.7) is for the contributions from conduction and convection. These equations are used to evaluate the cooling power of the structures under consideration. However, the connection between spectral profiles and the cooling power was not clearly outlined during the design methods reported in the literature.

By using equations (2.3) - (2.7) and considering the spectral distribution of solar irradiance and atmospheric transmittance (as shown in Fig. 2.1), the following spectral requirements to maximize the cooling power of surfaces can be determined: A daytime passive radiative cooling structure should strongly emit in the 8-13 μm spectrum, where the atmosphere is mostly transparent and highly reflects at shorter and longer wavelengths to prevent solar irradiance and atmospheric thermal radiation absorption. Generally, the requirement of low absorption in visible and near-infrared spectra is fulfilled by coating a strong metal reflector on the structure, e.g. Ag, and by using lossy materials to enhance emittance in the 8-13 μm interval.

Previous methods, e.g. [11, 73], have focused on minimizing the error between a given ideal emittance curve and actual emittance spectrum. Objective function for such minimization is given in Eq. (2.8) in Table 2.1. Then, cooling power performances of the designed structures are evaluated by equations given in (2.3) - (2.7).

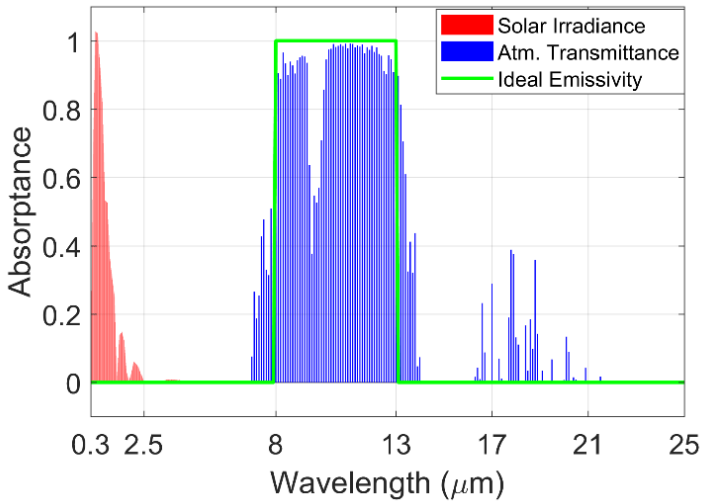

Fig. 2.2. Ideal emittance profile used in [11] plotted with respect to solar irradiance and atmospheric transmittance.

Table 2.1. Mathematical expressions for spectral and cooling power-based formulations

Approach	Cost Function	Eq.
(1) Spectral	$\min \left\| \varepsilon_{Target}(\lambda) - \varepsilon_{Actual}(\lambda) \right\|$	(2.8)
(2) Cooling Power	$\max P_{Cool} = P_{Rad} - P_{Atm} - P_{Sun}$	(2.9)

The cumulative spectral error in terms of minimum mean squares based on the difference between ideal and actual emittances serves as a reference to compare the spectral performance of different designs. Although the resulting structures with non-ideal emittance profiles might outperform each other in terms of cumulative errors, they do not necessarily result in higher cooling powers. This is because of the broadband nature of the problem and the spectral distribution of solar irradiance and atmospheric transparency.

Due to the broadband nature of the problem, coatings alter the spectral behavior over the entire spectrum. Therefore, a coating increasing the emittance in the 8-13 μm spectrum may also enhance the absorptance at longer wavelengths, where the atmospheric thermal radiation is strong. Such an increase in longer wavelengths introduces significant thermal load to the system, and if not compensated by emitted power, total cooling power decreases. Therefore, during the design processes, the effect of spectral behavior on the cooling powers should be considered. This is achieved by reformulating the optimization problem based on the cooling power. In this case, the cost function is transformed from (1) to (2) as shown in Table 2.1. Spectral behaviors of the two 4-layer structures designed based on the objective functions given in Table 2.1, are demonstrated in Fig. 2.3.

Fig. 2.3 shows that, there is a considerable difference in absorptance around the 11 – 19 μm interval, whereas only slight changes exist in shorter wavelengths. Minimum mean square errors between actual and ideal emittances are 31.03 and 38.55 and cooling powers are around 55 and 70 W/m^2 respectively for spectral and CP approaches. These results indicate the superiority of the CP approach over the spectral approach. Even with the increased absorption (P_{Atm}) at wavelengths longer than 13 μm, the CP method results in structures with higher cooling powers due to reduction in P_{Sun} and increase in P_{Rad} (demonstrated in table 2.2). These results show the importance of weighting on the spectral behaviors based on the contribution to cooling powers.

The proposed method is called cooling power (CP) approach, since it focuses on cooling power maximization by tailoring the spectral emittance, instead of pure spectral error minimization.

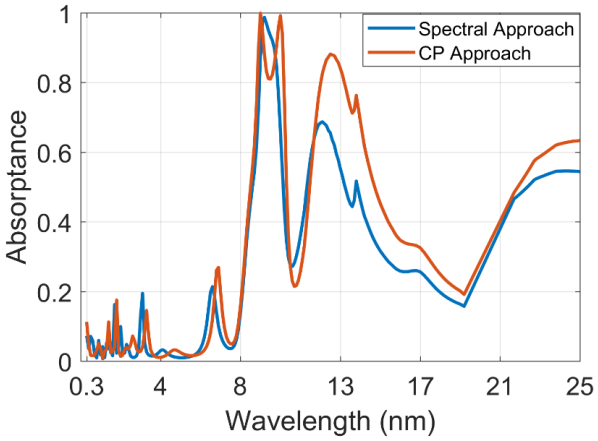

Fig 2.3. Spectral absorptance of 4-layer structure at perpendicular angle of incidence, designed by spectral and cooling power methods for which cost functions are depicted in Table 1.

Table 2.2. Radiative heat components for the structures with 4 layers designed by spectral and CP approaches

Radiative Heat Components	Spectral Approach	CP
P_{Rad} (W/m^2)	148.79	175.39
P_{Sun} (W/m^2)	25.52	22.68
P_{Atm} (W/m^2)	68.19	82.97
P_{Cool} (W/m^2)	55.07	69.73

2.2 Methodology

2.2.1. Wave Impedance & Reflectance of Thin-Films

Wave impedance is the ratio of the transverse components of the electric and magnetic fields, which is equal to the ratio of the permeability and permittivity of the medium:

$$Z = \sqrt{\frac{\mu}{\varepsilon}} \tag{2.10}$$

where ε = (n-j*k)2 and ‘n-j*k’ is the complex refractive index. In thin-film applications, lossy substrates such as Si can be considered as a homogenous semi-infinite layer. When thin-films are coated on the top of a substrate, the wave impedance at the top surface is the wave impedance of the multilayer thin-film system, ‘Z ’, which is defined in terms of intrinsic impedance of the individual components as,

$$\mathcal{Z}_i = Z_i \frac{\mathcal{Z}_{i+1} + jZ_i \tan(\delta_i)}{Z_i + j\mathcal{Z}_{i+1} \tan(\delta_i)} \tag{2.11}$$

where 'Z_L', is the intrinsic impedance of the last film, which is coated on the substrate, '$\mathcal{Z}_i$' is the wave impedance on the front surface of a multilayer system. 'δ_i' is the optical thickness of the layers and expressed as, $\delta_i = \frac{2\pi * (n - j * k) * d * \cos(v_i)}{\lambda}$ where 'd_i' is the geometrical thickness, 'v_i' is the angle of refraction. A sample diagram showing the effect of layers on the impedance of the substrate and describing the variation of the surface impedance is depicted in Fig. 2.4. In Fig. 2.4, Z_L, Z_{M1} and Z_{M2} are the intrinsic impedances of the substrate and coated layers respectively. In the diagram, impedance matching with 2 layers between the Z_L and Z_0 is schematized. Once the impedance on the front surface is determined, the reflectance coefficient of the structure is obtained as

$$\Gamma_1 = \frac{\mathcal{Z}_1 - Z_0}{\mathcal{Z}_1 + Z_0} \tag{2.12}$$

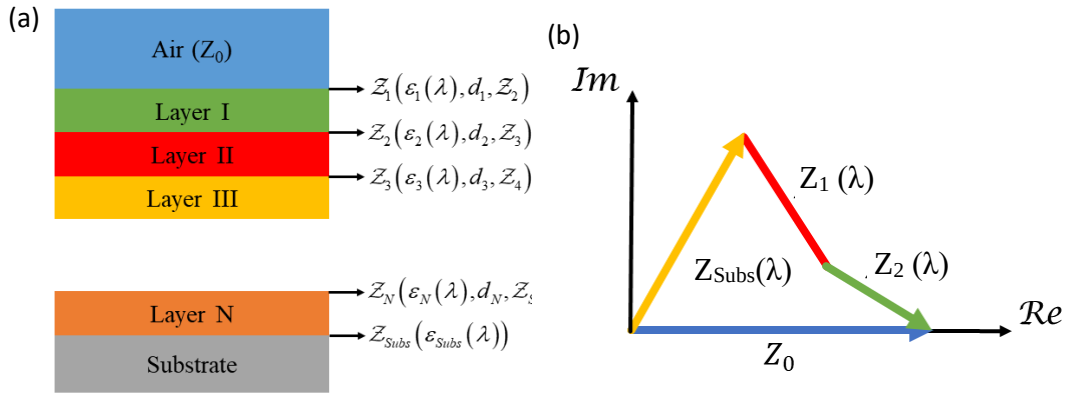

Fig. 2.4. Diagram that shows how impedance matching between a substrate, with impedance Z_L, and air (Z_0) is achieved by two layers with intrinsic impedances of Z_{M1} and Z_{M2} respectively.

The surface impedance values are mapped to complex gamma plane by normalizing reflection coefficients as,

$$\Gamma_{Norm} = \frac{\mathcal{Z}_1 / Z_0 - 1}{\mathcal{Z}_1 / Z_0 + 1} \tag{2.13}$$

where Γ_{Norm} is the normalized reflectance coefficient. To demonstrate the variety of the high reflectance solutions, reflection coefficients of a passive radiative cooling structure with three layers are plotted on the complex gamma plane. The considered structure is schematized in Fig. 2.5(a), and its spectral absorptance is demonstrated in Fig. 2.5(b). Cooling power of this

structure is 50 W/m^2, calculated from Eqs. (2.3) – (2.6). As seen, the absorption of the structure is very low until the wavelength of 8 μm, except the high absorption peak around 0.3 μm due to the Ag layer. An alternative and complementary way to understand the performance of this structure can be given by plotting the spectral reflectance in the complex gamma plane in Fig. 2.5(c). Fig. 2.5(c) is formed by plotting $\Gamma_{Norm}(\lambda)$ on complex plane for different wavelengths. Multiple $\Gamma_{Norm}(\lambda)$ values are plotted in spectrum intervals of 0.3-8, 8-13 and 13-25 μm.

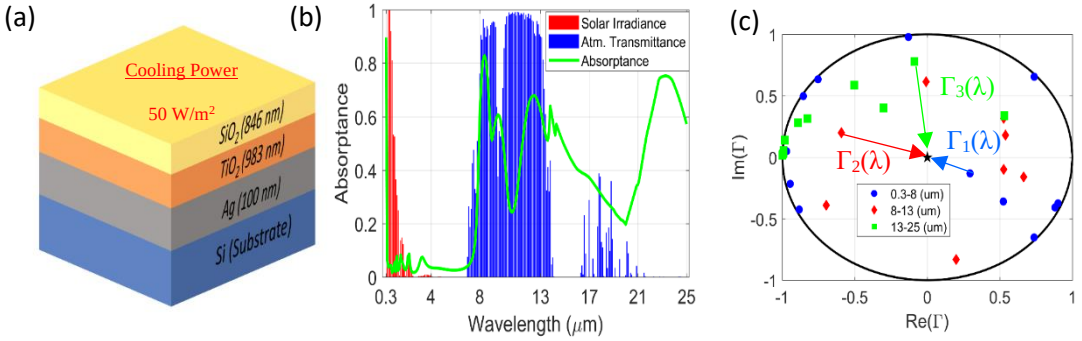

Fig. 2.5. a) Structure with 3 layers designed by the impedance formulation which has cooling power of 50 W/m^2 at 300 K. b) Spectral absorptance of the structure depicted in (a) at perpendicular angle of incidence, plotted with solar irradiance in 0.3 – 4 μm and atmospheric transmittance in 8 – 25 μm spectrum interval. c) Spectral distribution of reflectance coefficients of the structure depicted in (a).

Here, the high reflectance points are distributed close to the unit circle and only low reflectance points are closer to the center of the circle. On the unit circle $|\Gamma_1|^2$ becomes 1. As the points get closer to the center, $|\Gamma_1|^2$ decreases and becomes zero only at the center. Therefore, the solution of perfect impedance match is unique (center of the unit circle), whereas there are multiple solutions (on the unit circle) for perfect mismatch for a given structure.

Based on this, the desired residual errors, $R_i(\lambda)$,

$$R_i = \sqrt{(0 - \mathrm{Re}(\Gamma_1(\lambda))^2 + (0 - \mathrm{Im}(\Gamma_1(\lambda))^2} \tag{2.14}$$

for daytime passive radiative cooling are defined as:

1. Max $R_1(\lambda)$: Maximization of the distances between reflectance coefficients and perfect impedance matching point (center of the unit circle) for high reflectance in the 0.3 -8 μm spectrum.

2. Min $R_2(\lambda)$: Minimization of the distances between reflectance coefficients and perfect impedance matching point for low reflectance in the 8-13 μm spectrum.

3. Max $R_3(\lambda)$: Maximization of the distances between reflectance coefficients and perfect impedance matching point for high reflectance in the 13-25 μm spectrum.

In the following section, the design problem is mathematically formulated, and corresponding spectral results are discussed from the perspective of residuals.

2.2.2 Design & Performance Evaluations

The design problem is considered as the maximization of cooling power:

$$\max P_{Cool} = P_{Rad}(T, \varepsilon(\lambda)) - P_{Rad}(T, \varepsilon(\lambda)) - P_{Sun}(\lambda) \tag{2.15}$$

based on radiative heat transfer components. In Eq. (2.15), 'ε(λ)' is expressed in terms of normalized reflectance coefficients as $1-|\Gamma_1|^2$ based on surface impedance of the structure. The basic steps of the design methodology are outlined as follows:

First, 100-nm Ag is coated on the top of Si substrate, and its surface impedance is obtained using Eq. (2.11). Next, SiO_2 and TiO_2 layers are added in a series, and the surface impedance of the final structure is formed by leaving the layer thicknesses as unknowns. The optical properties of these materials are obtained from the literature [188-189]. The reflectance coefficients for these materials are obtained using Eq. (2.12) and are mapped to the complex gamma plane using Eq. (2.13). Finally, residual errors are defined from the normalized gamma values, are inserted in the cost function given in Eq. (2.15), where the layer thicknesses are obtained. A flow diagram for the complete procedure is depicted in Fig. 2.6.

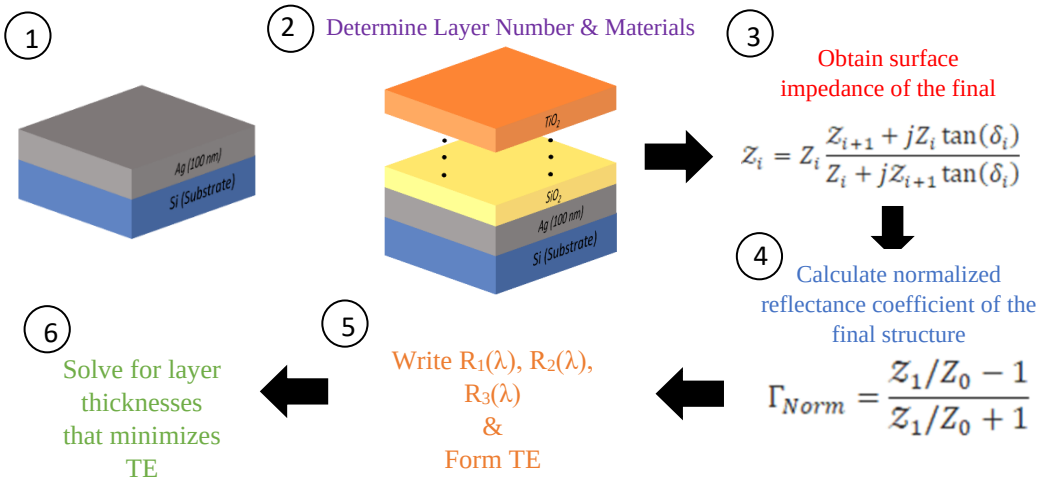

Fig. 2.6. Design steps for the cooling power-based method

Following the procedure given in Fig. 2.6, layer thicknesses are solved for layer numbers of 1 to 7, and cooling power of these structures is displayed in Fig. 2.7(b). As seen, an increasing trend in cooling power (T_{Surf} = 300 K and T_{Amb} =297 K) is observed with increasing number of layers. Cooling power reaches 100 W/m^2 with 7 layers on the top of Ag layer. The spectral distribution of the absorptance/emittance is also shown in Fig. 2.7(c) and 2.7(d), where selective emission occurs in the 8- 13 μm spectrum and high reflection is seen elsewhere. Average reflectances in the 0.3 – 8 μm and 13 – 25 μm spectra are 97% and 50% respectively, and the emittance in the 8 – 13 μm spectrum is 80%.

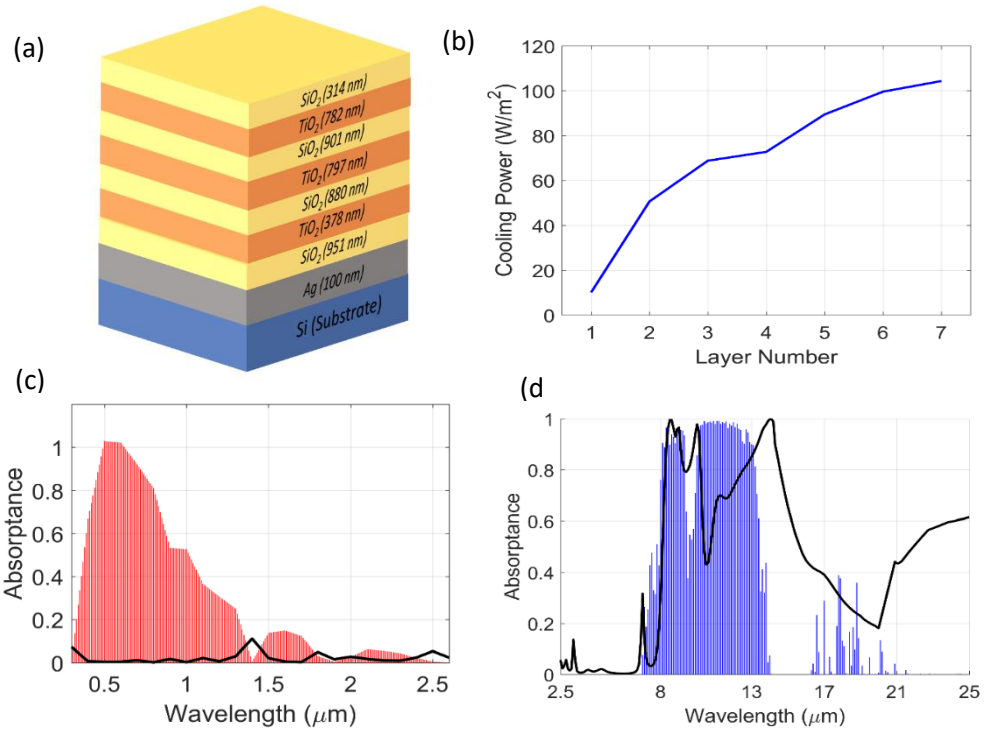

Fig. 2.7. a) Final structure with 7 layers. b) Cooling power at 300 K and T_{Amb} =297 K. c) Absorptance of the structure depicted in (a) in spectrum interval 0.3 – 2.5 μm plotted on solar irradiance in this interval at perpendicular angle of incidence. d) Absorptance of the structure depicted in (a) in spectrum interval 2.5 – 25 μm at perpendicular angle of incidence, plotted on atmospheric transmittance in this interval.

Normalized gamma values of the final structure with 7 layers are demonstrated in Fig. 2.8 and are compared to gamma values of Ag. As seen in Fig. 2.8(a), gamma values of the Ag layer in the 0.3 – 8 μm spectrum are clustered on the left side of the circle. When seven layers are coated on the top of Ag, we see that, Γ(λ=1.5), Γ(λ=4.5) and Γ(λ=7) values change but remain very close to the outer bounds of the unit circle. Therefore, the high reflectance at these wavelengths is still preserved. However, Γ(λ=0.3) also approaches to the outer edge of the unit

circle, thus its reflectance is increased, as shown in Fig. 2.7(c) and distinct absorptance peak due to Ag layer is suppressed. This suppression has significant impact on P_{Sun} component since radiation intensity around 0.3-0.4 μm spectrum is high as shown in Fig. 2.2. Gamma values are significantly altered in the 8-13 μm spectrum interval and approach to the center of the unit circle. Finally, at longer wavelengths (λ ≥13 μm), gamma values deviate from the unit circle, thereby resulting in decreased reflectance and increased absorption of the atmospheric thermal radiation. These changes occur mainly because of the lossy nature of SiO_2 and TiO_2 in these spectrum ranges. By optimizing the thicknesses, spectral selectivity (high and low emission in 8-13 μm and 13 – 25 μm intervals respectively), is achieved, as seen in Fig. 2.7(d). High emittance in 8-13 μm spectrum is achieved except a sharp dip around 11.5 μm which is attributed to phonon polariton resonance of SiO_2 around 10 μm.

Note that there is a small reduction in emission intensity around 9 μm is observed which is overlapping with the dip of the atmospheric transmittance in 8-13 μm interval. This behavior is similar to results reported in [73], in which modified ideal emittance curve in 8-13 μm (unity emission in 8-13 μm spectrum except around 9-10 μm wavelengths) is utilized. Authors of [73] report improved cooling powers due to modified ideal emittance curve by which the negative contribution of the dip in atmospheric transmittance window is suppressed. Our results indicate that CP based approach automatically achieves that modified spectral profile, by which cooling power is further improved. In Table 2.3, residual errors and radiative heat components (P_{Rad}, P_{Sun}, P_{Atm}) for Ag and structure with 7 layers given in Fig. 2.6(a) are displayed.

Table 2.3. Corresponding R(λ) and P values for 7-layered coating and Ag.

	Spectrum Interval	**Ag**	**Coated**
$\|\|R_1(\lambda)\|\|$	λ (0.3-8 μm)	8.7	8.8
$\|\|R_2(\lambda)\|\|$	λ (8-13 μm)	7.02	3.4
$\|\|R_3(\lambda)\|\|$	λ (13-25 μm)	10.29	7.64
Radiative Heat Loads	P_{Rad} (W/m^2)	27.3	207.31
	P_{Sun} (W/m^2)	26.29	6.75
	P_{Atm} (W/m^2)	23.84	96.24
	P_{Cool} (W/m^2)	-22.83	104.32

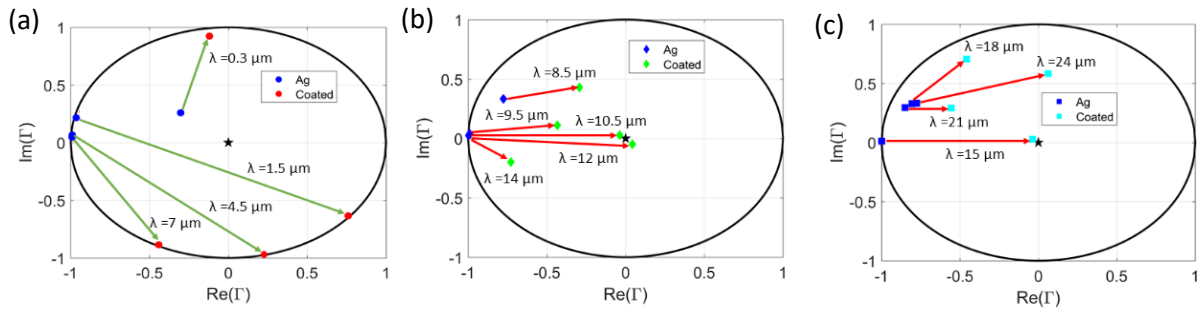

Fig. 2.8. a) Spectral distribution of reflectance coefficients of the structure depicted in Fig. 5(a), in 0.3 -8 μm spectrum, on complex gamma plane. b) Spectral distribution of reflectance coefficients of the structure depicted in Fig. 5(a), in 13 -25 μm spectrum, on complex gamma plane. c) Spectral distribution of reflectance coefficients of the structure depicted in Fig. 5(a), in 8 -13 μm spectrum, on complex gamma plane.

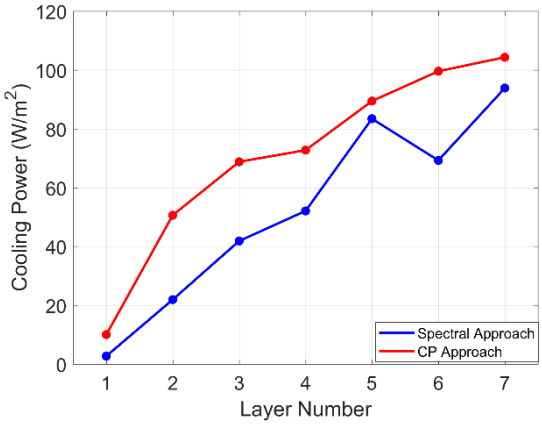

Fig. 2.9. Cooling power comparison of the structures designed by spectral and cooling power approach with layer numbers of 1 to 7.

Cooling powers of the structures designed by the spectral approach and cooling power approach with number of layers changing from 1 to 7 are compared in Fig. 2.9. Demonstrated cooling power results are discussed with the reported values of residual errors in Table 2.3.

As shown, cooling powers of the structures are higher when designed by the cooling power approach. Also, an increasing trend is observed with increasing number of layers with this approach. In the spectral approach case, when the layer number is increased from 5 to 6, cooling power is decreased from ~80 W/m^2 to ~70 W/m^2. To analyze this behavior, we compared the spectral behavior of these two structures. In Fig. 2.10, spectral behavior of 5 and 6 layered structures designed by the spectral approach at perpendicular angle of incidence is shown. As seen from Fig. 2.10, the spectral behavior is not significantly altered with in the 8-13 μm band, but significant changes are observed in 0.3-8 μm and 13-25 μm spectrum intervals. In Table 2.4, minimum mean square error values are given for the structures. As seen, MMSE value for the 6 layered structure is lower compared to the 5 layered structure. However, the 6

layered structure exhibits higher cooling power, which is explained by considering the average emittances and radiative heat components in Table 2.5. The average emittances in separate intervals indicate that reduced MMSE is the result of the reduced emittance in the 13 -25 μm spectrum. Reduction in $\overline{\varepsilon_3(\lambda)}$ results in a decrease in P_{Atm} (~6 W/m^2), leads also a considerable rise in $\overline{\varepsilon_1(\lambda)}$ and solar absorption. Thus, the total cooling power P_{Cool} is reduced to 69.25 W/m^2 from 83.42 W/m^2. This comparison and tabulated results in Table 2.5 reveal the advantage of the cooling power approach over the spectral approach. In the spectral approach, the effects of spectral behavior on the cooling power are ignored during the design process. The results indicate that a quantitatively better solution, shown in Table 2.4, in terms of spectral behavior does not necessarily result in higher cooling powers as depicted in Table 2.5. When the effects of spectral behavior on cooling powers are considered in the design process, much better designs are obtained.

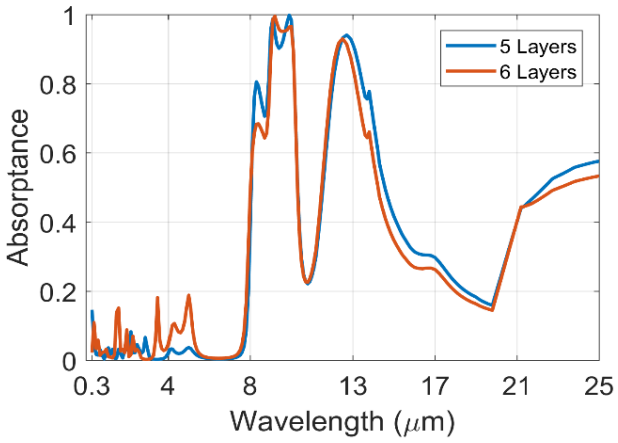

Fig. 2.10. Comparison of spectral emittance of the structures with 5 and 6 layers designed by spectral approach at perpendicular angle of incidence

Table 2.4. Comparison of MMSE of the structure with 5 and 6 layers designed by spectral approach

$MMSE = \sum(\varepsilon_{Ideal}(\lambda) - \varepsilon_{Actual}(\lambda))^2$	
5 Layers	33.73
6 Layers	29.60

Table 2.5. Average emittances and radiative heat components for the structures with 5 and 6 layers designed by spectral approach

	Spectrum Interval	5 Layers	6 Layers
$\overline{\varepsilon_1(\lambda)}$	λ (0.3-8 μm)	2.78 %	5.34 %
$\overline{\varepsilon_2(\lambda)}$	λ (8-13 μm)	70.74 %	69.86 %
$\overline{\varepsilon_3(\lambda)}$	λ (13-25 μm)	42.82 %	38.89 %
Radiative Heat Components	P_{Rad} (W/m^2)	177.95	170.49
	P_{Sun} (W/m^2)	16.29	28.69
	P_{Atm} (W/m^2)	78.23	72.54
	P_{Cool} (W/m^2)	83.42	69.25

In Fig. 2.11(a) and 2.11(b), angular spectral emittances with respect to wavelength for TE and TM polarizations are displayed. As seen from these results, the selective behavior of a filter is preserved in both polarizations for wide range of angles. Also, angular emittance of the structure with seven layers, whose spectral emittance in perpendicular angle is depicted in Fig. 2.7(d), is shown in Fig. 2.11(c). Results indicate that angular dependency of the emittance of the structure is low in broadband. As seen, very low emittance values in 0.3-2.5 and 2.5-8 μm intervals are observed, whereas it is increased in longer wavelengths, especially in 8-13 μm interval. Equilibrium temperatures of the structures are also evaluated based on the spectral behavior and the radiative components and are demonstrated in Fig. 2.12(a) for h_c =5.

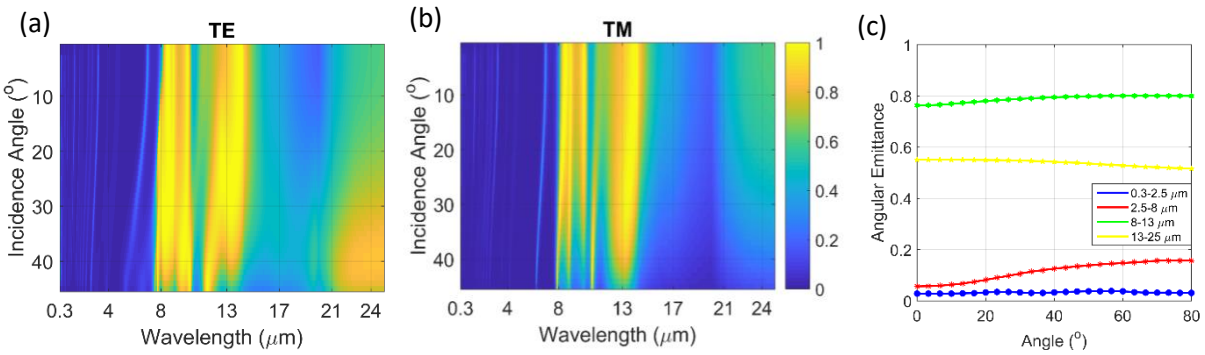

Figure 2.11: TE polarized emittance of the 8 layered structure depicted in Fig. 7(a) with respect to wavelength and incidence angle. b) TM polarized emittance of the 8 layered structure depicted in Fig. 7(a) with respect to wavelength and incidence angle. c) Angular emittance of the structure with 7 layers.

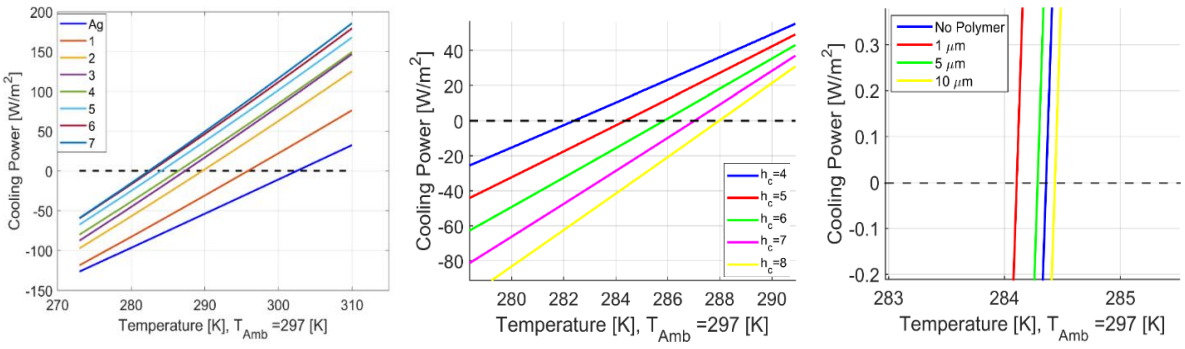

Figure 2.12 a) Temperature vs. cooling power curves of Ag and structures with varying number of layers, 1 to 7 with hc=5. b) Temperature vs. cooling power curves for the structure with 7 layers for varying hc values. c) Temperature vs. cooling power curves for the structure with 7 layers with and without a polymer coating of varying thicknesses with constant h_c of 5.

The equilibrium temperatures of the structures for varying number of layers are obtained by setting the cooling power equation, given in Eq. (2.3), to zero as

$$P_{Cool} = P_{Rad}(T_{Eq}) - P_{Atm}(T_{Amb}) - P_{Sun} - P_{Cond+Conv} = 0 \tag{2.16}$$

The change in cooling power with respect to temperatures are demonstrated in Fig. 2.12(a), from which equilibrium temperatures are deduced. Parasitic heat load coefficient, h_c, of 5 $Wm^{-2}K^{-1}$ is assumed to address conductive and convective contributions as in parallel lines with the literature [51], and T_{Amb} is set as 297 K. The equilibrium temperature of Ag at these conditions is around 302 K. For 7 layers, the equilibrium temperature is around 282 K, which is 15 K below the ambient temperature. When h_c is set to 0, structure can achieve a steady state temperature 40 K below the ambient temperature. Previously reported values for this case are around 24 K and 19 K in [73] and [11] respectively.

In Fig. 2.12(b), equilibrium temperatures for h_c values ranging from 4 to 8 are also shown. The equilibrium temperature of the structure with 7 layers is increased from 280 K to 288 K when h_c is increased from 4 to 8 $Wm^{-2}K^{-1}$. Results show that below ambient air temperature is still achieved when the heat exchange with the surrounding is increased. Finally, to observe the optical impact of the convection suppression through an insulator, the effect of a polymer layer on top of the designed coating's spectral emittance is analyzed.

Constant refractive index of 1.4 is assumed for the insulator polymer layer and its effect on the cooling temperature reductions are shown in Fig. 2.12(c). The polymer coating does not have a significant impact on the temperature of the structure for a constant hc of 5 $Wm^{-2}K^{-1}$, due to its transparency. On the other hand, polymers like PDMS, which have strong thermal

emissivity in mid-infrared range can further improve the radiative cooling performance as reported in [190-191].

Although atmospheric transparency is dependent on several factors, e.g. cloudiness, humidity and water vapor, we considered the profile depicted in Fig. 2.1 in the analysis. Such changes in the atmospheric transparency may also alter the spectral requirements for radiative cooling as discussed in [192]. Under different atmospheric transparency conditions, broadband emitters such as paints and building materials may provide higher cooling powers. However, when the structures are well-shielded from convection, higher cooler powers with the proposed selective emitters can be achieved. Use of such spectrally selective filters in cooling panels is also reported in the literature [193]. Radiative cooling structures for different emittance profiles can be designed with the proposed method for different atmospheric conditions.

3. ENHANCING THE SPECTRAL REFLECTANCE OF REFRACTORY METALS BY MULTILAYER OPTICAL THIN-FILM COATINGS

The principal motivation of this chapter is to describe a design methodology to reduce the spectral absorption of refractory metals, especially 300-1500 nm spectrum, through optical coatings. It is well known that optical filters, which consists of periodic low-index/high-index filters, can increase the reflection of surfaces in at distinct spectral points. In this study, we aim to use periodic low-index/high-index filters to increase the broadband reflectance from refractory metals coated by multilayer films so that they reflect incident radiation in 300-1500 nm spectrum. While achieving this task, the optical filter should not create additional burden on the materials system, such as creating additional absorption from longer wavelengths. To achieve this goal, I use dielectric materials that do not absorb at visible and near-infrared are selected, such as TiO_2, SiO_2 and Al_2O_3. A schematic representation of the problem description is shown in Fig 3.1.

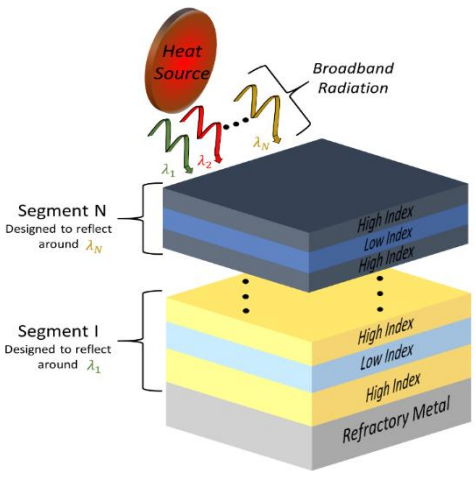

Fig. 3.1. Broadband source radiates power at the wavelengths λ_1 to λ_N which are incident upon the refractory metal coated with periodic high-low index films. Groups of periodic segments are stacked together to generate high reflectance zones by equalizing the phases of reflected waves from the films.

3.1 Incident Thermal Radiation and Spectral Reflectivity of Refractory Metals

In this part, incident solar irradiance above the atmosphere is approximated as radiation from a blackbody at 5850 K. During the analysis, incident radiation in 300-3000 nm spectrum, which is plotted in Fig. 3.2(c), and divided into two sub-intervals 300-1500 and 1500-3000 nm. Such division is done because spectral reflectance of the selected refractory metals is relatively low in the 300-1500 nm interval, whereas it increases up to 90% levels in the 1500-3000 nm spectrum. When incident radiation is encountered with a different medium, it is reflected, transmitted and absorbed at different percentages. Percentages of these three different spectral behaviors are dependent on optical properties of the mediums and geometry of the encountered structure. In this study, refractory metals are coated with thin-film filters. For the calculation of the spectral behaviors of the filters we utilized transfer matrix method [chapt. 2 of Ref. 194]. Our goal is to design filters with high reflectance in a broad spectrum to reflect the incident radiation. To achieve this, spectral reflectances/absorptances are calculated both for selected refractory metals and their coated versions with multilayer thin-films. Performance of the structure is quantified both in terms of average absorbed power as given in Eq. (3.1).

$$A_{avg} = \frac{1}{N}\sum_{i=1}^{N}[1-\Gamma(\lambda_i)] \tag{3.1}$$

The spectral reflectivity and absorption of refractory metals, W, Ta, Mo and Nb, are illustrated in Figs. 3.2(a) and 3.2(b). As shown in Fig. 3.2, average absorption percentage of these metals at the 300-1500 nm spectrum is in the range of 40-50%, whereas average absorption drops to less than 10% in 1500-3000 nm spectrum. Although spectral absorption of these metals are small beyond 3 μm wavelength, they are susceptible to absorb radiation at the visible and infrared spectrums especially below 1.5-μm wavelength. Spectral power distribution of incident solar irradiance just above the earth's atmosphere is also depicted in Fig. 3.2(c) in watts per meter square per wavelength. Solar irradiance is approximated by blackbody radiation at 5850 K and solid angle of $6.84*10^{-5}$. In Fig. 3.2(c), it is shown that solar power reaches to 2 $Wm^{-2}nm^{-1}$ levels in the visible spectrum and has a decreasing trend after 500-nm wavelength. Nearly 1270 Wm^{-2} power is present in the 300-1500 nm spectrum, whereas it drops by almost 90% in 1500-3000 nm spectrum to 135 Wm^{-2}. When thin-film layers of 500-nm thick of these materials are exposed to such radiative source, amount of absorbed powers are given in table 3.1.

In table 3.1, in two separate spectrum intervals of 300-1500 and 1500-3000 nm wavelengths, total solar power are presented. Average absorption percentages and absorbed powers for refractory metals of W, Ta, Mo and Nb are also reported. As shown in table 3.1, absorbed power percentages are around 40% in 300-1500 nm spectrum which corresponds to 488.4 W/m^2 power. Absorbed powers are decreased to 13 W/m^2 levels in 1500-3000 nm spectrum. The results in table 3.1, shows the need for broadband improvement of spectral reflectance to avoid such high undesired absorption in operating conditions in which heat transfer with radiation is dominant.

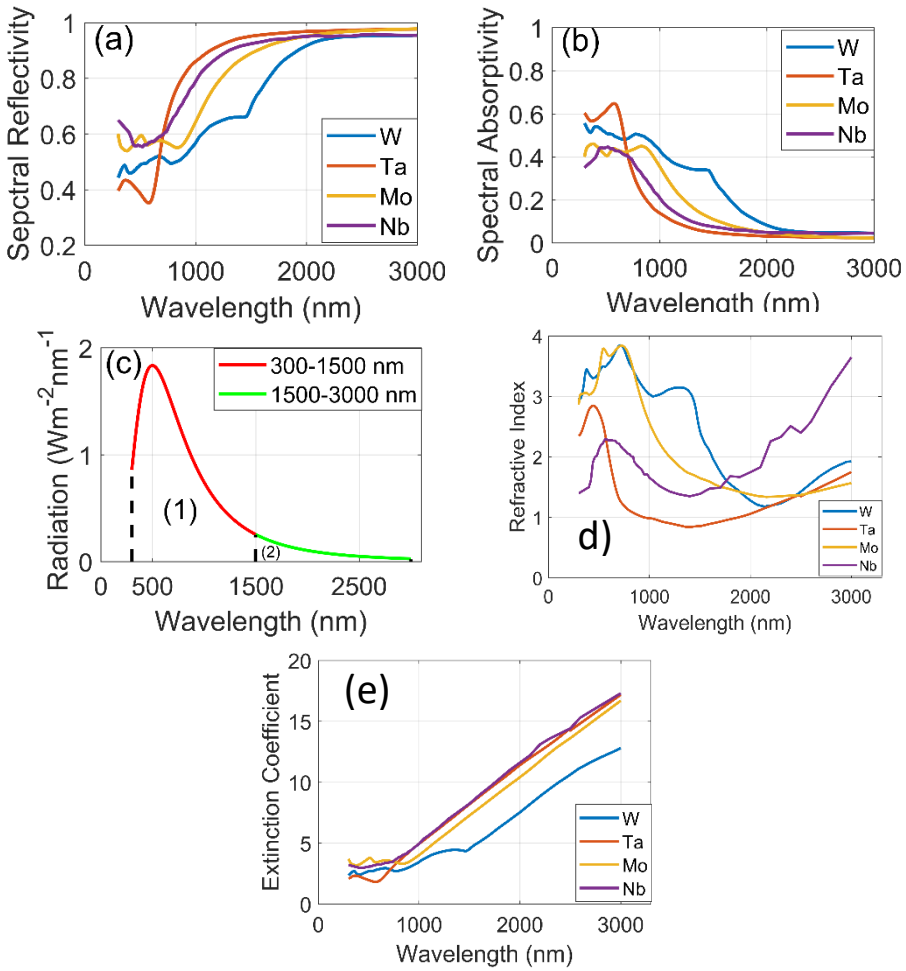

Figure 3.2. a) Spectral reflectivity of W, Ta, Mo and Nb films, each 500 nm thick, with respect to wavelength on top of a silicon substrate at perpendicular angle of incidence. b) Spectral absorptivity of W, Ta, Mo and Nb films, each 500 nm thick, with respect to wavelength on top of a silicon substrate at perpendicular angle of incidence. c) Spectral distribution of blackbody radiation of the sun that reaches to the atmosphere. Temperature is 5850 K and solid angle is 6.84*10^{-5}. (1) and (2) represent s two separate regions. Overall powers are calculated when blackbody radiation is integrated with respect to wavelength in 300-1500 nm, region 1, and in 1500 -3000 nm spectrum, region 2. Reported power densities are 1270 W/m^2 and 135 W/m^2 respectively. d) Refractive indices of selected refractory metals. e) Extinction coefficients of selected refractory metals.

Table 3.1. Average absorptivity of 500-nm of refractory metals, W, Ta, Mo and Nb, present solar power and absorbed solar power by these at 300-1500 nm and 1500-3000 nm spectrums.

Spectrum	300-1500 nm	1500-3000 nm
Material	Absorbed Power	Absorbed Power
W	44.25 %	13.11 %
Ta	37.46 %	3.54 %
Mo	36.33 %	5.99 %
Nb	39.22 %	5.59 %
Total Solar Power	1221 W/m^2 (89.91%)	137.67 W/m^2 (10.13%)

3.2 Improving Spectral Reflectance of Refractory Metals with Periodic High-Index/Low-Index Coatings

In this case high reflectance is desired at the front surface, so constructive interference of the reflected beams between the adjacent layers are created. To achieve such constructive interference, periodically altering high-low index layers are utilized. Since reflected beam experiences 180º phase change when encountered a high index layer and no phase change occurs in the interaction of the incident beam with low index layer all of the reflected become at the same phase at the front surface. A schematic for a periodic high-low index system is depicted in Fig. 3.3, which shows the reflected wave components in two separate colors depending on relative index of the adjacent medium to incident medium. Green components are the components which are reflected from a medium which has higher refractive index than the incident medium and it is the opposite for waves illustrated in orange. By adjusting the optical path in each layer through refractive index and thickness, reflected beams have the same phase at the front surface, thus high reflection is achieved.

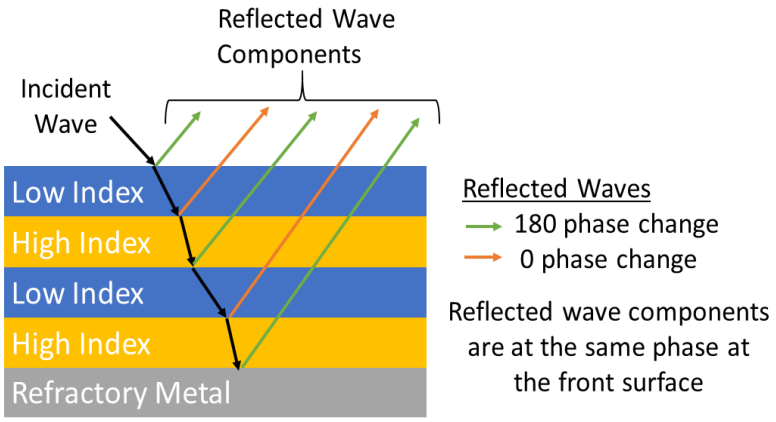

Fig. 3.3. Schematic of the high-low index periodic structures on which reflected wave components that either experiences 180° (green) or 0° (orange) phase change are visualized.

Location of such high reflection zone in the spectrum are tuned by controlling the thicknesses of the periodic layers. By setting the optical thickness of the layers to $\pi/2$ at a specified wavelength, high reflection around that wavelength are achieved. Relationship between the optical and geometrical thickness of a layer is given in Eq. (3.2) where, 'δ' is the optical thickness, 'n' is the refractive index, 'k' is the extinction coefficient, 'd' is the geometrical thickness, 'ϑ_r' is the angle of refraction and 'λ' is the wavelength. From Eq. (3.2), thickness is solved to determine required film thicknesses to achieve high reflection zone around the selected wavelength. We used lossless materials in 300-3000 nm spectrum to obtain geometrical thicknesses, 'd', from Eq. (3.2). A periodic filter is designed on top of Tungsten, to generate high reflectance around 600 nm with 9 layers of alternating TiO_2-SiO_2 layers wavelength for which both schematic and structure is depicted in Fig. 3.4(a) and 3.4(b).

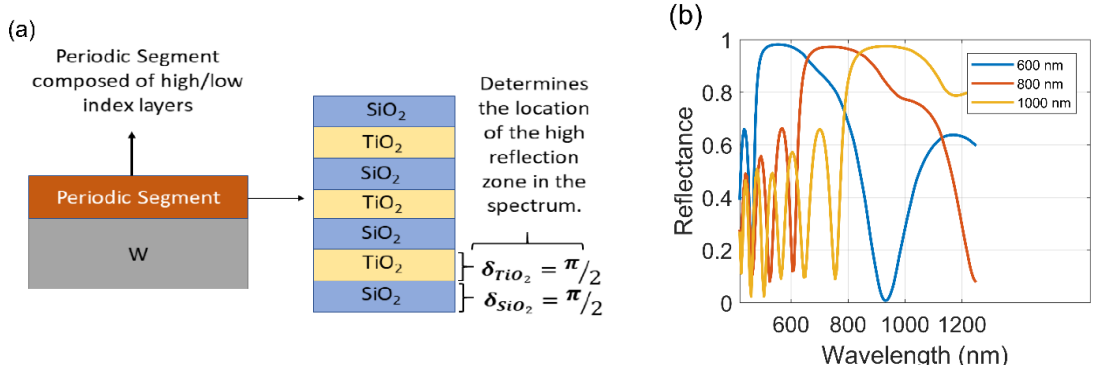

Fig. 3.4. a) A schematic representation for the simulated structure in which periodic high-low index layers are coated on tungsten on top of W. Coating materials are selected as TiO2 as high index and SiO2 as low index. Optical thicknesses of the layers are set to $\pi/2$ and central wavelengths are selected as 600, 800 and 1000 nm. b) Reflectance of the structure for which scheme is given in Fig. 3.4(a) at the specified central wavelengths. High reflectance zones are achieved around wavelengths which are slightly shifted from central wavelengths due to interference with W at the bottom.

$$\delta = \frac{(n - ik) * d * \cos(\vartheta_r)}{\lambda}$$

Table 3.2. Thickness of TiO_2 and SiO_2 layers for various central wavelengths and wavelengths at which reflectance of individual segments drop below 95%.

Central Wavelength (nm)	*Thickness (nm)*		*High Reflectance Bounds (nm)*
	TiO_2	SiO_2	
450	35	76	370-575
500	41	85	415-650
600	51	102	520-725
750	66	128	625-985
800	71	137	705-980
900	81	154	755-1200
1000	90	172	890-1255
1200	109	207	1055-1565
1500	138	259	1295-2065
2000	189	347	1675-2780
2200	210	383	1815-3100

In Fig. 3.4(b) reflectance of periodic TiO_2-SiO_2 segments with central wavelengths of 600, 800 and 1000 nm are plotted against wavelength. As shown, high reflectance zones around specified wavelengths are achieved with different segments. In this filter, TiO_2 is selected as high index and SiO_2 is selected as low index materials and geometrical thicknesses are reported in table 3.2. Although optical thicknesses are set to $\pi/2$ at the specified wavelengths, center of the high reflection zones shifted to slightly lower wavelengths because of the interference with the W at the bottom. However, bandwidths of the high reflectance zones for these individual designs are extremely low when compared to the bandwidth of the solar irradiance. Such a filter reflects only a small portion of the incident radiation and it is in need of bandwidth increase. To increase the bandwidth, several periodic segments are stacked. Each segment in this stack is composed of periodic layers. To obtain broad spectral reflection, these segments are stacked, each of which has a different central wavelength. In section 3.4, effects of central wavelengths of the segments are discussed in detail. Before the discussion of the influence of design parameters on the broadband reflectance, in Fig. 3.5(a) to 3.5(d), spectral response of periodic segments, which have 7 layers of TiO_2 and SiO_2 on top of W, Ta, Mo and Nb layers, which are designed to have reflectance peaks around 450, 500, 750, 900, 1000, 1200, 1500, 2000 and 2200 nm are demonstrated and thicknesses of the layers in the segments are depicted in table 3.2. Central wavelengths are determined by considering the bandwidth of the individual

segments and effects on the reflectance in broadband spectrum. As shown in Fig. 3.4(b) each segment's reflectance decreases at distant wavelengths. We started with a segment, with central wavelength of 450 nm, which creates high reflectance zone above 95 % from 370 nm to 575 nm which is reported in table 3.2. We selected the next segment's central wavelength such that its reflectance is above 95% around 575 nm, therefore spectral reflectance of the resulting structure does not drop below 95% and continuity of the bandwidth of high reflectance is achieved. For each segment, wavelengths at which reflectances dropped below 95% are reported in table 3.2. In this particular design, the reflectivity in each segment generates a high reflection zone with a reflectance above 95 % in a spectral interval of few hundreds of nm width. One can select a higher percentage, but it will result in a higher number of segments in Table 3.2. Other segments are added in this manner and high reflectance in 300-3000 nm spectrum is achieved. During the determination, we also considered the effect of the segments at distant wavelengths, e.g. a segment with central wavelength of 1000 nm can create a sharp reflectance dip at 400 nm when stacked together with other segments. To decrease the number and magnitude of reflectance dips we shifted central wavelengths of the existing segments and added segments with central around the reflectance dips, by obeying the continuity of the bandwidth rule discussed above. It is shown that highly broadband reflectance is obtained in 300-3000 nm spectrum for coated W, Ta, Mo and Nb. Magnitude and location of the sharp dips are varied for structures because of the different interference of the segments with the bottom metallic layer. Improvement percentages over 500-nm W, Ta, Mo and Nb by these filters in terms of absorbed powers are also reported in Table 3.3.

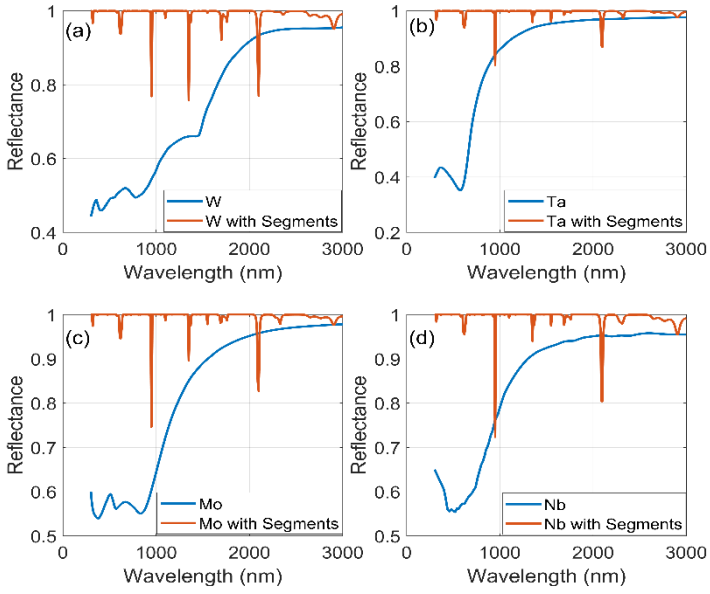

Fig. 3.5. Spectral reflectances of metals on which periodic segments designed at 450, 500, 750, 900, 1000, 1200, 1500, 2000 and 2200 nm are coated and compared to reflectivity of W, Ta, Mo and Nb respectively.

Table 3.3. Comparison of average absorption percentages of uncoated and coated W, Ta, Mo and Nb with periodic segments for which spectral reflectances are depicted in Fig. (5).

Average Absorptions & Improvements					
Spectrum Interval		W	Ta	Mo	Nb
300-1500 nm	Uncoated	44.2 %	37.4 %	36.3 %	39.2 %
	Coated	0.5 %	0.15 %	0.10 %	0.13 %
	Absorption Reduction	98.7 %	99.5 %	99.7 %	99.6 %
1500-3000 nm	Uncoated	13.1 %	3.54 %	5.99 %	5.59 %
	Coated	1.5 %	0.59 %	0.65 %	0.06 %
	Absorption Reduction	87.8 %	83.3%	89.13 %	84.91 %

As shown in Table 3, reduction rate of absorbed powers of refractory metals are around 99 % for 300-1500 nm spectrum and 85 % for 1500-3000 nm spectrum when coated with periodic segments.

3.3 Impact of Number and Structure of the Segments on Spectral Reflectance

Several design parameters, visually depicted in Fig. 3.6, including number of segments, layer numbers in the segments and materials in the segments are analyzed in this section. Effect of number of number of segments are compared by adding the above segments one by one on top of the W, Ta, Mo and Nb films and results are given in Fig. 3.7(a). Although average reflectivities converge to same levels for 8 segments, higher average values are obtained with Ta, Mo and Nb when compared to W at less number of segments. Reason of higher average at less number of segments with Ta, Mo and Nb is the littleness of the absorption of these metals when compared to W

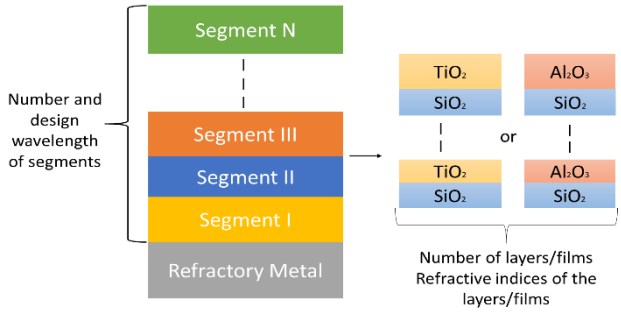

Fig. 3.6. Schematic for the proposed structures which are composed of several periodic high-low index segments. Possible design parameters that influence the performance of the structure, number of segments, central wavelength of the segments, number of layers in the segments and materials, are also demonstrated.

Number of layers in the segments are compared for various structures in Fig. 3.7(b). Not an increasing trend is observed with increasing number of layers, which indicates that number and magnitude of reflectance dips increase. From Fig. 3.7(b) it is shown that average reflectances are smaller for 5 and 7 layers when compared to 4 and 6 layers. Reason of such behavior is reflectance dips whose negative effects are enhanced when layer numbers are 4 and 6. Reason of such negative effects is discussed in detail in the next paragraph.

The reflectance dips in Fig. 3.5 resemble to the response of a Fabry Perot filter [chapt. 5 of Ref. 194]. Fabry Perot filters are composed of periodic high-low index films, each quarter wavelength thick, separated by a half wavelength thick film and designed to transmit incident wave at the selected wavelength and reflect the incident waves around that wavelength. Proposed filters consist of periodic high -low index segments which is similar to Fabry Perot filters. For demonstration, structures of Fabry Perot filters, their responses and approximate formation of those in proposed filters are depicted in Fig. 3.8(a), 3.8(b), and 3.8(c) respectively. Response of the Fabry Perot filters with demonstrated configuration in Fig. 8(a), for varying substrates with refractive indices of 1.4, 2 and 3 is depicted in Fig. 3.8(b). It is observed that bandwidth or magnitude of high reflectance zones around the transmission gap wavelength are not altered with varying refractive index of the substrate but decreases the magnitude of the transmission at the central wavelength of 500 nm. This indicates that back reflection from bottom layers seem to be highly affecting the transmission behavior at the central wavelength.

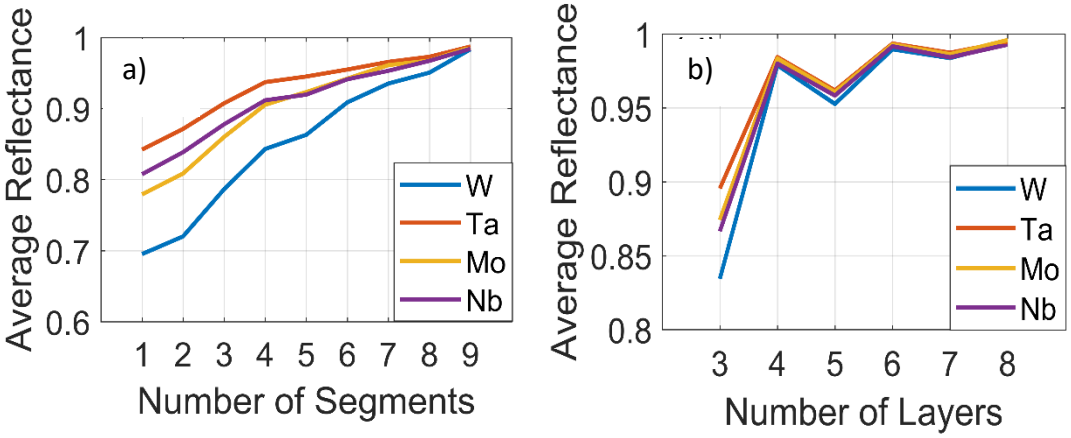

Fig. 3.7. a) Average reflectance against the number of segments for which an increasing trend is observed with increasing number of segments. Central wavelengths of the segments are 450, 500, 750, 900, 1000, 1200, 1500, 2000 and 2200 nm. b) Average reflectance against the number of layers per segment. Average reflectance remains 99% levels after 6 layers.

As shown, trends observed in the responses of Fabry Perot filters are very similar to responses observed in discussed broadband filters in terms of reflectance dips. To make an easier comparison, we consider a filter that is composed of periodic segments with central wavelengths of 400 nm 600 nm on top of 500 nm tungsten and Si substrate. In this filter top layer is selected as TiO_2, so when there are odd number of layers bottom layer of each segment becomes TiO_2. This creates TiO_2-TiO_2 interfaces at intersection locations of two segments. When such interface occurs, this TiO_2-TiO_2 interface acts as an almost perfect single half wavelength layer at 490 nm wavelength between two different periodic segments, because optical thicknesses of these two layers add up to π at 490 nm wavelength. Formation scheme of the half wavelength in between periodic segments is depicted in Fig. 3.8(c). In Fig. 3.9(a), spectral reflectance of Fabry Perot filter designed at 490 nm wavelength and filter with periodic segments at 400 and 600 nm, at which TiO_2-TiO_2 interface is formed and optical thicknesses add up to π on top tungsten is compared. As depicted in Fig. 3.9(a), similar reflection drops at 490 nm wavelength are observed. High reflectance zones around 490 nm is present at each filter with higher reflectances around 350 nm at the filter because, filter has periodic segment designed at 400 nm whereas periodic reflector of Fabry Perot is at 490 nm. Number of layers in the segments are 5 in each filter.

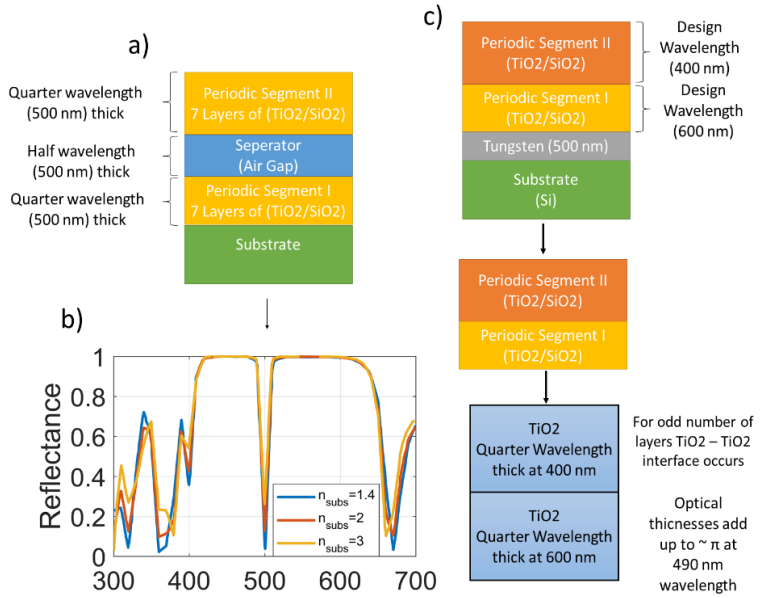

Fig. 3.8: a) Schematic structure of a Fabry Perot filter which generates transmission gap at 500 nm wavelength. b) Reflectance of the structure depicted in Fig. 8(a) on substrates with refractive indices of 1.4, 2 and 3. Change in refractive index effects the magnitude of the transmission gap. c) Scheme for a filter in which two segments creates a half wavelength thick layer. When bottom layer of periodic segment II and first layer of periodic segment I are TiO_2, optical thicknesses add up π at 490 nm wavelength and thus a single half wavelength thick layer is formed, which makes the structure an approximate Fabry Perot filter.

As mentioned, segments of the periodic filter depicted in Fig. 3.9(a) starts with TiO_2 and last layer of each segment becomes TiO_2 for odd number of layers. For even number layers SiO_2 become the last layer and SiO_2-TiO_2 interfaces occur instead of TiO_2-TiO_2. In Fig. 3.9(b), spectral reflectance of the filter in consideration with 4 and 5 layers are illustrated. As shown, when layer number is 5 reflectance drop occurs at 490 nm due to TiO_2-TiO_2 interface, whereas it is prevented when layer number is 4. This trend explains the reason why average reflectances are reduced for odd number of layers in Fig. 3.7(b). When the order of the layers is changed, starting with SiO_2 instead of TiO_2 and average reflectances are plotted against number of layers, an increasing trend is observed. Since segments' central wavelengths are kept identical, this result indicates that SiO_2-SiO_2 interfaces do not form approximate Fabry Perot filters as good as TiO_2-TiO_2 interfaces.

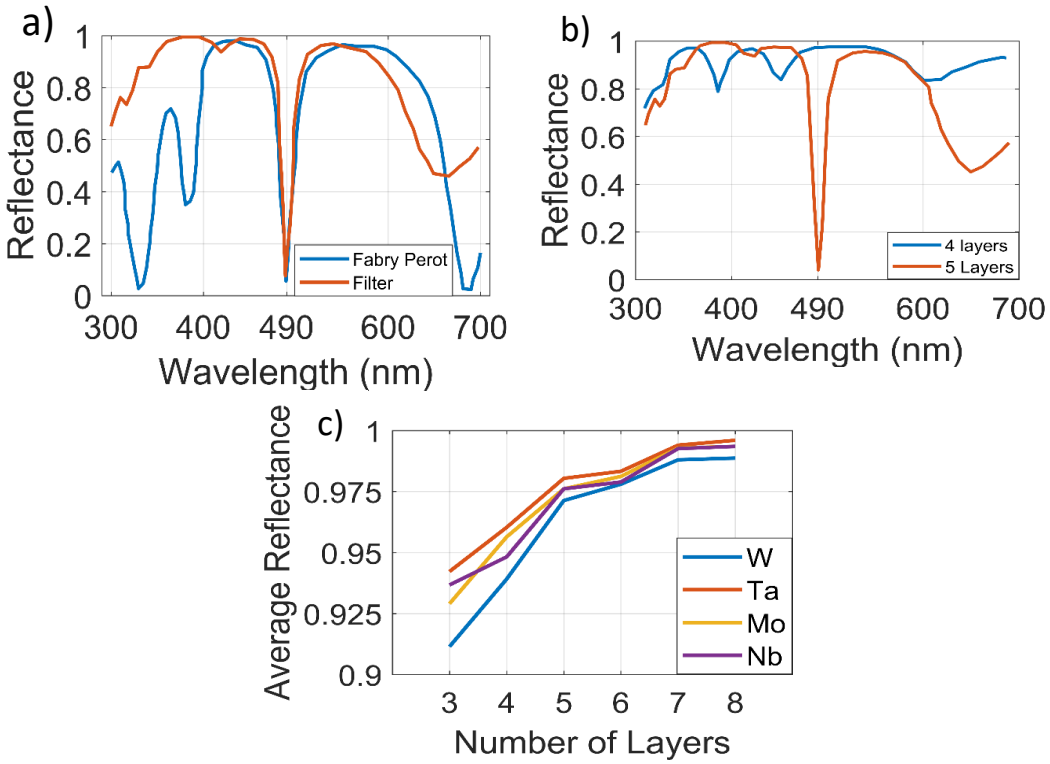

Fig. 3.9. a) Spectral reflectance of Fabry Perot filter designed at 490 nm and optical filter composed of two periodic segments with central wavelengths of 400 and 600 nm wavelengths on top of 500 nm thick tungsten. Similar spectral reflectance behaviors are observed. b) Spectral reflectances of the filters with periodic segments designed at 400 and 600 nm wavelengths on top of 500 nm thick tungsten. When layer number in the segments are 5, optical thicknesses of TiO_2 layers add up to π and form a half wavelength thick medium, whereas when number of layers are 4 half wavelength thick medium is not formed. c) Average reflectance of the filters for which average reflectances are reported in Fig. 7(d) when top layers of the segments are TiO_2 which creates approximate Fabry Perot effects due to TiO_2-TiO_2 interfaces. When top layers are changed to SiO_2 increasing average reflectance with increasing number of layers shows that effect of reflectance dips in the presence of SiO_2-SiO_2 interfaces on average reflectance are decreased.

We also investigated the performance of thin-film filters by substituting Al_2O_3 instead of SiO_2. Al_2O_3 has higher melting point and Young's modulus than SiO_2 which makes it a better candidate for coatings in extreme environments. Such a change degrades the optical performance of the coatings since refractive index of Al_2O_3 is less than SiO_2. Due to the decreased refractive index ratio of the segments, shown in Fig 3.10(a), both magnitude and bandwidth of the reflection zone created by a single segment is reduced which is illustrated in Fig. 3.10(b). Such reduction in reflectance of the segments rises the need for higher number of segments to cover 300-3000 nm spectrum interval. In Fig. 3.10(c), reflectance of segments with TiO_2 and Al_2O_3 at wavelengths 320, 370, 450, 500, 575, 660, 750, 860, 970, 1130, 1260, 1420, 1620, 1840, 2500 and 2580 nm, on top of 500-nm thick tungsten film. Average reflectance of the structure in 300-3000 nm spectrum is around 98% which is similar to previous structures. However, differently from TiO_2-SiO_2 segments, such broadband high reflectance is achieved by 16 segments. Absorbed powers are calculated for these structures with varying bottom metallic layers of W, Ta, Mo and Nb which are tabulated on table 3.4. When compared to results given in table 2, this structure absorbs more power than the structure which consists of TiO_2 and SiO_2.

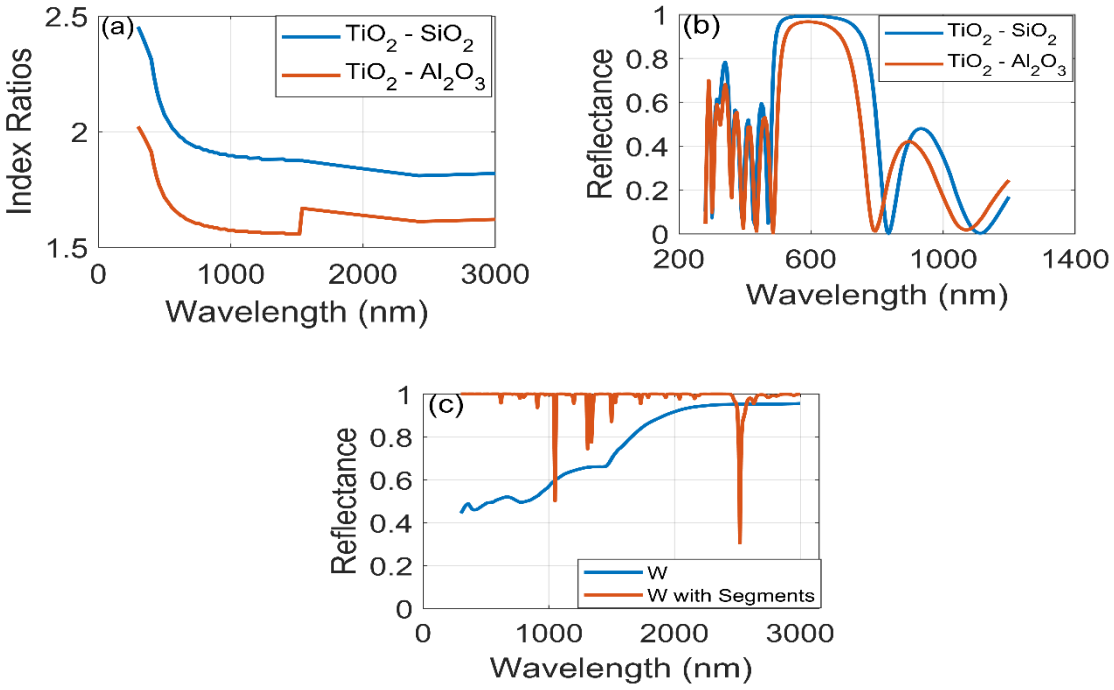

Fig 3.10. a) Ratio of the refractive indices of TiO_2-SiO_2 and TiO_2-Al_2O_3 in the spectrum interval of 300-3000 nm wavelength. b) Comparison of reflectances of TiO_2-SiO_2 and TiO_2-Al_2O_3 periodic segments for which structure with SiO_2 has reflectance with higher magnitude and bandwidth. c) Reflectance of W with 16 periodic TiO_2-Al_2O_3 segments for which average reflectance in 300-3000 nm wavelength is around 99%.

Table 3.4. Reduction rates of absorbed powers by segmented structures (TiO_2-Al_2O_3) with 500-nm W, Ta, Mo and Nb for spectral intervals of 300-1500 nm and 1500-3000 nm.

Spectrum Interval	Reduction Rates of Absorbed Powers			
	W	Ta	Mo	Nb
300-1500 nm	98.53 %	98.86 %	98.29 %	98.45 %
1500-3000 nm	91.90 %	81.48 %	87.73 %	81.93 %

As shown in Table 3.4, similar reduction rates with TiO_2-Al_2O_3 filters when compared to TiO_2-SiO_2 filters. However, reaching to such high reduction rates require higher number of segments than previous structures do.

Finally, in Fig. 3.11, the average reflectance of the structures for various incidence angles are demonstrated. As shown in Fig. 3.11, average reflectance of the structures reduces with increasing incidence angle. The maximum average reflectance is observed at 0° since high reflectance zones are designed for this angle of incidence

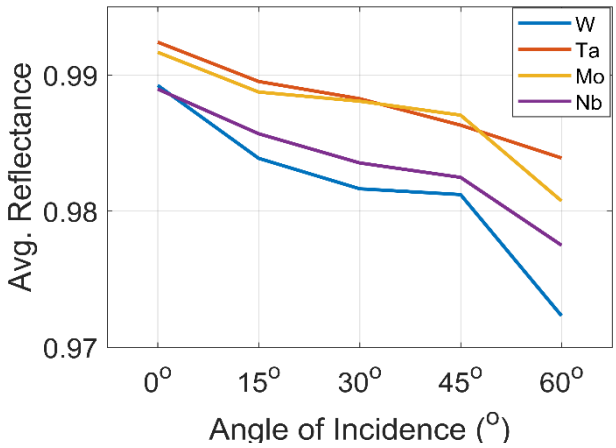

Fig. 3.11. Average reflectance of refractory metals coated with periodic segments, whose spectral behaviors are depicted in Fig. 3.5, for varying angle of incidence.

Although comparison for theoretical and experimental results are not reported, theoretical methodology applied in this work has been widely used for optical filter designs and experimentally verified in the literature [195-196]. The fabrication of a high number of segments with a high number of layers would be challenging, however fewer segments which include oxide layers can be fabricated by ion beam deposition which is currently used to produce very thin oxide multilayers [197]. A metal layer at the bottom can be coated via DC sputtering technique which can also be used to produce oxide layers on top of the refractory metal [195].

In real applications, effect of temperature on optical properties should also be considered. Temperature dependency of optical properties of the dielectrics in the devices brings a limit on operating temperature. In the literature it has been shown that optical properties of SiO_2 and Al_2O_3 do not vary significantly until 900 K and 1900 K levels respectively [198]. However, phase change in TiO_2, from anatase to rutile occurs at the temperatures around 900 K levels, results in changes in optical properties of TiO_2 in the visible spectrum. Therefore, structures in the manuscript can operate until 900 K temperatures according to studies reported in the literature on these materials. For operational condition beyond 900 K, other materials may be used with changes to designs based on the outlined methodology.

By designing broadband reflectors with refractory metals instead of soft metals like Ag, Au, Cu, or Al, more durable devices are obtained. Soft metals are vulnerable to scratches and other environmental damages which can alter the optical behaviors. Even if they are coated with hard protective layers such as SiO_2 or Al_2O_3 [84,199], several problems occur due to attempt of coating materials with higher hardness on softer materials [83-84,86]. When soft metal reflectors are replaced with refractory metals, broadband reflectors with higher durabilities are obtained.

4. ORIGINS OF THE BROADBAND ABSORPTION IN BLACK SILICON

In this chapter, I study the mechanisms of the broadband absorption enhancement in pure micro-structured silicon with random and deterministic textures. I considered texture geometry and doping concentration as major influential parameters on the absorptivity of the black silicon and linked those parameters to electromagnetic phenomena, which induce high field intensities. Random texture geometries, e.g. in Fig. 4.1(a), are analyzed by expressing them by random Gaussian surfaces and spectral characteristics are obtained. Surface geometry is characterized by root-mean-square (RMS) of surface height, h_{rms} and transverse correlation length l_c, shown in Fig. 4.1(c). Electromagnetic responses of those structures are analyzed by finite difference time domain (FDTD) [200] simulations. Then, spectral characteristics of random textures are compared to periodicity controlled deterministic patterns, Fig. 4.1(b) and 4.1(d) and the field distributions are calculated for analysis with FDTD [200]. In summary, geometry of randomly and deterministically textured black silicon structures are studied, results are analyzed based on field distributions. During the analysis, we considered the high field enhancement problem in black silicon as reciprocal of a waveguide problem in which multiple modes are supported throughout the geometry. In addition, high coupling in the transverse directions are observed in the analysis and coupling condition is estimated by adapting an effective wavelength method, which was originally proposed for optical antennas [201]. Findings show that overall field enhancement in the pure-silicon structure stem from these two different phenomena depending on the width of the features of the textures. These findings reveal the underlying physics of the broadband absorptivity enhancement in black silicon, which can aid the future studies in the field.

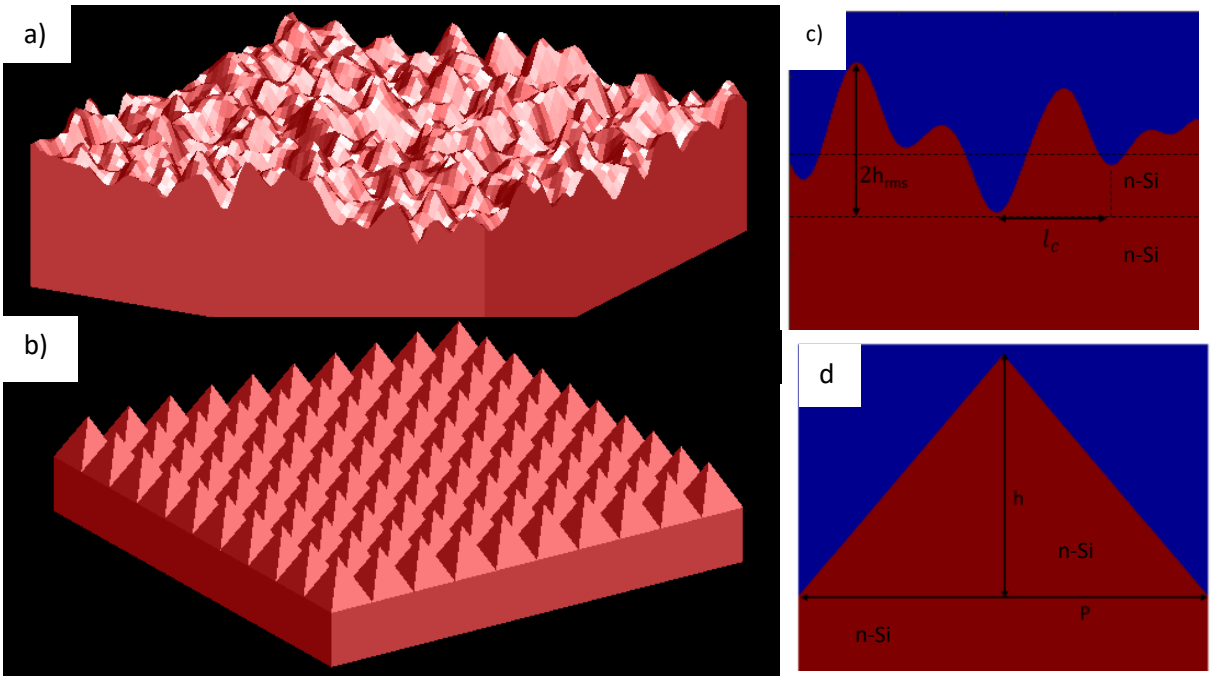

Fig. 4.1. a) Example 3D visual of random texture formed by random Gaussians. b) Example 3D visual of periodicity controlled deterministic texture. c) 2D scheme for random texture with geometric parameters. d) 2D scheme for deterministic texture with geometric parameters.

4.1 Methodology

In this section, methodology for random geometry formation and doped optical properties calculations is explained. Generated structures' electromagnetic response is computationally obtained in 0.3 – 3 μm spectrum interval. In section 4.2.1, random rough surface generation methodology is expressed. In the next section, 4.2.2, procedure for obtaining optical properties with doping is summarized.

4.1.1 Rough Surface Generation

A rough surface configuration shown in Fig. 4.1(c) is considered for explaining the random surface roughness effect. In this case, the roughness is characterized by a specified sigma RMS (σ) which is describing the height profile and is identical to standard deviation of a random variable and correlation length (L_c) which is defining frequencies of spatial variations

allowed over the surface. Large correlation length corresponds to small spatial frequencies and vice versa.

The integration of the power spectral density (PSD), which is the Fourier transformation of the surface height self-correlation function [202], over k-space results in the RMS of surface height. For a Gaussian surface, the roughness is randomly distributed with a PSD function, which follows a Gaussian distribution. In this study, Gaussian surface is described with the PSD [203] given as:

$$W = \frac{l^2 h_{rms}^2}{4\pi} e^{-\frac{k_p^2 l^2}{4}} \tag{4.1}$$

where l is the transverse correlation length, h_{rms}^2 is the surface height variance and $k_p^2 = k_x^2 + k_y^2$ is the wave-vector in the radial direction. These quantities are related to the correlation function by,

$$H(r)H(r+\delta) = h_{rms}^2 e^{\left(-\left(\frac{\delta}{l_c}\right)^2\right)} \tag{4.2}$$

where h_{rms} and l_c are RMS and correlation length values, respectively. r shows the positions on the surface and H is the surface height defined such that the rough surface structure can optionally generate textures as shown in Fig. 4.1(a).

Based on the previous experimental studies on black silicon, wet-chemical etching, which produces isotropic textures, is the most effective way for obtaining damage-free Si texture among various surface treatments including annealing and oxidation [204]. Isotropic distribution assumption is used in previously reported analysis of black silicon [205-206]. In line with those studies, random roughness surface profile is considered to be homogeneous and isotropic. In this study, isotropic gaussian rough surface approximation was utilized and $l_{cx}=l_{cy}=l_c$. A statistically homogeneous surface means the distribution of height is equally possible at any position within the surface. An isotropic surface is that the correlation function of surface heights is independent of the direction between two corresponding surface points' locations.

The roughness is generated by creating a matrix of uniform random numbers in k space (wave vector). The high frequency components (short wavelengths) which came from

conversion of time functions into waves of different frequencies and are rapidly changing in space, are removed, and the resulting values are transformed back to real space. In this case, a single import object (surface option) is used to define the entire object. The upper surface of this object is defined by a 2D matrix containing the surface height as a function of *x* and *y*. Then the surface matrix in k-space fills with uniform random numbers. It is then filtered according to the real roughness data extracted from atomic force microscopy (AFM) images to remove all high frequency components [207] and the actual surface is realized by applying the Fourier transform (FT) on the filtered k-space. The matrix is transformed back into real space, where the amplitude is corrected. Due to the way the Fourier transform is setup, the roughness will be periodic with period x, y span. This is convenient when using periodic boundary conditions. The import object is then added to the simulation. Reflection and absorption spectra have been determined in FDTD [180]. Periodic boundary conditions were used in the -x and -y directions, while perfectly matching layers (PML) were used in the lateral directions (-z direction). A broadband plane wave source was employed under normal incidence propagating. Reflection and transmission spectrum are evaluated with defining two monitors above and below the structure respectively. The absorption, *A*, is then calculated from reflection, *R*, and transmission, *T*, as *A =1-R-T*, in broadband spectrum. Field distributions over the geometry are also recorded in x-z plane to study the absorption spectra.

4.1.2 Optical Properties

Optical properties of the semiconductors can be modeled by Drude-Lorentz formalism, which is shown in Eq. (4.3),

$$\varepsilon(w) = \varepsilon_{\infty} - \frac{w_p^2}{w^2 + iwv} + \sum_{j=1}^{m} \frac{f_i}{w_j^2 - w^2 - i\Gamma_j w} \tag{4.3}$$

First term in Eq. (4.3), ε_{∞}, is the high frequency permittivity which stands for the contributions from high-frequency electronic transitions. Second term (Drude formalism) is the expression for free electron contribution to the frequency dependent permittivity where W_p is the plasma frequency and v is the relaxation frequency. Expressions for W_p and v are given in Eq. (4.4) and (4.5) respectively as,

$$w_p = \sqrt{\frac{4\pi N e^2}{m^*}} \tag{4.4}$$

$$\nu = \frac{e}{\mu_c m^*} \tag{4.5}$$

where N is the carrier concentration, e is the electron mass and m^* is the effective mass in Eq. (4.4) and μ_c is the mobility in Eq. (4.5). Last term in Eq. (4.3), Lorentz formalism, stands for the contributions to permittivity coming from lattice vibrations and interband transitions of bond electrons. In Lorentz formalism, f_j stands for oscillator strength, w_j for resonance frequency and Γ_j for damping factor.

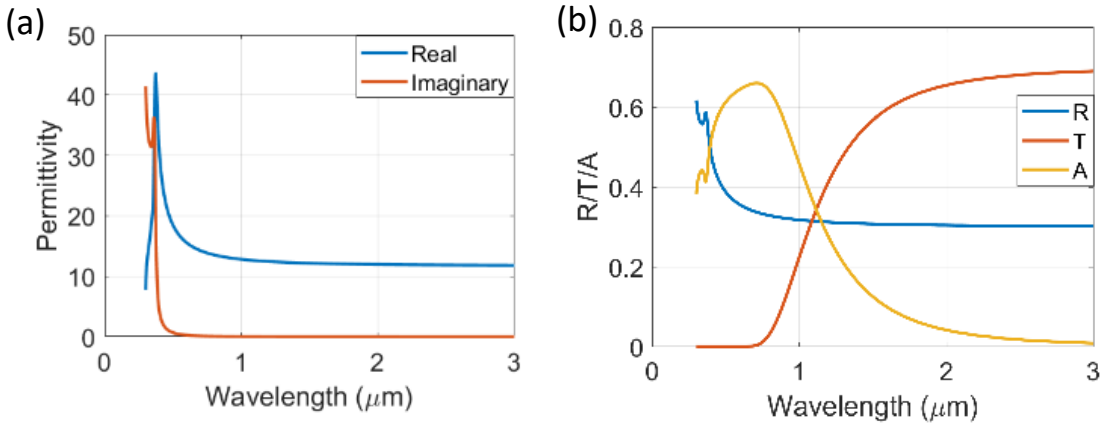

Fig. 4.2. a) Real and imaginary part of the permittivity of the silicon retrieved from [188]. b) Reflectance, transmittance and absorptance of Si film of finite thickness.

Drude formalism is sufficient to model the optical properties of Si for wavelengths longer than 3 μm, where optical properties are dominated by electron plasma of the material. However, to model the properties in wavelengths which are below bandgap energy of the Si, especially in visible spectrum, Lorentz term should be included to address the interband transitions. In Fig. 4.2(a) permittivity of the Si, retrieved from [188] is demonstrated and reflectance, transmittance and absorptance of Si film of finite thickness is shown in Fig. 4.2(b). As seen from Fig. 4.2(a), real part of the permittivity of the Si is almost constant after 1 um. However, it has distinct peak around 0.5 um with finite imaginary part, due to effects of bounded electrons, which give rise to below bandgap absorption as shown in Fig. 4.2(b). Therefore, Drude-Lorentz formalism is required to model the optical properties in 0.3 – 3 um spectrum interval.

To obtain a Drude-Lorentz model for optical properties of Si, we fit Eq. (4.3) to permittivity data given in Fig. 4.2(a) and obtained the ε_{∞}, W_p, ν in Drude term and other Lorentz parameters. We set the number of Lorentz oscillators to 6. Fitting parameters are given in Table 4.1 and reference and fitted permittivity, as well as the spectral reflectance values are compared in Fig. 4.3. Reflectance is obtained by Fresnel equation given in Eq. (4.6).

Table 4.1. List of parameters and their values for fitting Drude-Lorentz formalism given in Eq. (3) to optical properties of Si given in [188]

Parameter	**Value**
ε_{∞}	5 [F/m]
W_p	0.5006 [eV]
ν	$7.33*10^{-7}$ [s]
$f = [f_1:f_6]$	[1.33, 0.18, 1.61,1.49,1.53]
$w = [W_1:W_6]$	[4.50, 3.40,3.53,3.82,4.50,4.1]
$\Gamma = [\Gamma_1:\Gamma_6]$	$[2.73*10^{-5}, 0.0025, 0.0874, 2.36*10^{-5}, 0.064]$

$$R(w) = \left| \frac{\sqrt{\varepsilon(w)} - 1}{\sqrt{\varepsilon(w)} + 1} \right|^2 \tag{4.6}$$

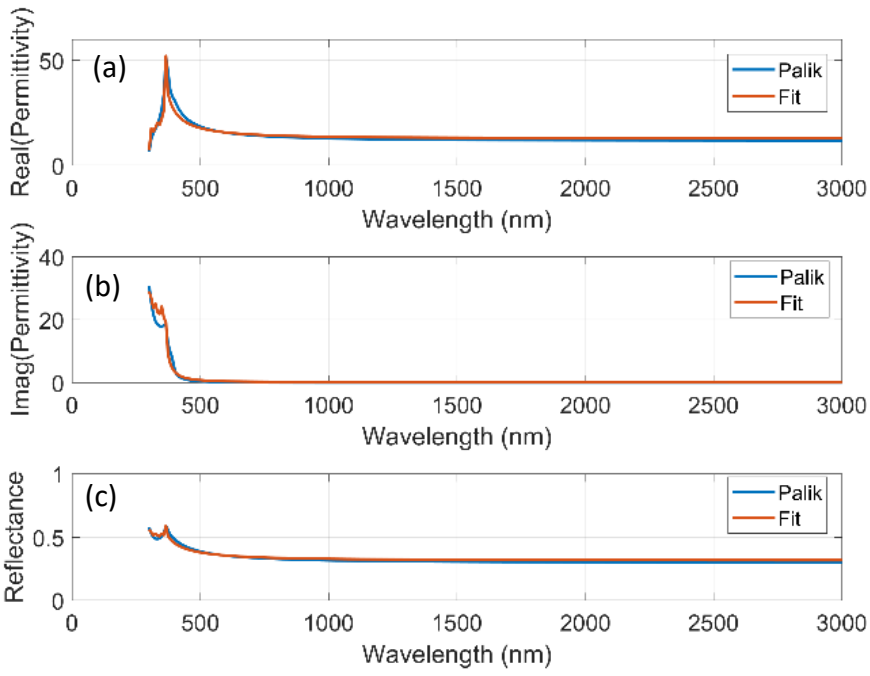

Fig. 4.3. a-b-c) Comparison of real and imaginary part of the permittivity given in [188] and fit values, and reflectance obtained from it and the fit.

As shown in Fig. 4.3, reference optical properties and obtained properties by fitting agrees well and similar reflectance is obtained over the spectrum of interest. From the Drude-Lorentz equation obtained for pure Si, optical properties of doped silicon for various doping concentrations is obtained.

Doping may significantly alter the optical properties depending on the doping concentration. Optical properties are linked to doping level by carrier concentration in the material. As shown in Eq. (4.4), carrier concentration has proportional relationship with the plasma frequency. In addition, it is also linked to mobility. Both plasma frequency and mobility are in the Drude part of the model, therefore, by modifying the Drude term in Eq. (4.3), permittivity for doped Si is obtained. During the calculations, we assumed constant effective mass for various doping levels.

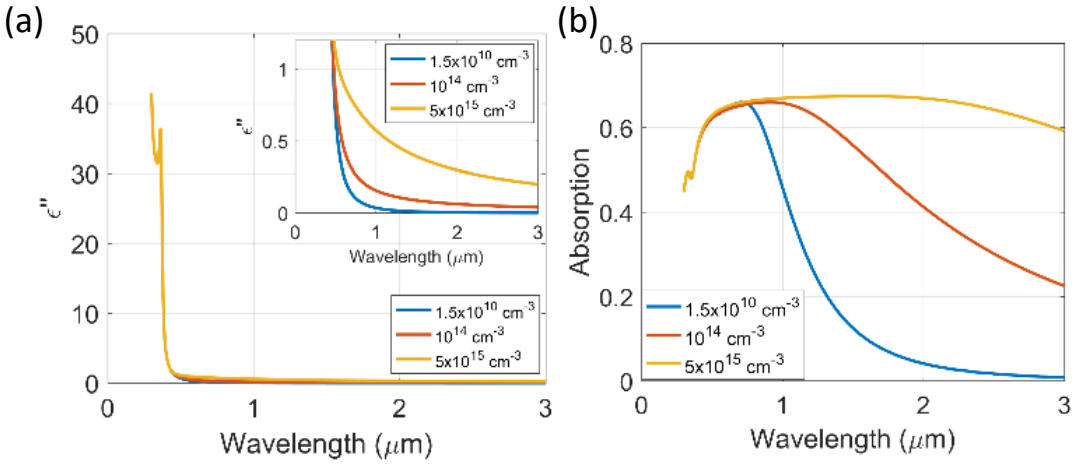

Fig. 4.4. a-b) Imaginary part of the permittivity of Si with doping concentrations of 10^{14}, $5x10^{15}$, 10^{16}, and $5x10^{16}$. c) Absorptivity of silicon with carrier concentrations of 10^{14}, $5x10^{15}$ and $5x10^{16}$ cm^{-3}.

Effect of carrier concentration on plasma frequency is evaluated as given in Eq. (4.4). To include the effect of carrier concentration on mobility, experimental values reported in [208], for mobility with respect to carrier concentration, are used in the calculations. We assumed the initial carrier concentration of Si is approximately 1.5 x 10^{10} cm^{-3} and obtained optical properties for n-type doping with different carrier concentrations. In Fig. 4.4, imaginary part of the permittivity of Si with n-type doping concentrations of 10^{14}, $5x10^{15}$, 10^{16}, $5x10^{16}$.

With the increasing carrier concentration, considerable increase in imaginary part occurs, as shown in Fig. 4.4(a), therefore loss in the material increases. Increased loss in the material results in elevated absorptance/emittance even in the bulk form. As shown, imaginary part of the permittivity is not changed significantly around 3 μm and shorter wavelengths with carrier concentration of 10^{14} cm^{-3}. In Fig. 4.4(b), spectral absorptance of Si with the selected

doping concentration is demonstrated. As seen, absorptance in broadband spectrum is significantly improved when carrier concentration is increased from 10^{14} to $5x10^{15}$ cm^{-3}. These findings show that even low doping concentrations, give rise to elevated absorptance/emittance in silicon. When combined with surface roughness/patterns, absorption is further improved by increased coupling with the incident waves and the structure. Absorption of textured structures, *A(λ),* are obtained by

$$A(\lambda) = \oiint_S \left(|E(\lambda)|^2 \times \sigma(\lambda) \right) \cdot ds \tag{4.7}$$

where $|E(\lambda)|^2$ is the electric field intensity in the geometry and $\sigma(\lambda)$ is the optical conductivity and dependent on the complex part of the dielectric permittivity, $\varepsilon = \varepsilon' + i\,\varepsilon''$, as

$$\sigma(\lambda) = 2 \times \pi \times f \times \varepsilon''(\lambda) \tag{4.8}$$

4.2 Results & Discussions

First, random textures with varying *l* and *h* are formed with *p* = 4 μm for which geometries are depicted in Fig. 4.5 and spectral absorption of those geometries are shown in Fig. 4.6(a). Doping concentration of silicon is fixed to 10^{14} cm^{-3}, for which calculation of the corresponding optical properties are described in section 2b. As seen in Fig. 4.6(a), for doping concentration of 10^{14} cm^{-3} near unity absorption is observed in 0.3 – 1 μm spectrum interval for varying correlation lengths and RMS heights when *p* =4 μm. However, high absorptance is decreased to 30 % at longer wavelengths and approach to absorption of smooth film. Such difference over the spectra is attributed to dispersion in optical conductivity where $\sigma(\lambda=1\ \mu m) \approx 10^{14}$ and $\sigma(\lambda=2\ \mu m) \approx 10^{13}$. $|E(\lambda=0.5\ \mu m)|^2$ distributions over the film and texture with $l = 0.2\ \mu m$, $h = 0.6\ \mu m$, geometry depicted in Fig. 4.5(a), are shown in Fig. 4.6(b) and 4.6(c) respectively. As shown in Fig. 4.6(b), uniform distribution of the fields inside the Si is observed when the surface is smooth. Unreflected fields penetrate to the silicon and physical phenomena at the interface can be explained by Fresnel reflections. However, in the case of textured surface, high field enhancements localized near the edges of the individual pyramid-like textures, are observed as shown in Fig. 4.6(c), which are called as side modes throughout the manuscript. As seen, those side modes give rise to higher fields inside the Si spikes, thus lead to elevated absorption. Similar side modes are also observed at different wavelengths in 0.3-3 μm interval.

It indicates that such side modes occur in broadband spectrum when the Si surface is textured and responsible from broadband absorption enhancement. To explore the effect of roughness dimensions on the absorption, field distributions are also analyzed for the geometry depicted in Fig. 4.5(b), which has less peaks and dips in the geometry due to the increased correlation length. In other words, texture in Fig. 4.5(a) has more spikes with small widths, whereas texture in Fig. 4.5(b) has less spikes with wider widths.

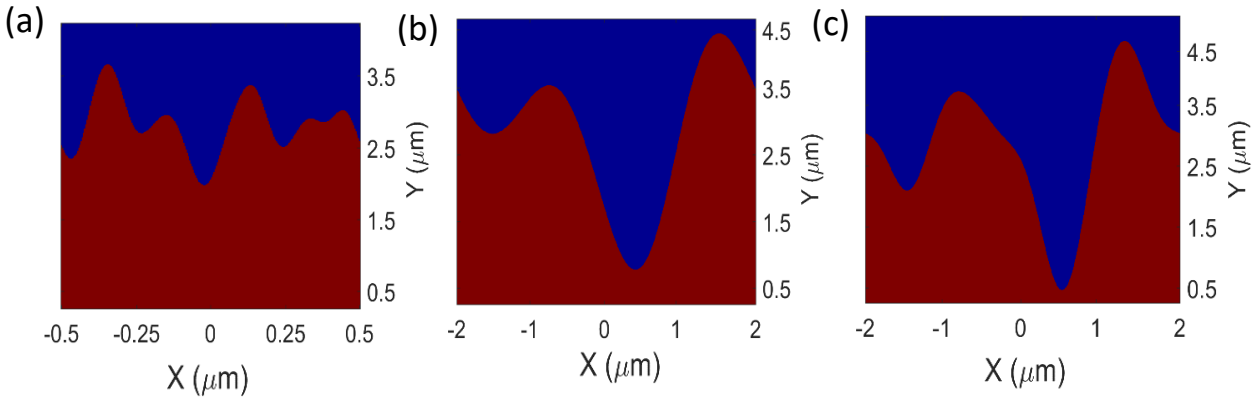

Fig. 4.5. a) An example random texture generated by setting l =0.1 μm , h_{rms} =0.3 μm, p = 1 μm. b) An example random texture generated by setting l =1.1 μm , h_{rms} =0.8 μm, p = 4 μm. c) An example random texture generated by setting l =0.6 μm , h_{rms} =0.8 μm, p = 4 μm.

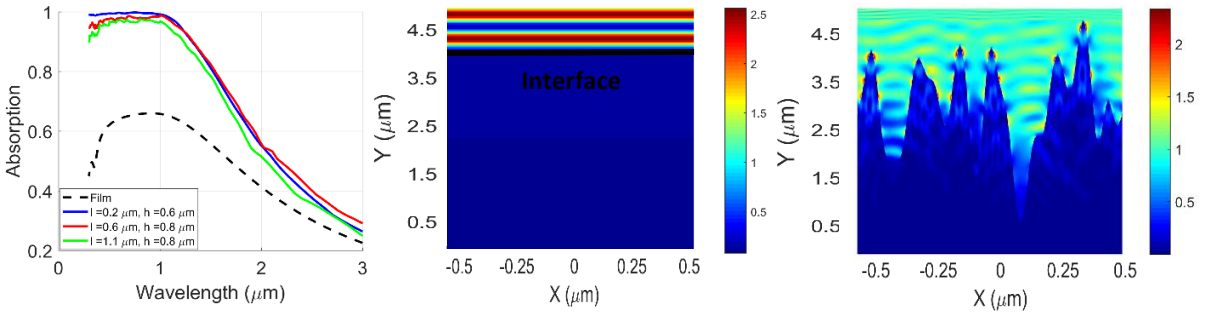

Fig. 4.6. a) Comparison of spectral absorption of untextured (film) and textures silicon with varying l and h_{rms}. b) $|E(\lambda)|^2$ distribution of untextured Si. c) $|E(\lambda)|^2$ distribution of textured silicon with l =0.1 μm and h_{rms} =0.3 μm.

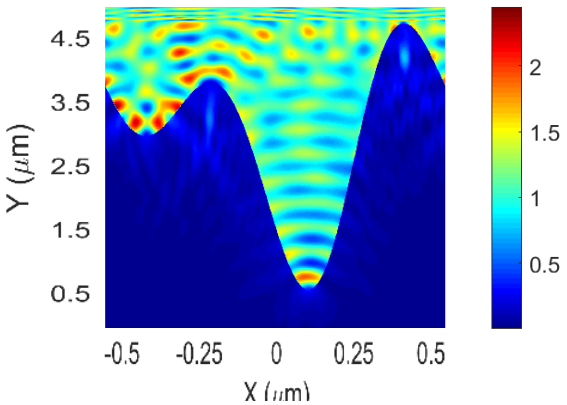

Fig. 4.7. $|E(\lambda=0.5\ \mu m)|^2$ distribution of the texture with l =1.1 μm , h_{rms} =0.8 μm at λ =0.5 μm.

Although no significant difference between textures with varying *l* and *h* are observed at longer wavelengths, slight decrease in absorption in visible spectrum is observed for increased *l*. To analyze, $|E(\lambda=0.5\ \mu m)|^2$ distribution for the texture with $l = 1.1\ \mu m$, $h = 0.8\ \mu m$ is shown in Fig. 4.7.

As seen in Fig. 4.7, side modes also occur in this texture with slightly reduced field intensities inside the spikes. It shows that field enhancement by the side modes are dependent on the width of the individual triangles. Increased widths lead to reduced intensity, thus resulting in decreased absorption. Effect of doping concentration on the spectral distribution and corresponding spatial absorption profiles for doping concentrations of 10^{14} and $5x10^{15}$ cm^{-3} are also shown in Fig. 4.8. As shown in Fig. 4.8(a), spectral absorption is significantly enhanced with increased doping concentration especially at longer wavelengths. $|E(\lambda)|^2 x\sigma(\lambda)$ distributions given in Fig. 4.8(b) and 4.8(c) for N =10^{14} and $5x10^{15}$ cm^{-3} also shows that spatial distribution profile inside the texture is not significantly altered by *N*.

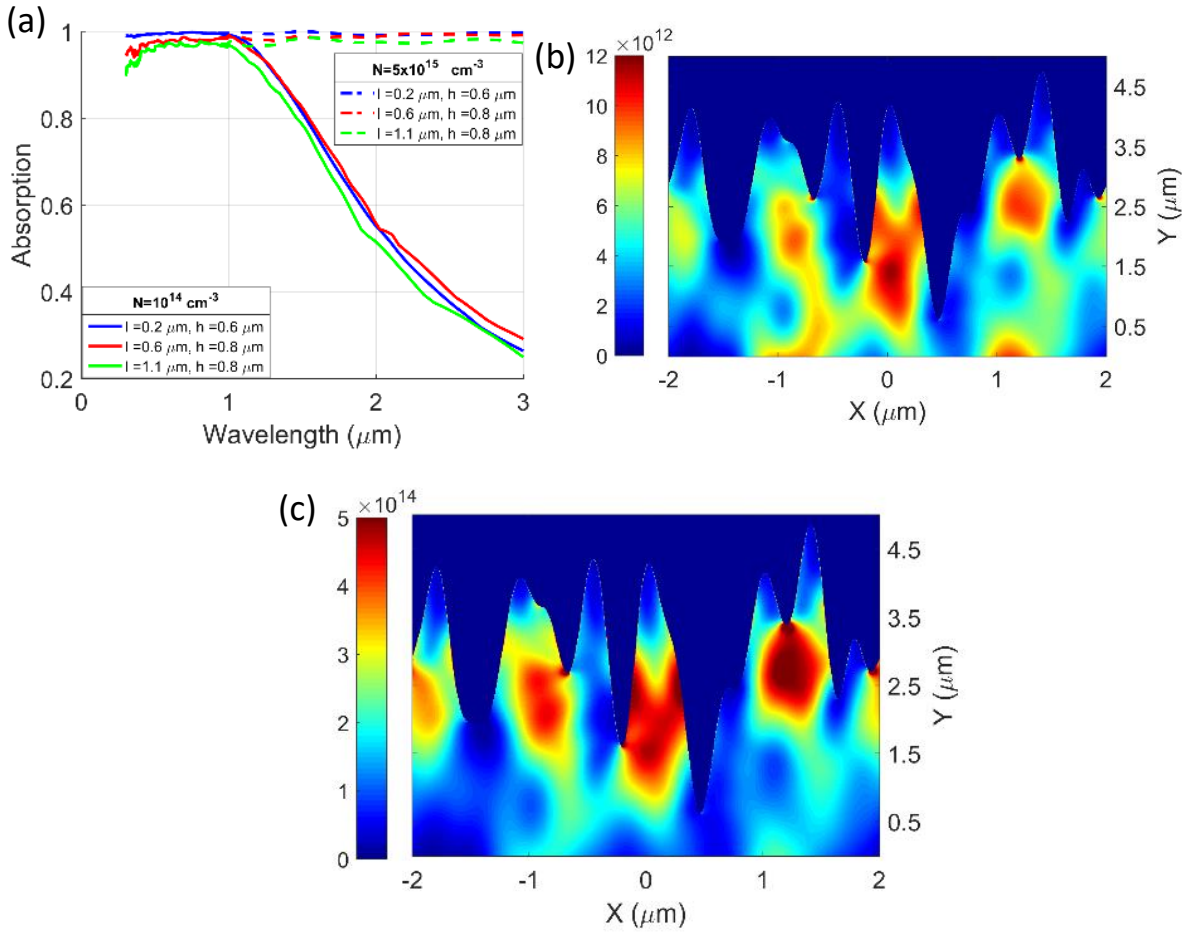

Fig. 4.8. a) Spectral absorptions of random textures for N =10^{14} and $5x10^{15}$ cm^{-3}. b-c) Spatial absorption profiles for N =10^{14} and $5x10^{15}$ cm^{-3}.

However, differently from N =10^{14} cm^{-3} case, fields absorbed more on the upper segment of the texture due to increased attenuation with increased ε''(λ), therefore σ(λ), when N is set to 5x10^{15} cm^{-3}. Finally, spectral absorption of a random texture is compared to deterministic textures with varying periodicities in Fig. 4.9(a). $|E(\lambda=0.5\ \mu m)|^2$ is also depicted in Fig. 4.9(b).

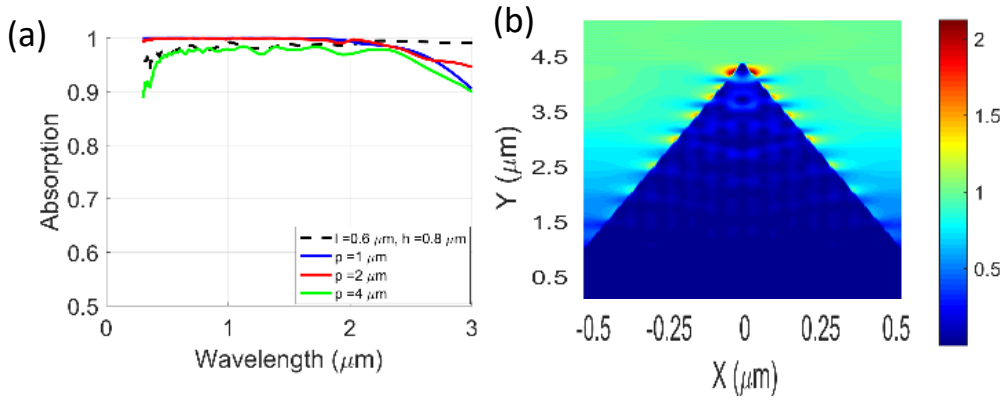

Fig 4.9. a) Absorption of a random texture and deterministic texture with varying p for N =5x10^{15} cm^{-3}. b) |E(λ=0.5 μm)|^2 distribution for the deterministic texture with p =1 μm.

Results depicted in Fig. 4.9(a) shows that spectral absorption of the random textures are very similar to previously reported experimental results [29-31]. Also, absorption of deterministic textures is similar to random textures' and are not very sensitive to periodicity in 0.3-3 μm spectrum, except the visible spectrum. Similar change in the visible spectra is also reported for random textures and attributed to reduced field intensity when texture widths are increased. In addition, field distribution for the deterministic texture with p =1 μm shown in Fig. 4.9(b) shows that side modes are also supported in deterministic textures. such similarity in absorption spectrum and field distributions allow us to use deterministic textures to understand underlying mechanisms in textured silicon. For analysis, deterministic textures with varying dimensions in broadband spectrum are analyzed.

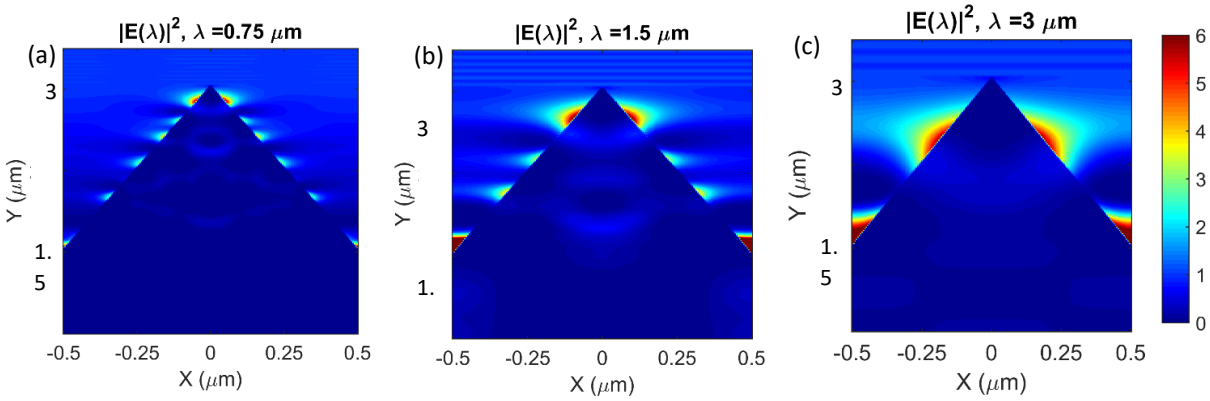

Fig. 4.10. a-b-c) |E(λ)|^2 at wavelengths of 0.75, 1.5 and 3 μm for the triangle dimensions of p =1 μm, h =3 μm and carrier concentration of 10^{14} cm^{-3}.

In the light of reported results until this point, it is found out that high absorption in broadband spectrum stem from local field enhancements which occur near the edges of the features. Both in random and periodic textures, such side modes are observed. Analysis reveal that field intensity of the side modes are dependent on the width of the individual spikes and are reduced with increased width. Absorption profiles inside the silicon are found to be insensitive to doping concentration. Finally, it is shown that deterministic textures exhibit similar absorption characteristics compared to random textures.

To study the underlying mechanism that give rise to side modes, further analysis is carried out with deterministic textures. Deterministic textures are chosen to avoid interference effects in random textures therefore, to be able to characterize the side modes occurring in individual features. $|E(\lambda)|^2$ and $|E(\lambda)|^2 \; x \; \sigma(\lambda)$ distributions over the deterministic textures are considered for the analysis.

In Fig. 4.10, $|E(\lambda)|^2$ for $\lambda = 0.75$ µm, $\lambda = 1.5$ µm and $\lambda = 3$ µm is demonstrated. p and h of the triangle are set to 1 µm and 3 µm respectively and N is set to 10^{14} cm^{-3}. As seen, distinct local field enhancements on the edges of the triangle are observed. At each wavelength, highest field intensities are obtained near the top of the triangle. However, number of local field enhancements on the edges of triangle differ for each wavelength. Those distinctive regions also exist inside the triangle, as shown in $|E(\lambda)|^2 \; x \; \sigma(\lambda)$distributions depicted in Fig. 4.11 for selected wavelengths.

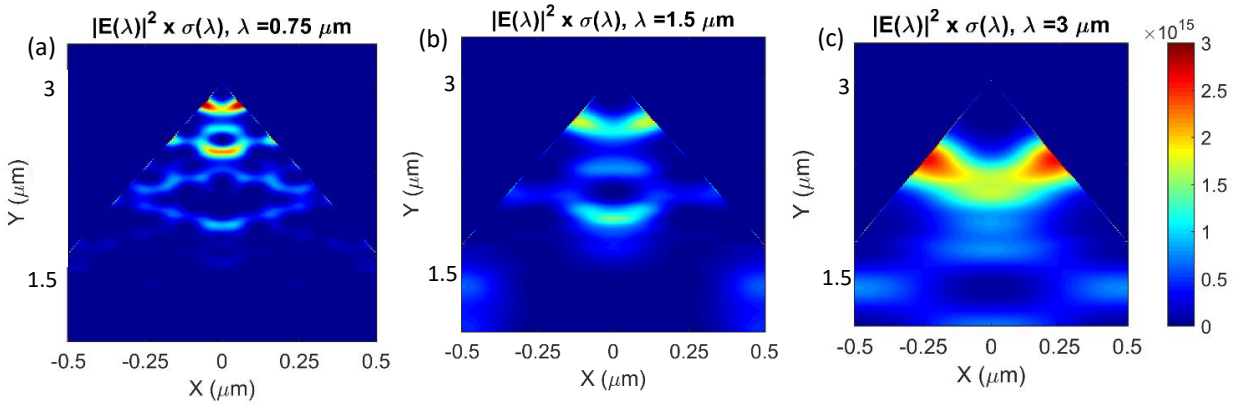

Fig. 4.11. a-b-c) $|E(\lambda)|^2$ x $\sigma(\lambda)$ at wavelengths of 0.75, 1.5 and 3 µm for the triangle dimensions of p =1 µm, h =3 µm and carrier concentration of 10^{14} cm^{-3}.

As shown in Fig. 4.11, highest absorption inside the triangle occurs at the region where side mode with highest intensity penetrates the structure. Field distribution due to this mode, thus the absorption, inside the triangle is similar for the selected wavelengths. Results depicted in Fig. 4.10 and 4.11 shows that these textures support resonance modes at different

wavelengths and resonance conditions are satisfied throughout the geometry multiple times. To analyze, previously reported study regarding to resonance mechanisms in a trapezoid geometry is considered.

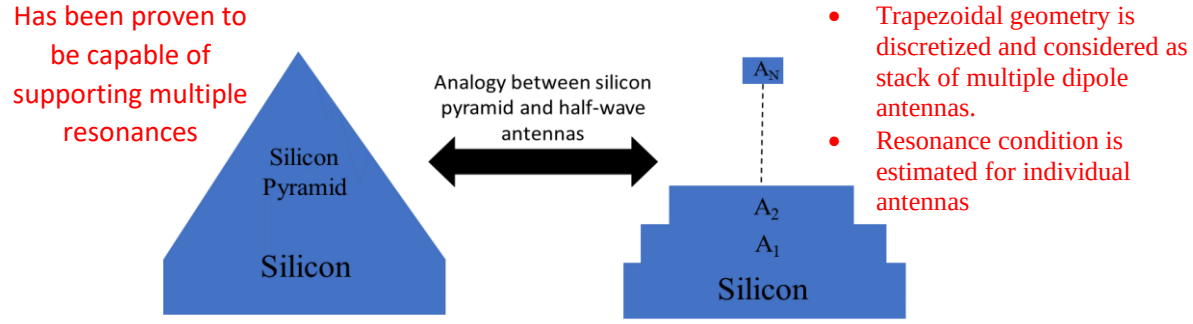

Fig. 4.12. Scheme for analogy between silicon triangle and stacked half-wave antennas

In the literature, such position dependent local field enhancements are reported for trapezoidal metal-insulator-metal (MIM) ultra-thin broadband resonators [209]. In [209], it is shown that strong and broadband field enhancement is achieved by exciting multiple resonance modes in different regions of the trapezoidal structure. Similarly, silicon triangle can support multiple resonance modes due to its trapezoidal geometry and give rise to high field enhancements inside which are absorbed due to the broadband loss introduced in the silicon with doping. Those resonance modes also give rise to strong fields in the silicon air interface on the sides of the triangle. Resonance condition for different wavelengths is dependent on -Z direction. Position of the resonance mode with the highest intensity shifts towards to the bottom of the triangle for increasing wavelength. It indicates that higher width is required to achieve increased coupling with the structure for longer wavelengths. It is also observed that those modes are repeated throughout the triangle in -Z direction. To estimate the resonance condition in the triangle, an effective wavelength method derived for optical antennas is used here.

It is known that coupling condition for RF and microwave antennas are strongly correlated with the length of the antenna, e.g. it is $L = (1/2)\lambda$ [210] for half-wave antennas. Such relationship fails in optical frequencies due to the penetration of the incident wave into the structure and interaction of it with the electron oscillations, whereas structures are nearly perfect conductors in microwave and RF applications, thus penetration does not occur. By considering this difference, an effective wavelength, λ_{eff}, calculation formula is derived in [201] which yields an λ_{eff} inside the antenna that can be used to tune the L. By utilizing this theory, required width for the resonance at a specific wavelength inside the silicon triangle is estimated. To apply such analysis, triangular geometry is treated as a combination of several half-wave

antennas which resonate at different wavelengths. Scheme for such representation is depicted in Fig 4.12.

λ_{eff} calculation is described in detail in [201] and final formula for λ_{eff} is given in Eq. (4.9),

$$\lambda_{Eff} = \frac{\lambda}{\sqrt{\varepsilon_s}} \sqrt{\frac{4\pi^2 \varepsilon_s (R^2/\lambda^2)\tilde{z}(\lambda)^2}{1+4\pi^2 \varepsilon_s (R^2/\lambda^2)\tilde{z}(\lambda)^2}} \tag{4.9}$$

where λ is the incident wavelength, ε_s is the permittivity of the incident medium, R is the thickness of the antenna and $\tilde{z}$ is an intermediate variable expressed in [201]. Based on this formula, L for the resonance to occur is obtained as $\lambda_{eff}/2$ for a half-wave antenna. To create an analogy between half-wave antennas and silicon triangles, L is treated as width of the triangle where a side mode occurs. Therefore, side modes are attributed to half-wave antennas and when stacked together in trapezoidal fashion, multiple resonance modes at different wavelengths are supported.

Effective wavelength calculation with Eq. (4.9) is carried out for the selected wavelengths, $\lambda_1 = 0.5$ µm, $\lambda_2 = 1.5$ µm and $\lambda_3 = 3$ µm. Hypothetical half-wave antenna with dimensions is schematized on the triangle and field distribution at λ_3 is shown in Fig. 4.13(a). In this case, effective wavelength of 0.7 µm is obtained, with R =0.13 µm, from Eq. (4.9), thus L = 0.35 µm, which is equal to the width of the triangle at the location where resonance mode is occurred as shown in Fig. 4.10(c). Smaller effective wavelengths are achieved for wavelengths of λ_1 and λ_2, for which field distributions are also shown in Fig. 4.10. To analyze the dependency of L on R, L values are calculated for varying R values. To satisfy the $R << \lambda$ requirement given in [181] for Eq. (4.9) to be valid, R values between $\lambda/20$ and $\lambda/50$ are considered and maximum errors are demonstrated in Fig. 4.13(b) for wavelengths of λ_1, λ_2 and λ_3.

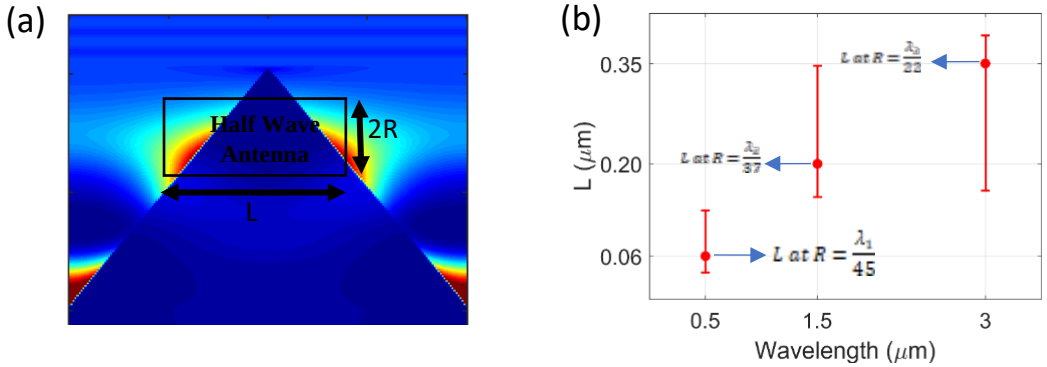

Fig. 4.13. a) Representation of individual half-wave antenna with thickness $2R$ and length L, on the triangle silicon. b) Calculated resonance condition for varying R values and corresponding L values. Lower and upper bounds of the error bars stand for $R = \lambda/50$ and $\lambda/20$. $L = \lambda_{Eff}/2$ values are obtained at $R = \lambda_1/45$, $R = \lambda_2/37$ and $R = \lambda_3/22$ which is equal to the width of the triangle where first side mode occurs.

As seen from Fig. 4.13(b), maximum errors are 0.07, 0.15 and 0.18 μm which corresponds to $\lambda_1/7$, $\lambda_2/10$ and $\lambda_3/15$ for wavelengths of λ_1, λ_2 and λ_3. Estimation accuracy is increased with higher *'R'* at longer wavelengths which indicates that fields are less confined in the geometry for longer wavelengths. Such variations in confinement also shown in Fig. 4.10. Calculated effective wavelengths for the given dimensions of *'L'* and *'R'* shows that absorption occurs in very small dimensions compared to overall size. This also explains the high absorption at different periodicities which controls the width of the triangles. Since sufficient width for effective wavelength matching condition is satisfied for p =1, 2 and 4 μm, high fields, thus absorption, inside the triangles are achieved. As shown in the field distribution results, these absorptance modes are repeated throughout the geometry. This repetition is attributed to similar resonance condition, which occurs due to the scaling of effective wavelength obtained from Eq. (4.9). In other words, effective wavelength matching conditions are satisfied when the width of the triangle is extended. As a next step, effects of periodicity of the triangles, therefore the texture widths, on the field distributions and absorption are investigated.

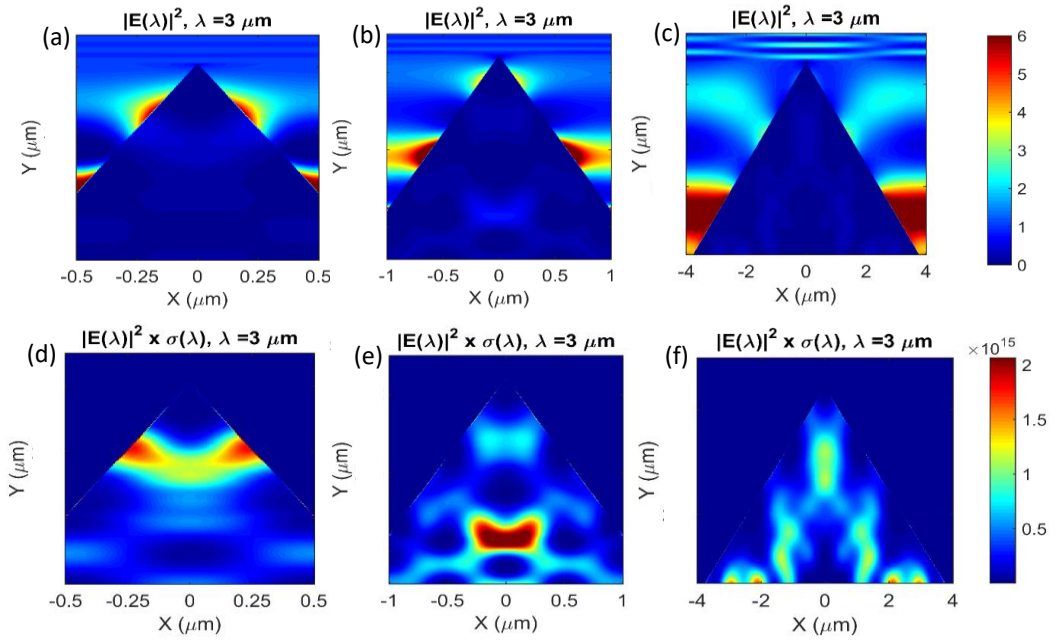

Fig. 4.14. a-b-c) $|E(\lambda)|^2$ distributions at λ =3 μm wavelength for p =1 μm, 2 μm and 4 μm respectively. d-e-f) $|E(\lambda)|^2$ x σ(λ) distributions at λ =3 μm wavelength for p =1 μm, 2 μm and 4 μm respectively.

$|E(\lambda)|^2$ distributions depicted in Fig. 4.14(a), (b) and (c) shows that number of side modes at 3 μm is increased with increasing periodicity. These results indicate that coupling condition inside the triangle is repeated and it is linked to the periodicity, thus the width of the triangle. However, different trends are observed in the fields inside the triangle. In Fig. 4.14(d), a single distinctive high absorption zone is observed inside the triangle which is linked to side mode shown in Fig. 4.14(a). The highest absorptance zone is shifted towards to the bottom of

the triangle and exhibits a different kind of $|E(\lambda)|^2 \, x \, \sigma(\lambda)$ distribution when p is increased to 2 μm.

The highest absorptance zone in Fig. 4.14(d) is occurred due to the side modes and a continuous trend between the fields inside and outside of the triangle is observed. However, a continuous trend is not observed between the highest $|E(\lambda)|^2 \, x \, \sigma(\lambda)$ region inside the triangle and side modes shown in Fig. 4.14(e) and 4.14(b) respectively.

A different behavior from these is observed when p =4 μm. As seen in Fig. 4.14(f), multiple high $|E(\lambda)|^2 \, x \, \sigma(\lambda)$ zones are occurred, and they are extended in -Z direction like propagating modes. $|E(\lambda)|^2 \, x \, \sigma(\lambda)$ in Fig. 4.14(e) and 4.14(f) indicates that absorptance enhancement inside the triangles in these geometries does not only stem from effective wavelength matching condition. Although resonance conditions in the triangle is satisfied as shown in Fig. 4.14(b) and 4.14(c), another phenomenon occurs in these geometries which induces fields that interfere with the resonances. Therefore, distinctive $|E(\lambda)|^2 \, x \, \sigma(\lambda)$ region in Fig. 4.14(e) is attributed to the interference of the fields induced by multiple electromagnetic phenomenas occurring in the geometry. Finally, results depicted in Fig. 4.14(f) shows that field enhancement in the geometry is dominated by this second electromagnetic phenomenon which give rise to field enhancements extended in -Z direction and suppresses the fields induced by effective wavelength matching.

It is observed that these triangles resemble the waveguide geometries that are composed of a high index core surrounded by a low index cladding which supports certain TM modes. In this configuration, silicon acts as high index core and air is the low index cladding material as depicted in Fig. 4.15(a). Due to the tapered geometry, broadband spectrum of wavelengths is supported throughout the geometry and response is analogous to tapered fibers [211]. In tapered fibers, modes with longer wavelengths start to cut-off as the width of the fiber shrinks. In the textured silicon geometries, modes with longer wavelengths start to occur as width of the triangle increases.

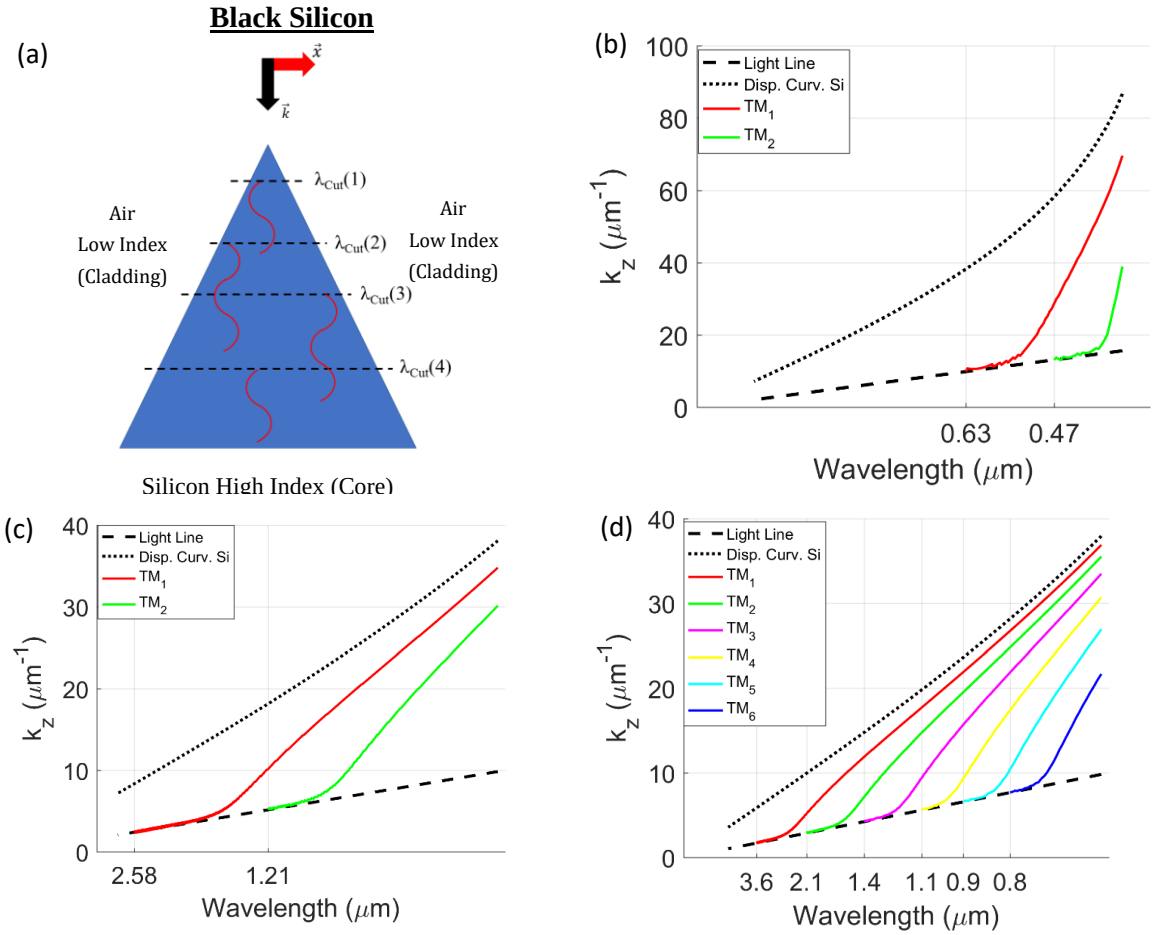

Fig. 4.15. a) Scheme for the black silicon as a waveguide problem composed of high index (core) and low index (cladding). b-c-d) Dispersion diagrams for d =0.06, 0.2 and 0.35 μm at which effective wavelength matching condition is satisfied for wavelengths of 0.5, 1.5 and 3 μm wavelengths.

Therefore, two problems are analogous and similar analysis is adapted based on the reciprocity of the Maxwell's equations. Assuming tapered geometry is composed of rectangular segments for which supported TM modes' cut-off wavelengths are estimated by,

$$k_{cut} = \frac{m\pi}{d\sqrt{1-\frac{\mu_1\varepsilon_1}{\mu_0\varepsilon_0}}} \tag{4.10}$$

and dispersion diagrams are obtained by the following expressions:

$$\left\{\begin{matrix}\tan\left(k_x d\right)\\ -\cot\left(k_x d\right)\end{matrix}\right\} = \sqrt{\frac{w^2\mu_0\left(\varepsilon_1-\varepsilon_0\right)d^2}{\left(k_x d\right)^2}-1} \tag{4.11}$$

$$k_z = \sqrt{w^2\mu_0\varepsilon_1 - k_x^2} \tag{4.12}$$

With the aid of dispersion diagrams, which modes are supported at certain parts of the tapered geometry is estimated. Based on these formulas, dispersion diagrams for different core widths, which corresponds to width of the silicon triangle. Diagrams for *d=0.06* μm, *d=0.2* μm and *d=0.35* μm, at which effective wavelength matching is achieved, are obtained and shown in Fig. 4.16.

As seen in Fig. 4.16(a), 4.16(b) and 4.16(c) respectively, only TM_1 modes exist with a very small wavevector (near cut-off wavelength), for wavelengths of 0.5 μm, 1.5 μm and 3 μm when *d* is set to 0.06 μm, 0.2 μm and 0.35 μm. This indicates that fields formed due to the effective wavelength matching in these segments do not strongly interfere with TM modes. Therefore, *E* fields smoothly travels throughout the triangle in -X direction and continuous trends are observed. However, this is only valid for the top side mode.

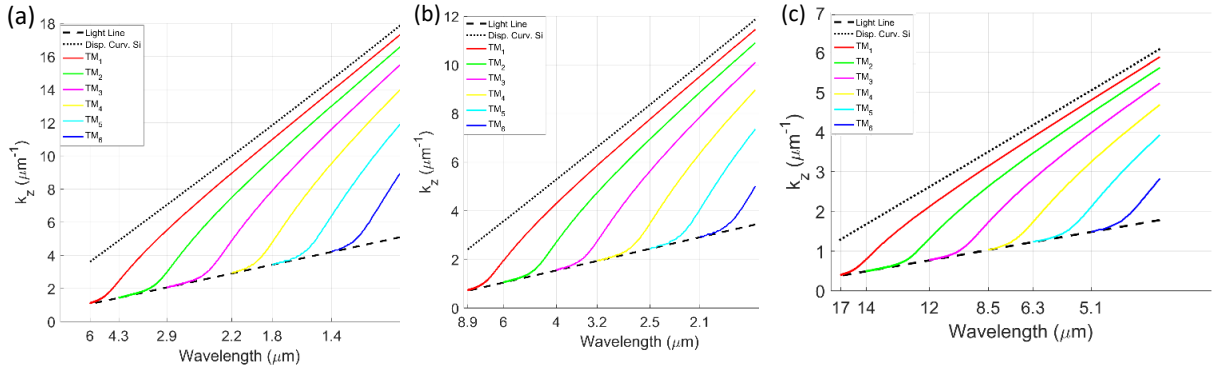

Fig. 4.16. a-b-c) Dispersion diagrams for d =0.7, 1 and 2 μm and supported *TM* modes with cut-off wavelengths labeled.

Although modes that exist when *d =0.2* μm or *d=0.35* μm do not have high wavevectors at longer wavelengths, it is not the case for shorter wavelengths. As seen in Fig. 4.15(c) and 4.15(d), number of modes and magnitude of the existing modes' wavevectors are increased at shorter wavelengths. This indicates that TM modes at shorter wavelengths start to interfere with fields induced by effective wavelength matching when width is around 0.2 μm. Such interference lead to reduction in absorption in the visible spectrum for the rough surfaces with increased correlation lengths and shown in Fig. 4.9(a). Since width of the individual spikes are increased with increasing correlation lengths, TM modes start to form in the textures and reduction in absorption in shorter wavelengths are observed. To further analyze the effect of texture width, *d*, modes in the structures with higher periodicities are analyzed.

As periodicity increased, maximum width of the silicon triangle is also increased, and multiple effective wavelength matching conditions occur throughout the geometry as shown in Fig. 4.14(b). Increase in maximum possible width also allows the triangle support other TM

modes which have longer cut-off wavelengths. To show this, dispersion diagrams with *d = 0.7* μm, *1* μm and 2 μm is demonstrated in Fig. 4.16. As shown in Fig. 16, with increasing *d*, number of TM modes increase and wavevector of the existing modes, e.g. TM_1, is increased. Therefore, at wider widths, contributions from TM modes to electric fields are increased. This leads to significant changes in field distributions and reduction in absorption which becomes more dominant at shorter wavelengths. In summary, our analysis regarding to supported TM modes reveal that these modes have significant effect on the field distribution inside the triangle. It is shown that TM modes becomes dominant in broadband with increased periodicity of the triangles and compensates the effect fields induced due to the effective wavelength matching throughout the geometry. In other words, TM modes starts to dominate field profile in the geometry at widths around 0.3 μm in broadband and effective wavelength matching is dominant at smaller widths.

5. BROADBAND HIGH TEMPERATURE THERMAL EMITTER/ABSORBER DESIGNED BY ADJOINT METHOD

Dispersive characteristics and sign change in the dielectric function of ZrB_2 [179], from positive to negative, allows exciting different phenomena including ENZ/ENP and plasmonic modes. In this study, broadband thermal emitters/absorbers in 0.3-3 μm spectrum composed of ZrB_2 designed by adjoint based topology optimization are demonstrated. First, emission/absorption of periodically arranged rectangular gratings are evaluated and considered as initial intuitive designs. Initial structures exhibit nearly 65 % emission/absorption in 0.3-3 μm spectrum with distinct peaks around 0.7 and 1 μm for which underlying mechanisms are analyzed. Variations in interested spectrum with changing geometrical dimensions are also reported. Next, initial designs are fed to adjoint based inverse design algorithm and topology optimization is conducted in 3D to increase emission/absorption in broadband spectrum. Resulting structures yield elevated emission by 20-25 % in broadband spectrum, which cannot be achieved by a simpler topology. Our results show that textured ZrB_2 surface exhibits high emission in broadband spectra, comparable to the ones obtained by mixing and doping, which can be utilized as high temperature broadband thermal emitters.

5.1 Methodology

Reflection (R) and transmission (T) of the rectangular gratings on bulk ZrB_2 are calculated and absorption (A) is obtained from the equality $1 = A + R + T$ using FDTD [200]. In the simulations, optical properties retrieved from [179] are used. Periodic on x-y dimensions and PML boundary conditions are applied in -z direction. Structures are excited with a linearly polarized plane wave propagating in -z direction. Geometrical dimensions and physics of the simulations are depicted in Fig. 5.1(b).

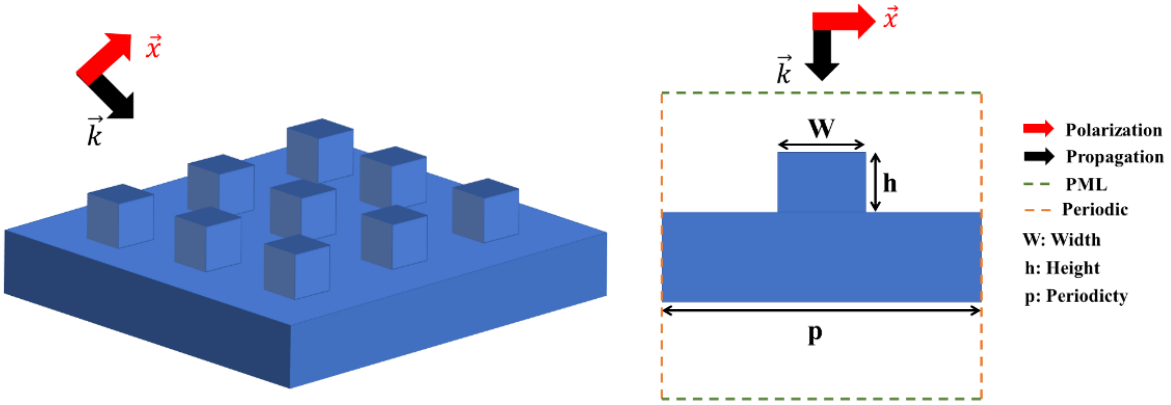

Fig. 5.1. a) 3D visualization of rectangular gratings. b) 2D scheme of geometrical dimensions and simulation physics.

The required gradient of the figure of merit, FoM, with respect to permittivity change is calculated in a similar fashion described in [212]. In [212], gradient is calculated for electric field enhancement and mode matching problems, which can be adapted to reflection minimization, therefore emission/absorption enhancement problem, in which FoM is given as,

$$FoM = \frac{\frac{1}{2}\int \mathrm{Re}\left(\vec{E}(\lambda) x \overrightarrow{H}(\lambda)^{*}\right) ds}{I(\lambda)} \tag{5.1}$$

where $\vec{E}(\lambda)$ and $\vec{H}(\lambda)$ are electric and magnetic fields and $I(\lambda)$ is the source intensity. In Eq. (5.1), $\vec{E}(\lambda)x\vec{H}^{*}(\lambda)$ can be denoted as $\vec{P}(\lambda)$, poynting vector. Gradient of the FoM with respect to change in permittivity on the design space in terms of Poynting vectors from forward and adjoint simulations is given as,

$$\frac{\partial FoM}{\partial \varepsilon(x)} = \mathrm{Re}\left[\vec{P}^{Forw}(x)\cdot\vec{P}^{Adj}(x)\right] \tag{5.2}$$

where $\vec{P}^{Forw}(x)$ and $\vec{P}^{Adj}(x)$ are poynting vectors on the design space, obtained from forward and backward simulations. $\vec{P}^{Forw}(x)$ is obtained from the simulation in which design space is excited with a plane wave in this case.

$\vec{P}^{Adj}(x)$ is needed to estimate how small geometrical perturbations change the $\vec{P}^{Forw}(x)$, therefore, *FoM*. By using Maxwell Green's function and its reciprocity, for electric,

$$\overline{\overline{G^{EP}}}(x,x') = \overline{\overline{G^{EP}}}(x',x)^{T} \tag{5.3}$$

and for magnetic,

$$\overline{\overline{G^{EM}}}(x,x') = \overline{\overline{G^{EM}}}(x,x')^{T} \tag{5.4}$$

dipoles, electric and magnetic fields on the measurement plane, *x'*, induced by dipoles at a point on design space, *x*. Since every small geometrical perturbation on the design space acts as a dipole scatterer, Maxwell Green's functions are used to calculate the electric and magnetic fields induced by those scatterers on the measurement plane, *x'*. By relying on the reciprocity of these functions, shown in Eq. (5.3) and (5.4), dipole scatterers are transferred to *x'* and fields induced by them on x are used to calculate $\vec{P}^{Adj}(x)$. Mathematical expression for $\vec{P}^{Adj}(x)$ is given as,

$$\vec{P}^{Adj}(x) = \varepsilon_0 \Delta V \frac{\int \vec{E}^{Forw} x \vec{H}^{Forw} ds}{I(\lambda)} \int \left(\overline{\overline{G^{EP}}}(x,x')\vec{n} - \overline{\overline{G^{EM}}}(x,x')\frac{\vec{n}}{\mu_0} \right) ds \tag{5.5}$$

These calculations are realized in FDTD [180] with the dipole sources placed on the measurement plane and $\vec{P}^{Adj}(x)$ is obtained. Details of the calculation of the dipole magnitudes and phases are described in [213] which were used in the implementation. Once $\vec{P}^{Adj}(x)$ is obtained, gradient is calculated as given in Eq. (5.5). Visual for the formation of the forward and adjoint simulations is depicted in Fig. 2. With the knowledge of the gradient, geometrical changes are introduced in the design space with fixed volume of ΔV in an iterative fashion. Due to the broadband nature of the problem, both forward and adjoint simulations are conducted in broadband spectrum and wavelength with highest reflection is selected and only gradient with

respect to that wavelength is calculated in every iteration. Then geometry is modified in the gradient direction to reduce the reflection and increase the absorption.

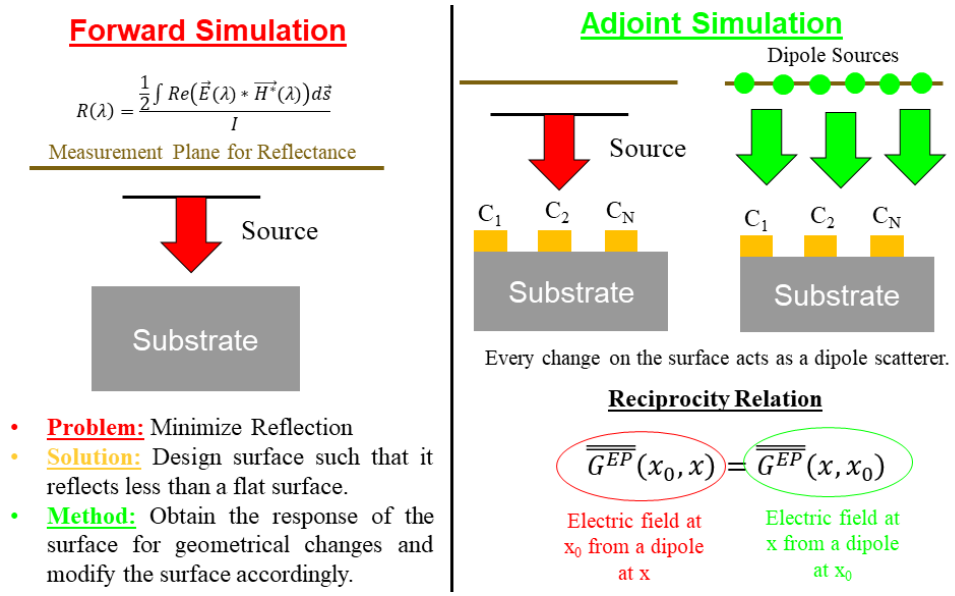

Fig. 5.2. Visuals for the forward and adjoint simulations.

Design space for the algorithm is depicted in Fig. 5.3. Inverse design technique is applied to two type structures with dimensions given in Table 5.1. Design space is determined as the non-pillar region, surface of the bulk ZrB_2. Filling factor, *FF*, is defined as the ratio of the area with and without ZrB_2 where A_P is the area of the pillar, $A_{DS}(1)$ is the total area of the design space with ZrB_2 added and $A_{DS}(0)$ is the untouched ZrB_2 surface on the design space. *FF* of the initial designs are 25 % which means that pillar occupies 25 % of the surface of the bulk ZrB_2. Emission/absorption spectra of both type of structures are obtained for *FF* of 40 % and 50 %. Parametric sweep also conducted for the structure type I.

Table 5.1. Geometrical dimensions and filling factors of the studied structures

	Pillar Dimensions	**Periodicity**	**Filling Factor**
Type I	W = L = h = 0.5 μm	P = 1 μm	FF =25 %
Type II	W = L = h = 1 μm	P = 2 μm	FF =25 %

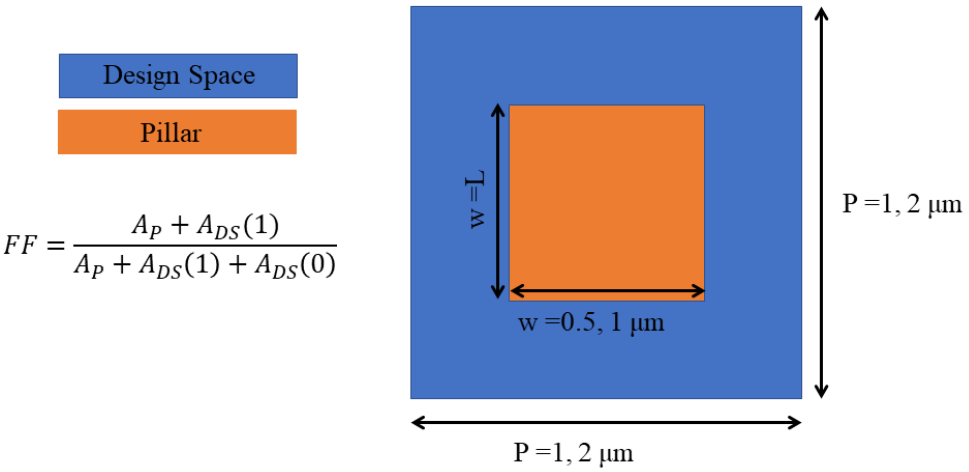

Fig. 5.3. Design space and geometrical dimensions of the initial structures

5.2.Results and Discussions

In this section, emission/absorption spectra of the structures are demonstrated and analyzed. In the first subsection, results belong to rectangular gratings on top of bulk ZrB_2 substrate, intuitive/initial structures obtained by parametric sweep, are demonstrated. Resulting spectra is analyzed and resonance mechanisms responsible from distinct peaks are reported. In the second subsection, emission/absorption spectra of the structures designed by inverse design by adjoint method are demonstrated and discussed. Calculation of the gradient based on adjoints are also briefly summarized in that subsection.

5.2.1 Intuitive Structures

Emission/absorption spectra for varying grating dimensions, *w* and *h*, as well as periodicity is demonstrated and resulting spectra are analyzed. In Fig. 5.4(a), emission/absorption spectra for varying widths for fixed h = 0.5 μm and p = 1 μm. Effect of h on emission/absorption for fixed w =0.5 μm and p = 1 μm are also depicted in Fig. 5.4(b).

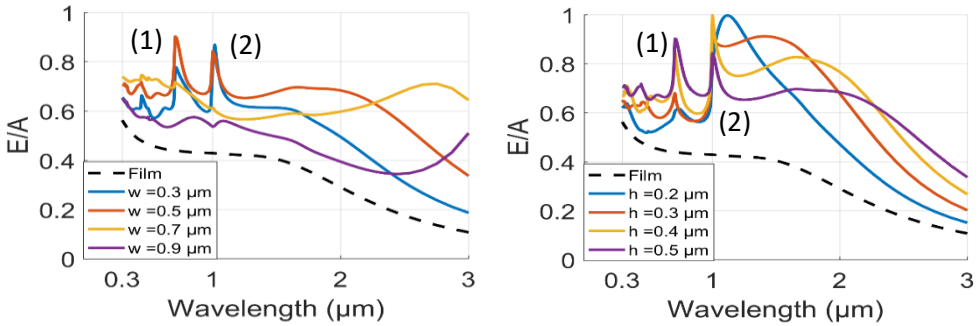

Fig. 5.4. a) ε(λ)/α(λ) intensities for h =0.5 μm and p =1 μm and varying widths. b) ε(λ)/α(λ) intensities for w =0.5 μm and p = 1 μm.

As seen from Fig. 5.4(a) when grating/pillar widths are at 0.3 and 0.5 μm distinct peaks around 0.7 and 1 μm wavelengths are observed with intensities reaching up to 90 % levels. Emission/absorption intensity almost approach the intensity of the film form except the increase around 3 μm. This is attributed to increased volume fraction when width is set to 0.9 μm at which waves with smaller lengths "sees" almost a flat film. Sharp peaks observed in *w* =0.3 and *w* = 0.5 μm are not exist in higher widths. Variations in *h*, for which emission/absorption is depicted in Fig. 5.4(b), does not significantly change the intensities or trends at longer wavelengths. Also, both peaks around 0.7 and 1 μm wavelengths occur at different *h*. Bandwidth of the sharp peak around 0.7 μm remained similar but only its intensity is increased with increasing *h*. On the other hand, changes in *h* caused variations in the bandwidth of the peak around 1 μm.

To explain the underlying mechanisms of the peak 1 and 2 around 0.7 and 1 μm, which are also labeled in Fig. 5.4, different methods are adapted. Cavity modes are calculated to analyze the peak 1, due to the resemblance of the geometry with metallic waveguides. Effective medium calculation for meta-materials [214] and momentum matching condition for wavevectors to estimate plasmonic contributions, are used to analyze the peak 2, since no cavity modes are available around those wavelengths with studied dimensions.

Contribution of *TM* modes is held responsible for selective emission obtained by semi-open cylindrical cavities surrounded by W, by relying on the high optical conductivity of W at wavelengths of interest [87]. Comparison of optical conductivities of W and ZrB_2, formation of semi-open cavities and cut-off wavelengths of TM modes obtained by,

$$\frac{1}{\lambda_C} = \frac{1}{2\pi}\sqrt{m\left(\frac{\pi}{w_C}\right)^2 + n\left(\frac{\pi}{l_C}\right)^2 + k\left(\frac{\pi}{h_C}\right)^2} \tag{5.6}$$

are demonstrated in Fig. 5.5.

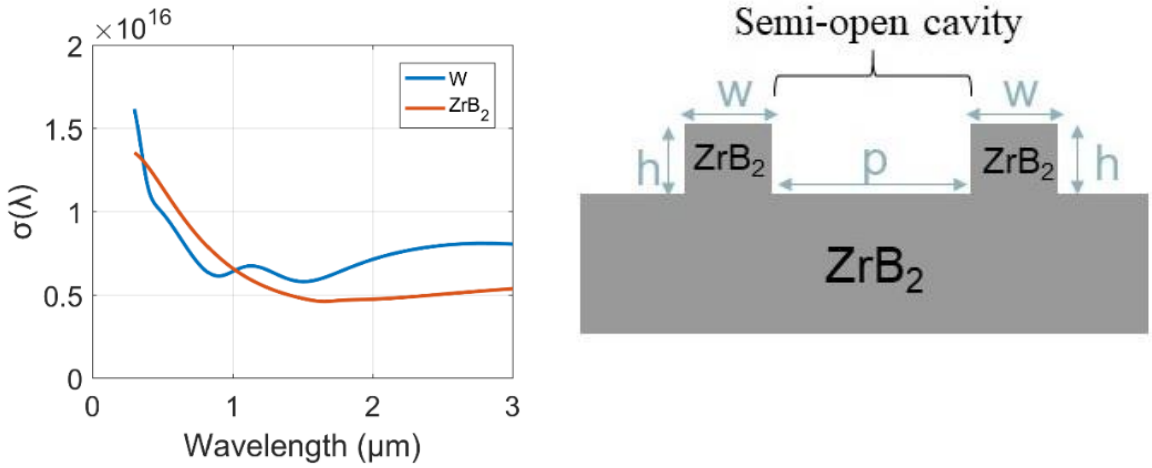

Fig. 5.5. a) σ(λ) of W and ZrB_2. b) Scheme for semi-open cavity formation

As seen from Fig. 5.5(a), σ(λ) of W and ZrB_2 are similar. As shown in Fig. 5.5(b), cavity size is controlled by *w* of the pillars for fixed *p*. In Eq. (5.6) where *m*, *n*, *k* and constants from 1 to infinity and w_C, l_C and h_C are the geometrical dimensions of the cavity. Cut-off wavelengths, λ_C for *TM* modes in a cavity is estimated by Eq. (5.6) and dominant *TM* modes are shown in Table 5.2.

Table 5.2. λ_C for various TM_{mnk} modes for different pillar dimensions

Pillar Dimensions	**TM_{110}**	**TM_{111}**	**TM_{112}**	**TM_{113}**
(W =0.3, L =0.3, h =0.5)	0.98 μm	0.88 μm	0.70 μm	0.552 μm
(W =0.5, L =0.5, h =0.5)	0.70 μm	0.66 μm	0.57 μm	0.48 μm
(W =0.7, L =0.7, h =0.5)	0.42 μm	0.41 μm	0.39 μm	0.35 μm
(W =0.9, L =0.9, h =0.5)	0.14 μm	0.14 μm	0.14 μm	0.13 μm
(W =0.5, L =0.5, h =0.2)	0.70 μm	0.52 μm	0.34 μm	0.24 μm
(W =0.5, L =0.5, h =0.3)	0.70 μm	0.60 μm	0.45 μm	0.34 μm
(W =0.5, L =0.5, h =0.4)	0.70 μm	0.64 μm	0.52 μm	0.42 μm

As shown in Table 5.2, when pillar dimensions are set to (0.5,0.5,0.5) μm, TM_{110} mode has λ_C =0.7 μm which is the dominant mode. Since other modes, e.g. TM_{111}, TM_{112}, TM_{113}, have shorter λ_C, they do not interfere with TM_{110} mode around 0.7 μm. However, when pillar dimensions are set to (0.3,0.3,0.5) μm, λ_C of the dominant TM_{110} mode shifts to 0.98 μm and TM_{110}, TM_{111} and TM_{112} modes start to contribute to absorption around 0.7 μm wavelength. Due to the interference of multiple modes, peak intensity is slightly reduced. When pillar dimensions

are set to (0.7,0.7,0.5) and (0.9,0.9,0.5) μm, λ_C of all TM_{mnk} modes shift toward shorter wavelengths, therefore no distinct peaks are observed around 0.7 μm wavelength. Since only TM_{110} mode is supported for h = 0.2, 0.3 and 0.4 μm for $W=L=0.5$ μm, no destructive interference exists and fields due to TM_{110} mode interact with the surrounding ZrB_2 more. These lead to an increasing absorption intensity with higher h. On the other hand, there exists only one mode, TM_{110} λ_C =0.98 μm, among geometries depicted in Table 5.2, around 1 μm, when h<0.5. Cut-off wavelengths depicted in Table 5.2 indicates that for h<0.5 μm, λ_C <0.7 μm and all *TM* modes shift trough shorter wavelengths than 1 μm, which shows that no contribution to absorption around that wavelength is present from *TM* modes. This indicates that peak 2, does not stem from absorption of fields induced in cavity due to waveguide modes by multiple reflection from highly conductive surrounding material.

To explain the origins of the peak 2, whose wavelength shifts to nearly 1.8 μm with varying h, plasmonic modes and effective permittivity, $\varepsilon_{Eff}(\lambda)$, are estimated. Plasmonic modes are considered in the analysis, because $\varepsilon_{ZrB2}(\lambda)$<0 for λ>1.5 μm, which is necessary condition for plasmonic resonances. Resonance wavelengths of the plasmonic modes are calculated by momentum matching condition,

$$\left(\frac{2\pi m}{P}\right)=\sqrt{\frac{\varepsilon_d(\lambda)\varepsilon_m(\lambda)}{\varepsilon_d(\lambda)+\varepsilon_m(\lambda)}}k_0(\lambda) \tag{5.7}$$

where P is the periodicity, $\varepsilon_d(\lambda)$ and $\varepsilon_m(\lambda)$ are the permittivity of the filling and grating material respectively and m is the resonance order. Plasmonic resonance wavelengths for varying P is calculated and shown in Fig. 5.6(a). Results show that there exist a plasmonic resonance around 1.6 μm wavelength when P =1 μm and no plasmonic mode exist around 1 μm wavelength for any periodicity since $\varepsilon_{ZrB2}(\lambda=1\ \mu m)$>0 as shown in Fig. 5.6(b). However, no plasmonic resonance around 1.6 μm wavelength is observed in absorption spectra depicted in Fig. 5.4(b) for h =0.2 μm. Therefore, to analyze the peak around 1 μm wavelength and disappearance of plasmonic resonance effect on the absorption spectra, $\varepsilon_{Eff}(\lambda)$ values are calculated for varying h in broadband spectrum and obtained results are depicted in Fig. 5.7.

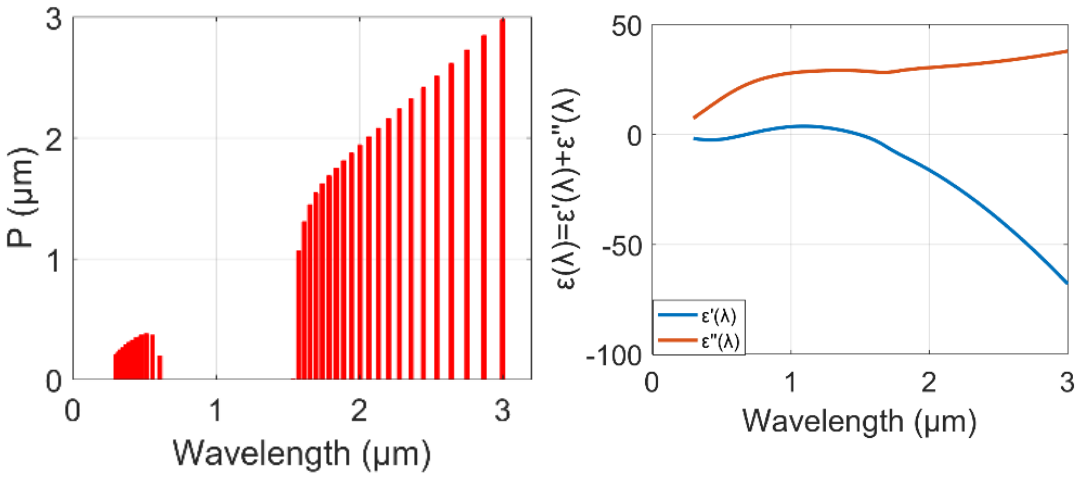

Figure 5.6. a) Required periodicities for allowed plasmonic modes. b) Permittivity of ZrB_2 retrieved from [179].

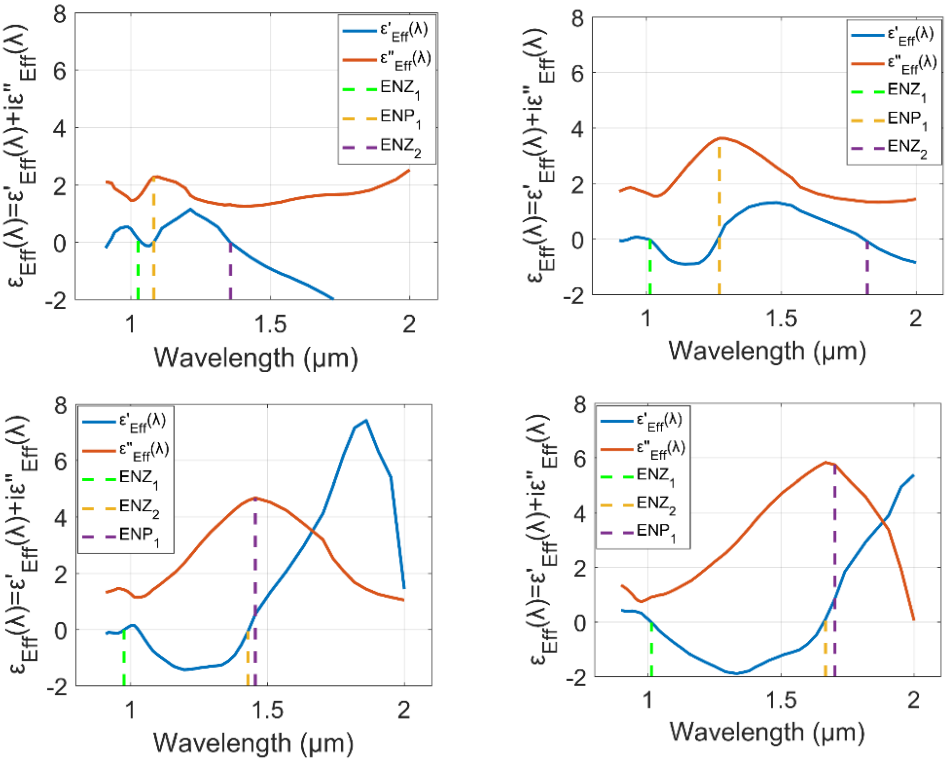

Figure 5.7. a-b-c-d) $\varepsilon_{Eff}(\lambda)$ values calculated by [194] in broadband for h =0.2, 0.3, 0.4 and 0.5 μm.

Fig. 5.6(a) shows that when p =1 μm, a plasmonic resonance around 1.55 μm is excited. In addition, $\varepsilon_{Eff}(\lambda)$ values depicted in Fig. 5.7(a)-(d) show that ENZ and ENP resonances also occur over the spectra, including 1.55 μm wavelength. In [57], it is shown that ENZ resonances give rise to strong absorption while $\varepsilon'(\lambda) \approx 0$ and $\varepsilon''(\lambda) \neq 0$ due the reduced impedance mismatch at the interface. In addition, ENP modes are also introduced in [78, 153] where $\varepsilon''(\lambda)$ exhibits a Lorentzian shape and give rise to absorption over the spectra whose bandwidth is

strongly dependent on the Lorentz peak in ε''(λ). Their contribution to absorption spectra were also discussed in [78, 153]. When h = 0.2 μm, an ENZ and ENP resonance around 1 μm wavelength is observed in Fig. 5.7(a) which result in absorption peak with relatively higher bandwidth, shown in Fig. 5.4(b). The ENZ_2 resonance in this case occur around 1.4 μm and interfere with the fields induced by plasmon mode around 1.55 μm and cancel out their effects. With increasing h, Lorentzian peaks shift toward longer wavelengths which reduces the interference with the ENZ modes around 1 μm wavelength. Therefore, sharp peaks at 1 μm wavelength occur when h = 0.3, 0.4 and 0.5 μm. However, as ENP resonance shift toward longer wavelengths, it starts to interfere with plasmonic resonance, thus lower intensities compared to h =0.2 μm case are observed. When h =0.3 μm ENP occur around 1.2 μm, therefore absorption intensity remains around 0.9 in 1-1.6 μm. Finally, ENP resonances shift to 1.6 μm and 1.7 μm wavelengths when h = 0.4 and 0.5 μm respectively, therefore smooth peaks around those wavelengths which exhibit Lorentzian shapes observed in corresponding εEff (λ) figures. Shift of the ENP resonance is also responsible from the higher absorption intensity at longer wavelengths observed in Fig. 5.4(b). These results show that, ENZ, ENP and plasmonic modes contribute to absorption spectra at different wavelengths depending on the geometry. In summary, although a plasmonic resonance around 1.6 μm exist due to the periodicity of the pillars, those pillars create an effective ENZ and ENP mediums, because of their width and lengths.

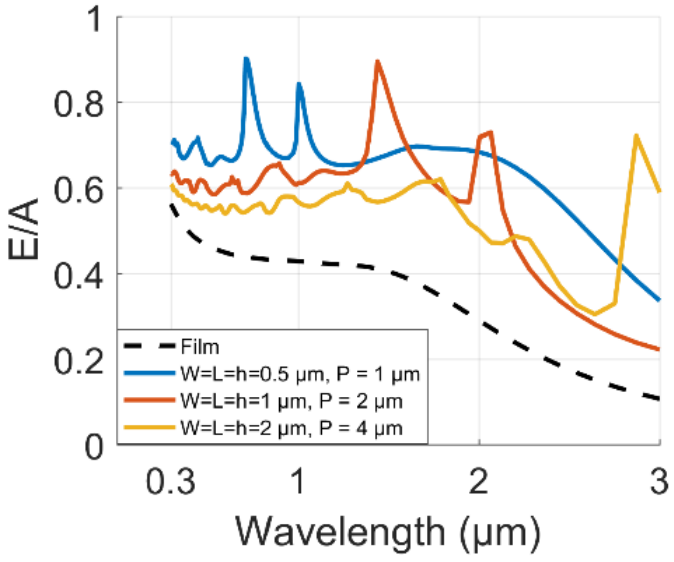

Fig. 5.8. Emission/absorption spectra of the structures with larger dimensions.

To analyze the effect of *P*, emission/absorption spectra of the structures with larger pillar dimensions and periodicity is reported in Fig. 5.8. Results show that with increasing dimensions, distinct peaks observed around 0.7 and 1 μm wavelengths shift toward longer wavelengths. Only a plasmon resonance peak exists around 2.9 μm, when *P* =4 μm. Structures with larger dimensions do not exhibit higher emission/absorption intensity at near-infrared wavelengths and they have slightly reduced emission at shorter wavelengths. Average emission in 0.3-3 μm spectra reaches up to 65 % levels at maximum.

5.2.2 Non-Intuitive Structures

Some of the intuitive structures studied in the previous section is considered as the initial structures in this section. Two type of structures, whose dimensions are depicted in table 1, are fed to inverse design algorithm and corresponding results are given in this section. Top views of the final designs for *FF* of 40 % and 50 % are depicted in Fig. 5.9.

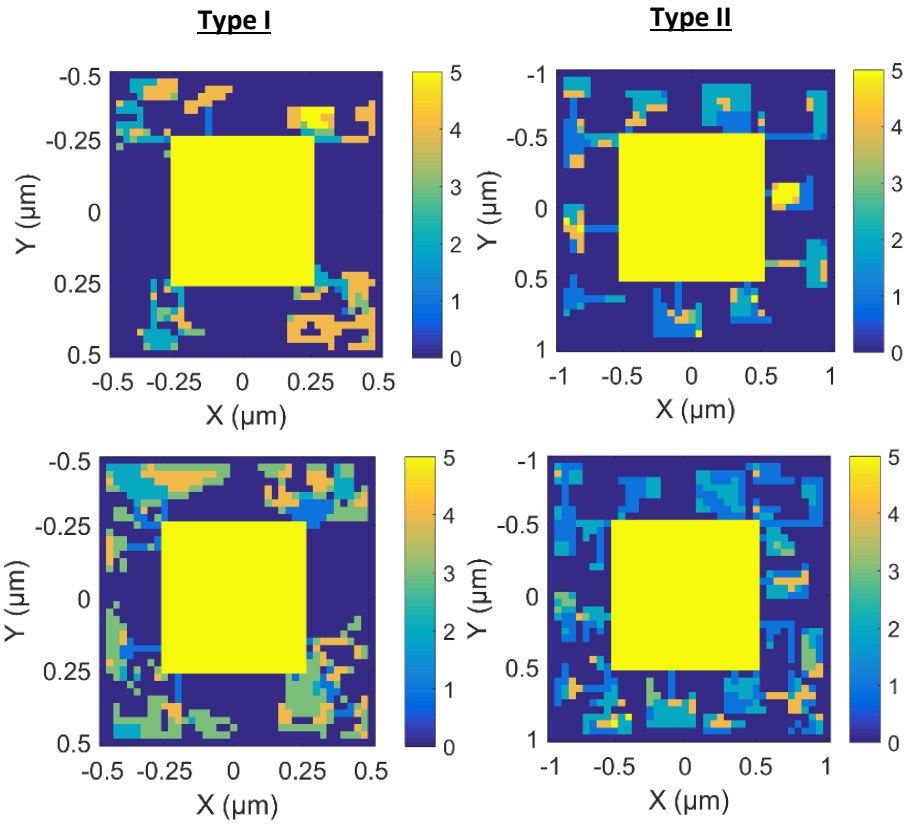

Fig. 5. 9. a-b) Final topology of the structures when maximum FF = 40 %. c-d) Final topology of the structures when maximum FF = 50 %.

Since algorithm adds material to the pixel with highest sensitivity to change, discontinuities in the futures occur as seen in Fig. 5.9. Maximum value of 5 in color scale corresponds to 0.5 and 1 μm in type I and II structures respectively. Average emission/absorption of these structures are demonstrated in Fig. 5.10(a) and 5.10(b) respectively with increasing number of iterations.

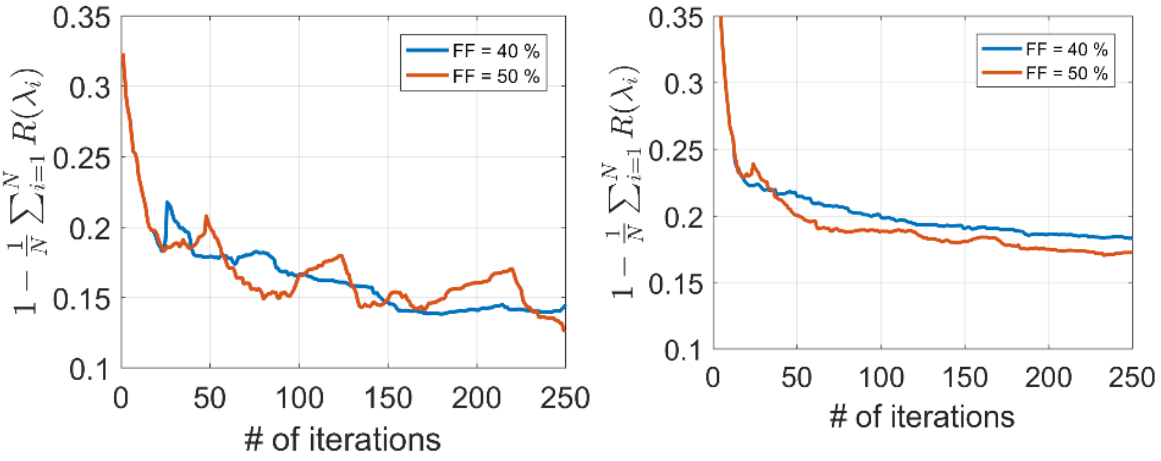

Fig. 5.10. a-b) Average emission/absorption of the structures type I and II with increasing number of iterations of inverse design algorithm

As seen in Fig. 5.10, average emission values converged to 0.14 and 0.18 levels respectively for type I and II structures for *FF* of 40 % and 50 %. After 250 iterations, final structures with *FF* = 50 % are manually modified to create a more feasible pattern for possible experimental studies. Topology of the modified geometries are depicted in Fig. 5.11(a) and 5.11(b) and emission/absorption spectra of the structures are shown in Fig. 5.11(c) and 5.11(d).

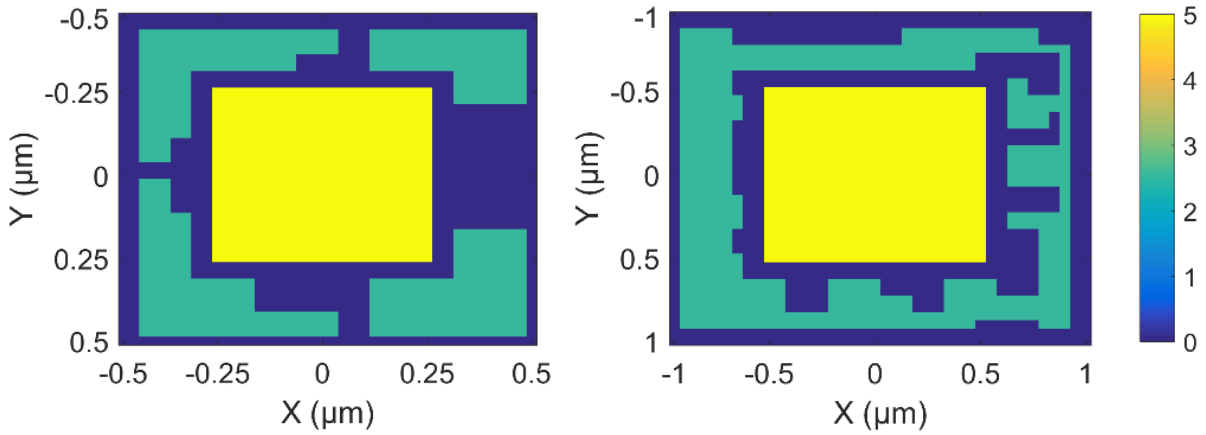

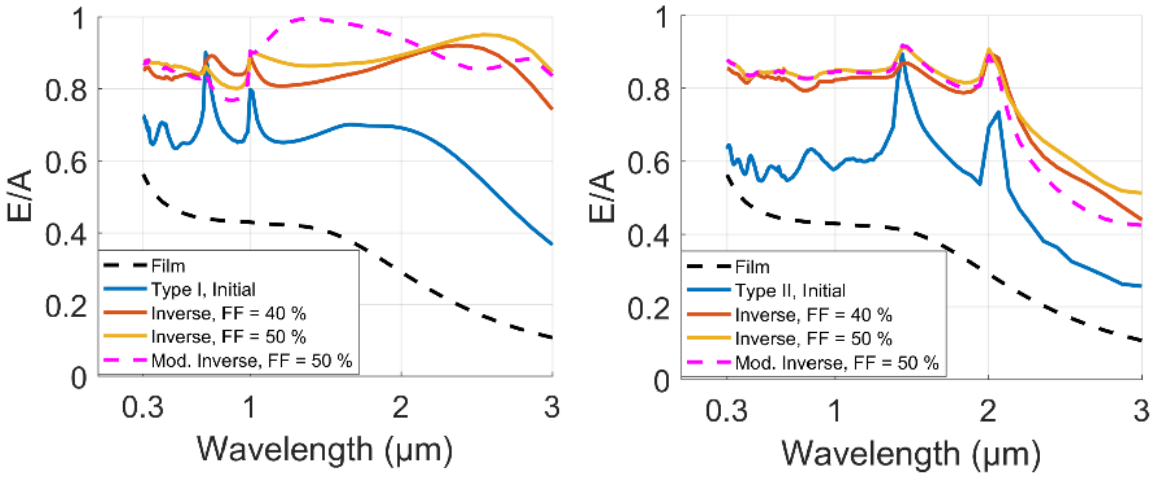

Fig. 5.11. a-b) Modified topology of the type I and II structures with *FF* = 50 %. c-d) Comparison of the emission/absorption of the structures for type I and II respectively.

Spectral results depicted in Fig. 5.11(c) and 5.11(d) shows that introduced changes in the final topologies, which results in topologies depicted in Fig. 5.11(a) and 5.11(b), does not significantly change the absorption/emission in broadband spectrum. As seen in Fig. 5.11(c) and 5.11(d), significant enhancements in emission absorption spectra are achieved with inverse design. Average emission of the film, type I and II structures before and after inverse design are also given in Table 5.3.

Table 5.3. Average emission/absorption values for the structures in film, intuitive and non-intuitive pattern forms

	Film	Intuitive	Non-intuitive/Inverse		Mod. Inverse
			FF =40 %	FF =50 %	
Type I	0.4518	0.6767	0.8438	0.8643	0.8669
Type II		0.5889	0.8170	0.8376	0.8322

Enhancement rates reach up to 40 % levels at longer wavelengths an overall enhancement of 15 % and 20 % respectively for type I and II structures compared to initial designs, which is very challenging to achieve with parametric analysis. Depicted results indicate that *FF* and final modifications in topology does not have significant impact on the broadband behavior.

6. CONCLUSIONS

Main aim of this thesis is the broadband engineering and analysis of spectral characteristics of the surfaces for the selected applications. Different methods are adapted including thickness optimization for thin-films and topology optimization for inhomogeneous/patterned coatings for separate problems. With the used methods and techniques in this thesis, structures with desired broadband, application dependent, spectral behaviors are achieved. All the results depicted in this thesis, contribute to subfields of nanophotonics literature by proposing design and analysis methods which lead to structures with superior characteristics compared to previously reported ones and explain the underlying mechanism that lead to such superior behavior.

Specifically, proposed thin-film optimization strategy for daytime passive radiative cooling yield structures with enhanced cooling power performance compared to previously reported structures designed by traditional optimization methods. Results depicted in this thesis, clearly shows that considering the contribution of spectral characteristics to cooling power results in significant enhancement in cooling power and temperature reduction rates. Cooling power reaching up to 100 W/m^2 at 297 K with 7 layers on Ag is achieved. Temperature reduction rates up to 40 K are reported, when the contributions from conductive and convective heat transfer are prevented. Even in the presence of significant conductive and convective radiative heat loads, temperature reductions 15 K below the ambient are observed. All the spectral results are interpreted by wave impedance analysis, which supports the spectral selectivity. Overall, this new methodology indicates that focusing on maximizing the cooling power of a thin film system yields significant performance improvements compared to the techniques which formulates the problem as purely spectral.

Other than daytime passive radiative cooling, thin-film filters are also proposed as solution to broadband reflectance with refractory metals problem. It is shown that periodic high-low index segments, which are used to improve reflectance around a center wavelength, are

stacked together with different central wavelengths to generate broadband high reflectance. Obtained results indicate that underlying mechanism in the single segment case, creating constructive interference of the reflected beams by equalizing their phases on the front surface, can be extended to the case of several stacked segments with different central wavelengths. Spectral results showed sharp reflectance drops, which stem from interference of approximately half wavelength thick mediums in between different segments. It is shown that this behavior is similar to responses observed in Fabry Perot filters. Influence of design parameters, number of segments and number of layers, were investigated. Findings indicate that central wavelengths of the segments were responsible from the bandwidth of the high reflectance zone and number of layers were highly affecting the magnitude of the reflectance. Finally, we demonstrated that replacing SiO_2 with Al_2O_3 requires higher number of segments to obtain similar reflectance values in broadband spectrum due to deceased ratio of the refractive indices. With the proposed structures, average reflectance of the metals in consideration are increased to 99 % from 40 % levels. Such improvement prevents nearly 1.1 MW /m^2 absorption in aerospace applications operating in orbit of the earth.

Differently from previous problems, in black silicon problem, underlying mechanism of the broadband absorption/emission in existing structures are analyzed, which were not previously studied. In chapter 4, broadband absorption mechanism of the black silicon is investigated. Field distributions inside the random and deterministic textures show that high field intensities which are confined near the edges of the textures occur. Detailed analysis shows that high coupling in transverse direction occurs and coupling conditions are estimated with effective wavelength matching phenomenon in optical antennas. Further analysis reveals that, TM modes are also supported in the textures and affects the absorption distribution over the geometry. Due to the trapezoidal geometry of the textures, TM modes start to form with increasing width (*d*). It is found out that effective wavelength matching occurs in smaller widths ($d<0.3$ μm) and are dominant in terms of contribution to absorption. On the other hand, TM modes start to dominate at higher widths ($d>0.3$ μm) in broadband for which cut-off wavelengths are obtained by waveguide theory. Destructive interference of the fields induced by these two different phenomena lead to slightly reduced spectral absorption. Our findings regarding to driving mechanisms of elevated absorption in black silicon provide a good understanding of those mechanisms which was not discussed in such a detailed manner before.

Finally, emission/absorption of ZrB_2 is improved by studying intuitive and non-intuitive patterns to be used as high temperature broadband thermal emitter/absorber. Rectangular gratings were considered as intuitive patterns and their effect on the emission when patterned on bulk ZrB_2 with varying dimensions are reported. Obtained results showed that gratings form cavities which support certain *TM* modes and resulted in narrowband emission peaks in the spectrum. In addition, it was shown that depending on the grating dimensions and periodicity, *ENZ* and *ENP* modes occur over the spectra as well as plasmonic modes. These phenomena resulted in elevated absorption in relatively narrowband spectrum. Average emission/absorption of 65 % was achieved with intuitive structures, whereas it was around 45 % in film form. As a final step, topology optimization based on adjoints which enables efficient calculation of the gradients, non-intuitive patterns are designed. Resulting non-intuitive patterns lead to significant emission enhancement, especially at longer wavelengths, reaching up to 85 % levels in broadband spectrum which corresponds to nearly 20 % enhancement compared to intuitive designs. Overall, this study demonstrates the potential of ZrB_2 as a broadband thermal emitter/absorber when dispersive nature of its optical properties coupled with an inverse design technique.

In summary, this thesis contributes to nanophotonics literature for applications in energy harvesting, thermal management, broadband thermal emitters and photodiodes. Proposed design methods in this thesis for coatings composed of thin-film filters with selected materials for selective emission/absorption and broadband reflection can be utilized in daytime passive radiative cooling and aerospace applications, respectively. Revealed mechanisms of the broadband absorption/emission in micro/nano-structured black silicon provides a good understanding of the problem and may aid the future design studies in silicon-based photodiodes and photodetectors. Finally, utilizing adjoint based calculation of the gradient in the design of broadband thermal emitters/absorbers, lead to superior designs compared to structures obtained by intuition. In addition to design method perspective, design of the coating by patterning ZrB_2, shows the material's potential as emitter/absorber and demonstration of its available resonance modes shows its applicability in applications require selective behaviors, e.g. sensing. Overall, several problems are studied extensively with clearly outlined methodology and discussed results in detail. Although specific problems which require broadband engineering of the electromagnetic spectrum are discussed, methods depicted in this thesis can be adapted to different problems in the related fields and may inspire future studies.

7. FUTURE WORKS

Based on the research output of this thesis, the following headlines are suggested for further extending the work:

- Proposed reformulation of the passive radiative cooling structure design problem, which focus on cooling power maximization, can be further extended to temperature reduction maximization problem. By coupling the spectral design methods with commercial heat transfer solvers, both spectral and radiative aspects of the problem can be considered and more complicated analysis can be conducted. With such approach, effect of the layer materials and thicknesses on the thermal aspect of the problem due to conduction between layers and convection with the environment, can also be considered.

- Proposed multilayer structures for enhancing the reflection of refractory metals show that very high reflection can be achieved in broadband spectrum. However, it requires high number of layers. To reduce the number of layers, a new design method based on wave impedance analysis (which is already discussed in radiative cooling chapter of this thesis) can be utilized. Structures with less number of layers would be more durable in harsh environmental conditions.

  In addition to multilayers, inhomogeneous type of structures can also be studied to design broadband reflectors, by considering the methods and analysis reported in this thesis.

- Characteristics of black silicon can also be analyzed from the perspective of radiative transfer and near field effects should be studied. Analysis of such characteristics may reveal different opportunities for several energy harvesting applications.

- Utilized adjoint based topology optimization methodology can be adapted to wide range of reflection/absorption/transmission control problems to further enhance the desired spectral performance. It will allow easier exploration of non-intuitive topologies with superior performance.

BIBLIOGRAPHY

[1] S. Y. Lin, J. Fleming, E. Chow, J. Bur, K. Choi, and A. Goldberg, "Enhancement and suppression of thermal emission by a three-dimensional photonic crystal," *Phys. Rev. B - Condens. Matter Mater. Phys.*, vol. 62, no. 4, pp. R2243–R2246, 2000.

[2] J. A. Schuller, T. Taubner, and M. L. Brongersma, "Optical antenna thermal emitters," *Nat. Photonics*, vol. 3, no. 11, pp. 658–661, 2009.

[3] G. C. Prendergast, "Cancer: Why tumours eat tryptophan," *Nature*, vol. 478, no. 7368, pp. 192–194, 2011.

[4] M. A. Kats, R. Blanchard, S. Ramanathan, and F. Capasso, "Thin-Film Interference in Lossy, Ultra-Thin Layers," *Opt. Photonics News*, vol. 25, no. 1, p. 40, 2014.

[5] A. G. Aberle, "Thin-film solar cells," *Thin Solid Films*, vol. 517, no. 17, pp. 4706–4710, 2009.

[6] A. Didari and M. P. Mengüç, "Near- to far-field coherent thermal emission by surfaces coated by nanoparticles and the evaluation of effective medium theory," *Opt. Express*, vol. 23, no. 11, p. A547, 2015.

[7] W. Wang, C. Fu, and W. Tan, "Thermal Radiative Properties of a SiC Grating on a Photonic Crystal," *J. Heat Transfer*, vol. 135, no. 9, p. 091504, 2013.

[8] S. Han and B. J. Lee, "Control of thermal radiative properties using two-dimensional complex gratings," *Int. J. Heat Mass Transf.*, vol. 84, pp. 713–721, 2015.

[9] R. U. Tok and K. Şendur, "Engineering the broadband spectrum of close-packed plasmonic honeycomb array surfaces," *J. Quant. Spectrosc. Radiat. Transf.*, vol. 120, pp. 70–80, 2013.

[10] B. Zhao and Z. M. Zhang, "Study of magnetic polaritons in deep gratings for thermal emission control," *J. Quant. Spectrosc. Radiat. Transf.*, vol. 135, pp. 81–89, 2014.

[11] A. P. Raman, M. A. Anoma, L. Zhu, E. Rephaeli, and S. Fan, "Passive radiative cooling below ambient air temperature under direct sunlight," *Nature*, vol. 515, no. 7528, pp. 540–544, 2014.

[12] E. Rephaeli, A. Raman, and S. Fan, "Ultrabroadband photonic structures to achieve high-performance daytime radiative cooling," *Nano Lett.*, vol. 13, no. 4, pp. 1457–1461, 2013.

[13] B. Guha, C. Otey, C. B. Poitras, S. Fan, and M. Lipson, “Near-field radiative cooling of nanostructures,” *Nano Lett.*, vol. 12, no. 9, pp. 4546–4550, 2012.

[14] L. Zhu, A. Raman, K. X. Wang, M. A. Anoma, and S. Fan, “Radiative cooling of solar cells,” *Optica*, vol. 1, no. 1, p. 32, 2014.

[15] R. Family and M. P. Mengüç, “Analysis of sustainable materials for radiative cooling potential of building surfaces,” *Sustain.*, vol. 10, no. 9, 2018.

[16] M. A. Kecebas, M. P. Menguc, A. Kosar, and K. Sendur, “Passive radiative cooling design with broadband optical thin-film filters,” *J. Quant. Spectrosc. Radiat. Transf.*, vol. 198, 2017.

[17] J. G. Fleming, S. Y. Lin, I. El-Kady, R. Biswas, and K. M. Ho, “All-metallic three-dimensional photonic crytal with a large infrared bandgap,” *Nature*, vol. 417, no. 6884, pp. 52–55, 2002.

[18] X. Zhai, J. Lai, H. Liang, and S. Chen, “Performance analysis of thermophotovoltaic system with an equivalent cut-off blackbody emitter,” *J. Appl. Phys.*, vol. 108, no. 7, 2010.

[19] E. Rephaeli and S. Fan, “Absorber and emitter for solar thermo-photovoltaic systems to achieve efficiency exceeding the Shockley-Queisser limit,” *Opt. Express*, vol. 17, no. 17, p. 15145, 2009.

[20] C. Wu *et al.*, “Metamaterial-based integrated plasmonic absorber/emitter for solar thermo-photovoltaic systems,” *J. Opt.*, vol. 14, no. 2, 2012.

[21] J. R. Howell, M. P. Menguc, and R. Siegel, *Thermal radiation heat transfer*. CRC press, 2015.

[22] M. Planck, “On the Law of Distribution of Energy in the Normal Spectrum,” *Ann. Phys.*, vol. 4, no. 553, pp. 1–11, 1901.

[23] Crouch, C. H., Carey, J. E., Shen, M., Mazur, E., & Genin, F. Y. (2004). Infrared absorption by sulfur-doped silicon formed by femtosecond laser irradiation. Applied Physics A, 79(7), 1635 - 1641.

[24] Carey, J. E., Crouch, C. H., Shen, M., & Mazur, E. (2005). Visible and near-infrared responsivity of femtosecond-laser microstructured silicon photodiodes. *Optics letters*, *30*(14), 1773-1775.

[25] Torres, R., Itina, T. E., Vervisch, V., Halbwax, M., Derrien, T., Sarnet, T., ... & Roux, L. (2010, October). Study On Laser-Induced Periodic Structures And Photovoltaic Application. In *AIP Conference Proceedings* (Vol. 1278, No. 1, pp. 576-581). American Institute of Physics.

[26] Stewart, A. G., Greene-O'Sullivan, E., Herbert, D. J., Saveliev, V., Quinlan, F., Wall, L., ... & Jackson, J. C. (2006, February). Study of the properties of new SPM detectors. In *Semiconductor Photodetectors III* (Vol. 6119, p. 61190A). International Society for Optics and Photonics.

[27] Carey, J. E., & Mazur, E. (2004, May). High sensitivity silicon-based VIS/NIR photodetectors. In *Conference on Lasers and Electro-Optics, 2004.(CLEO).* (Vol. 2, pp. 2-pp). IEEE.

[28] Huang, Z., Carey, J. E., Liu, M., Guo, X., Mazur, E., & Campbell, J. C. (2006). Microstructured silicon photodetector. *Applied Physics Letters*, *89*(3), 033506.

[29] Wu, C., Crouch, C. H., Zhao, L., Carey, J. E., Younkin, R., Levinson, J. A., ... & Karger, A. (2001). Near-unity below-band-gap absorption by microstructured silicon. *Applied Physics Letters*, *78*(13), 1850-1852.

[30] Lv, J., Zhang, T., Zhang, P., Zhao, Y., & Li, S. (2018). Review application of nanostructured black silicon. *Nanoscale research letters*, *13*(1), 1-10.

[31] Liu, X., Coxon, P. R., Peters, M., Hoex, B., Cole, J. M., & Fray, D. J. (2014). Black silicon: fabrication methods, properties and solar energy applications. *Energy & Environmental Science*, *7*(10), 3223-3263.

[32] Otto, M., Algasinger, M., Branz, H., Gesemann, B., Gimpel, T., Füchsel, K., ... & Naumann, V. (2015). Black silicon photovoltaics. *Advanced optical materials*, *3*(2), 147-164.

[33] Chattopadhyay, S., Huang, Y. F., Jen, Y. J., Ganguly, A., Chen, K. H., & Chen, L. C. (2010). Anti-reflecting and photonic nanostructures. *Materials Science and Engineering: R: Reports*, *69*(1-3), 1-35.

[34] Priolo, F., Gregorkiewicz, T., Galli, M., & Krauss, T. F. (2014). Silicon nanostructures for photonics and photovoltaics. *Nature nanotechnology*, *9*(1), 19.

[35] Soplaki E. and Palyvos J., (2009). "On the temperature dependence of photovoltaic module electrical performance: a review of efficiency/power correlations". *Sol Energy* 83, 614-624.

[36] Family, R., & Mengüç, M. P. (2017). Materials for radiative cooling: a review. *Procedia environmental sciences*, *38*, 752-759.

[37] Catalanotti, S., Cuomo, V., Piro, G., Ruggi, D., Silvestrini, V., & Troise, G. (1975). "The radiative cooling of selective surfaces". *Solar Energy*, *17*(2), 83–89.

[38] Granqvist, C.G. and Hjortssberg, A. (1980). "Surfaces for radiative cooling: Silicon monoxide films on aluminum". Applied Physics Letters, 36, 139- 141.

[39] Granqvist, C. G. and Hjortsberg, A., (1981). "Radiative cooling to low temperatures: General considerations and application to selectively emitting SiO films". *Journal of Applied Physics*, 52, 4205-4220.

[40] Berdahl, P., Martin, M., & Sakkal, F. (1983). "Thermal performance of radiative cooling panels". *International Journal of Heat and Mass Transfer*, *26*(6), 871–880.

[41] Orel, B., Gunde, M. K., & Krainer, A. (1993). "Radiative cooling efficiency of white pigmented paints". *Solar Energy*, *50*(6), 477–482.

[42] Chetan N. Suryawanshi and Chhiu-Tsu Lin, (2009). "Radiative Cooling: Lattice Quantization and Surface Emissivity in Thin Coatings". *ACS Applied Materials & Interfaces*, 1(6), 1334-1338.

[43] A.R. Gentle and G. B. Smith, (2010). “Radiative Heat Pumping from the Earth Using Surface Phonon Resonance Nanoparticles”. *Nano Letters*, 10(2), 373-379.

[44] Kou, J. L., Jurado, Z., Chen, Z., Fan, S., & Minnich, A. J. (2017). Daytime radiative cooling using near-black infrared emitters. *Acs Photonics*, *4*(3), 626-630.

[45] Hu, M., Pei, G., Wang, Q., Li, J., Wang, Y., & Ji, J. (2016). Field test and preliminary analysis of a combined diurnal solar heating and nocturnal radiative cooling system. *Applied energy*, *179*, 899-908.

[46] Granqvist, C. G. (1981). Radiative heating and cooling with spectrally selective surfaces. *Applied Optics*, *20*(15), 2606-2615.

[47] Granqvist, C. G., Hjortsberg, A., & Eriksson, T. S. (1982). Radiative cooling to low temperatures with selectivity IR-emitting surfaces. *Thin Solid Films*, *90*(2), 187-190.

[48] Eriksson, T. S., Lushiku, E. M., & Granqvist, C. G. (1984). Materials for radiative cooling to low temperature. *Solar energy materials*, *11*(3), 149-161.

[49] Bao, H., Yan, C., Wang, B., Fang, X., Zhao, C. Y., & Ruan, X. (2017). Double-layer nanoparticle-based coatings for efficient terrestrial radiative cooling. *Solar Energy Materials and Solar Cells*, *168*, 78-84.

[50] Huang, Z., & Ruan, X. (2017). Nanoparticle embedded double-layer coating for daytime radiative cooling. *International Journal of Heat and Mass Transfer*, *104*, 890-896.

[51] Zhai, Y., Ma, Y., David, S. N., Zhao, D., Lou, R., Tan, G., ... & Yin, X. (2017). Scalable-manufactured randomized glass-polymer hybrid metamaterial for daytime radiative cooling. *Science*, *355*(6329), 1062-1066.

[52] Gentle, A. R., & Smith, G. B. (2015). A subambient open roof surface under the Mid-Summer sun. *Advanced Science*, *2*(9), 1500119.

[53] Huang, Y., Pu, M., Zhao, Z., Li, X., Ma, X., & Luo, X. (2018). Broadband metamaterial as an “invisible” radiative cooling coat. *Optics Communications*, *407*, 204-207.

[54] Tikhonravov, A. V., Trubetskov, M. K., & DeBell, G. W. (1996). Application of the needle optimization technique to the design of optical coatings. *Applied optics*, *35*(28), 5493-5508.

[55] Tikhonravov, A. V., Trubetskov, M. K., & DeBell, G. W. (2007). Optical coating design approaches based on the needle optimization technique. *Applied optics*, *46*(5), 704-710.

[56] Boudet, T., Chaton, P., Herault, L., Gonon, G., Jouanet, L., & Keller, P. (1996). Thin-film designs by simulated annealing. *Applied optics*, *35*(31), 6219-6226.

[57] Li, L., Wang, Q. H., Li, D. H., & Peng, H. R. (2009). Jump method for optical thin film design. *Optics express*, *17*(19), 16920-16926.

[58] Zhu, L., Raman, A. P., & Fan, S. (2015). Radiative cooling of solar absorbers using a visibly transparent photonic crystal thermal blackbody. *Proceedings of the national academy of sciences*, *112*(40), 12282-12287.

[59] Wu, D., Liu, C., Xu, Z., Liu, Y., Yu, Z., Yu, L., ... & Ye, H. (2018). The design of ultra-broadband selective near-perfect absorber based on photonic structures to achieve near-ideal daytime radiative cooling. *Materials & Design*, *139*, 104-111.

[60] Hossain, M. M., Jia, B., & Gu, M. (2015). A metamaterial emitter for highly efficient radiative cooling. *Advanced Optical Materials*, *3*(8), 1047-1051.

[61] Zeyghami, M., Goswami, D. Y., & Stefanakos, E. (2018). A review of clear sky radiative cooling developments and applications in renewable power systems and passive building cooling. *Solar Energy Materials and Solar Cells*, *178*, 115-128.

[62] Vall, S., & Castell, A. (2017). Radiative cooling as low-grade energy source: A literature review. *Renewable and Sustainable Energy Reviews*, *77*, 803-820.

[63] Ko, B., Lee, D., Badloe, T., & Rho, J. (2019). Metamaterial-based radiative cooling: Towards energy-free all-day cooling. *Energies*, *12*(1), 89.

[64] Hossain, M. M., & Gu, M. (2016). Radiative cooling: principles, progress, and potentials. *Advanced Science*, *3*(7), 1500360.

[65] Bijarniya, J. P., Sarkar, J., & Maiti, P. (2020). Environmental effect on the performance of passive daytime photonic radiative cooling and building energy-saving potential. *Journal of Cleaner Production*, 123119.

[66] Li, W., Li, Y., & Shah, K. W. (2020). A materials perspective on radiative cooling structures for buildings. *Solar Energy*, *207*, 247-269.

[67] Chen, J., & Lu, L. (2020). Comprehensive evaluation of thermal and energy performance of radiative roof cooling in buildings. *Journal of Building Engineering*, 101631.

[68] Chen, L., Zhang, K., Ma, M., Tang, S., Li, F., & Niu, X. (2020, July). Sub-ambient radiative cooling and its application in buildings. In *Building Simulation* (pp. 1-25). Tsinghua University Press.

[69] Family, R., Celik, S., & Mengüç, M. P. Coupled heat transfer analysis and experiments to evaluate the radiative cooling potential of concrete and green roofs for buildings.

[70] Ishii, S., Dao, T. D., & Nagao, T. (2020). Radiative cooling for continuous thermoelectric power generation in day and night. *Applied Physics Letters*, *117*(1), 013901.

[71] Kumar, A., & Chowdhury, A. (2020). Effect of multilayer selective radiative anti-reflective coating on crystalline silicon photovoltaics for operating temperature reduction. *International Journal of Sustainable Energy*, 1-15.

[72] Kandeal, A. W., Thakur, A. K., Elkadeem, M. R., Elmorshedy, M. F., Ullah, Z., Sathyamurthy, R., & Sharshir, S. W. (2020). Photovoltaics performance improvement using different cooling methodologies: A State-of-Art Review. *Journal of Cleaner Production*, 122772.

[73] Shi, Y., Li, W., Raman, A., & Fan, S. (2017). Optimization of multilayer optical films with a memetic algorithm and mixed integer programming. *ACS Photonics*, *5*(3), 684-691.

[74] D. M. Van Wie, D. G. Drewry, D. E. King, and C. M. Hudson, “The hypersonic environment: required operating conditions and design challenges,” J. Mater. Sci., **39**(19), 5915-5924 (2004).

[75] T. H. Squire, and J. Marschall, “Material property requirements for analysis and design of UHTC components in hypersonic applications,” J. Eur. Ceram. Soc., **30**(11), 2239-2251 (2010).

[76] A. Mack, “Aerothermodynamic behaviour of a generic nosecap model including thermomechanical structural effects,” Aerospace science and technology, **11**(5), 386-395 (2007).

[77] E. A. Thornton, “Thermal structures for aerospace applications,” AIAA Education Series (1996).

[78] S. Molesky, C. J. Dewalt, and Z. Jacob, “High temperature epsilon-near-zero and epsilon-near-pole metamaterial emitters for thermophotovoltaics,” Opt. express, **21**(101), A96-A110 (2013).

[79] S. K. Leggett, T. G. Hawarden, M. J. Currie, A. J. Adamson, T. C. Carroll, T. H. Kerr, ... & T. Wold, “L′ and M′ standard stars for the Mauna Kea Observatories Near-Infrared system,” Monthly Notices of the Royal Astronomical Society *345*(1), 144-152 (2003).

[80] J. T. Rayner, D. W. Toomey, P. M. Onaka, A. J. Denault, W. E. Stahlberger, W.D. Vacca, ... & S. Wang, “SpeX: A Medium-Resolution 0.8–5.5 Micron Spectrograph and Imager for the NASA Infrared Telescope Facility,” Publications of the Astronomical Society of the Pacific, 115(805), 362 (2003).

[81] A. Rogalski, K. Chrzanowski, “Infrared devices and techniques (revision),” Metrology and Measurement Systems, 21(4), 565-618 (2014).

[82] A. C. Phillips, J. Miller, W. Brown, D. Hilyard, B. Dupraw, V. Wallace, D. Cowley, “Progress toward high-performance reflective and anti-reflection coatings for astronomical optics,” *Advanced Optical and Mechanical Technologies in Telescopes and Instrumentation*, Vol. 7018, p. 70185A, International Society for Optics and Photonics, (2008).

[83] S. K. Mishra, V. Kumar, S. K. Tiwari, T. Mishra, G. Angula, S. Adhikari, “Development and degradation behavior of protective multilayer coatings for aluminum reflectors for solar thermal applications,” *Thin Solid Films, 619*, 202-207, (2016).

[84] D. M. Fryauf, A. C. Phillips, N. P. Kobayashi, “Corrosion protection of silver-based telescope mirrors using evaporated anti-oxidation overlayers and aluminum oxide films by atomic layer deposition,” In Low-Dimensional Materials and Devices, Vol. 9924, p. 99240S International Society for Optics and Photonics, (2016).

[85] J. Sebag, T. Vucina, J. Andrew, D. Neill, G. Poczulp, “Mirror coatings for the Large Synoptic Survey Telescope: requirements and solutions,” In *59th* Annual Technical Conference Proceedings of the Society of Vacuum Coaters, (2016, May).

[86] D. M. Fryauf, A. C. Phillips, N. P. Kobayashi, “Corrosion barriers for silver-based telescope mirrors: comparative study of plasma-enhanced atomic layer deposition and

reactive evaporation of aluminum oxide," Journal of Astronomical Telescopes, Instruments, and Systems, 1(4), 044002, (2015).

[87] I. Celanovic, N. Jovanovic, J. Kassakian, "Two-dimensional tungsten photonic crystals as selective thermal emitters," *Applied Physics Letters*, *92*(19), 193101, (2008).

[88] I. Celanovic, D. Perreault, J. Kassakian, "Resonant-cavity enhanced thermal emission," *Physical Review B*, *72*(7), 075127, (2005).

[89] A. Bessiere, C. Marcel, M. Morcrette, J. M. Tarascon, V. Lucas, B. Viana, N. Baffier, "Flexible electrochromic reflectance device based on tungsten oxide for infrared emissivity control," Journal of applied physics, 91(3), 1589-1594, (2002).

[90] M. G. Hutchins, N. S. Butt, A. J. Topping, J. Gallego, P. Milne, D. Jeffrey, I. Brotherston, "Infrared reflectance modulation in tungsten oxide based electrochromic devices," *Electrochimica Acta*, *46*(13-14), 1983-1988, (2001).

[91] A. T. Mecherikunnel, and J. Richmond, "Spectral distribution of solar radiation," (1980).

[92] J. Le Gall, M. Olivier, and J. Greffet, "Experimental and theoretical study of reflection and coherent thermal emission by a SiC grating supporting a surface-phonon polariton," Phys. Rev. B, **55**, 10105 (1997).

[93] J.-J. Greffet, R. Carminati, K. Joulain, J.-P. Mulet, S. Mainguy, Y. Chen, "Coherent emission of light by thermal sources," Nature, **416**, 61-64 (2002).

[94] C. Luo, A. Narayanaswamy, G. Chen, and J. D. Joannopoulos, "Thermal radiation from photonic crystals: A direct calculation," Phys. Rev. Lett. **93**, 213905 (2004).

[95] E. Rephaeli, S. Fan, "Tungsten black absorber for solar light with wide angular operation range," Appl. Phys. Lett. **92**, 211107 (2008).

[96] S. Zhang, Y. Li, G. Feng, B. Zhu, S. Xiao, L. Zhou, L. Zhao, "Strong infrared absorber: surface-microstructered Au film replicated from back silicon," Opt. Express, **19**, 20462-20467 (2011).

[97] I. Benkò, "High infrared emissivity coating for energy conservation and protection of inner surfaces in furnaces," International Journal of Global Energy Issues, **17**(1-2), 60-67 (2002).

[98] D. B. Mahadik, S. Gujjar, G. M. Gouda, and H. C. Barshilia, "Double layer SiO2/Al2O3 high emissivity coatings on stainless steel substrates using simple spray deposition system," Applied Surface Science, **299**, 6-11 (2014).

[99] X. He, Y. Li, L. Wang, Y. Sun, and S. Zhang, "High emissivity coatings for high temperature application: progress and prospect," Thin Solid Films, **517**(17), 5120-5129, (2009).

[100] Z. Chen, L. Zhu, A. Raman, and S. Fan, "Radiative cooling to deep sub-freezing temperatures through a 24-h day–night cycle," Nature communications, **7** (2016).

[101] C. E. Kennedy, R. V. Smilgys, D. A. Kirkpatrick, and J. S. Ross, "Optical performance and durability of solar reflectors protected by an alumina coating," Thin Solid Films, **304**(1-2), 303-309 (1997).

[102] C. E. Kennedy, and K. Terwilliger, "Optical durability of candidate solar reflectors," in *ASME 2004 International Solar Energy Conference*, pp. 597-606.

[103] U. Guler, A. Boltasseva, and V. M. Shalaev, "Refractory plasmonics," Science, **344**(6181), 263-264 (2014).

[104] H. Song, L. Guo, Z. Liu, K. Liu, X. Zeng, D. Ji, N. Zhang, H. Hu, S. Jiang, and Q. Gan, "Nanocavity enhancement for ultra-thin film optical absorber," Advanced Materials, **26**(17), 2737-2743 (2014).

[105] R. W. Philips, T. Mayer, and G.S. Ash, *U.S. Patent No. 5,084,351*. Washington, DC: U.S. Patent and Trademark Office (1992).

[106] B. J. Chun, C. K. Hwangbo, and J. S. Kim, "Optical monitoring of nonquarterwave layers of dielectric multilayer filters using optical admittance," Opt. Express, **14**(6), 2473-2480 (2006).

[107] Pralle, M. U., Carey, J. E., Homayoon, H., Alie, S., Sickler, J., Li, X., ... & McKee, J. (2010, May). Black silicon enhanced photodetectors: a path to IR CMOS. In *Infrared Technology and Applications XXXVI* (Vol. 7660, p. 76600N). International Society for Optics and Photonics.

[108] Halbwax, M., Sarnet, T., Delaporte, P., Sentis, M., Etienne, H., Torregrosa, F., ... & Martinuzzi, S. (2008). Micro and nano-structuration of silicon by femtosecond laser: application to silicon photovoltaic cells fabrication. *Thin solid films*, *516*(20), 6791-6795.

[109] Yuan, H. C., Yost, V. E., Page, M. R., Roybal, L., To, B., Stradins, P., ... & Branz, H. M. (2009, June). Efficient black silicon solar cells with nanoporous anti-reflection made in a single-step liquid etch. In *2009 34th IEEE Photovoltaic Specialists Conference (PVSC)* (pp. 000141-000145). IEEE.

[110] Yuan, H. C., Yost, V. E., Page, M. R., Stradins, P., Meier, D. L., & Branz, H. M. (2009). Efficient black silicon solar cell with a density-graded nanoporous surface: Optical properties, performance limitations, and design rules. *Applied Physics Letters*, *95*(12), 123501.

[111] Hu, L., & Chen, G. (2007). Analysis of optical absorption in silicon nanowire arrays for photovoltaic applications. *Nano letters*, *7*(11), 3249-3252.

[112] Wang, W., Wu, S., Reinhardt, K., Lu, Y., & Chen, S. (2010). Broadband light absorption enhancement in thin-film silicon solar cells. *Nano letters*, *10*(6), 2012-2018.

[113] Wang, Y., Yang, L., Liu, Y., Mei, Z., Chen, W., Li, J., ... & Xiaolong, D. (2015). Maskless inverted pyramid texturization of silicon. *Scientific reports*, *5*, 10843.

[114] Gouda, A. M., Allam, N. K., & Swillam, M. A. (2017). Efficient fabrication methodology of wide angle black silicon for energy harvesting applications. *RSC advances*, *7*(43), 26974-26982.

[115] Koynov, S., Brandt, M. S., & Stutzmann, M. (2006). Black nonreflecting silicon surfaces for solar cells. *Applied physics letters*, *88*(20), 203107.

[116] Liu, Y., Lai, T., Li, H., Wang, Y., Mei, Z., Liang, H., ... & Du, X. (2012). Nanostructure formation and passivation of large-area black silicon for solar cell applications. *Small*, *8*(9), 1392-1397.

[117] Yueh, S. H., Kwok, R., Li, F. K., Nghiem, S. V., Wilson, W. J., & Kong, J. A. (1994). Polarimetric passive remote sensing of ocean wind vectors. *Radio Science*, *29*(04), 799-814.

[118] Johnson, J. T., & Zhang, M. (1999). Theoretical study of the small slope approximation for ocean polarimetric thermal emission. *IEEE Transactions on Geoscience and Remote Sensing*, *37*(5), 2305-2316.

[119] Sendur, I. K., Johnson, J. T., & Baertlein, B. A. (2001, October). Analysis of polarimetric IR phenomena for detection of surface mines. In *Detection and Remediation Technologies for Mines and Minelike Targets VI* (Vol. 4394, pp. 153-163). International Society for Optics and Photonics.

[120] Oh, Y., Sarabandi, K., & Ulaby, F. T. (1992). An empirical model and an inversion technique for radar scattering from bare soil surfaces. *IEEE transactions on Geoscience and Remote Sensing*, *30*(2), 370-381.

[121] Zheng, L., Ma, Y., Chu, S., Wang, S., Qu, B., Xiao, L., ... & Hou, X. (2014). Improved light absorption and charge transport for perovskite solar cells with rough interfaces by sequential deposition. *Nanoscale*, *6*(14), 8171-8176.

[122] Faÿ, S., Feitknecht, L., Schlüchter, R., Kroll, U., Vallat-Sauvain, E., & Shah, A. (2006). Rough ZnO layers by LP-CVD process and their effect in improving performances of amorphous and microcrystalline silicon solar cells. *Solar Energy Materials and Solar Cells*, *90*(18-19), 2960-2967.

[123] Raether, H. (1988). Surface plasmons on smooth surfaces. In *Surface plasmons on smooth and rough surfaces and on gratings* (pp. 4-39). Springer, Berlin, Heidelberg.

[124] Hoffmann, A., Lenkefi, Z., & Szentirmay, Z. (1998). Effect of roughness on surface plasmon scattering in gold films. *Journal of physics: Condensed matter*, *10*(24), 5503.

[125] Farias, G. A., & Maradudin, A. A. (1983). Surface plasmons on a randomly rough surface. *Physical Review B*, *28*(10), 5675.

[126] Liu, Z., Liu, H., Wang, X., Yang, H., & Gao, J. (2017). Large area and broadband ultra-black absorber using microstructured aluminum doped silicon films. *Scientific reports*, *7*, 42750.

[127] Gorgulu, K., Gok, A., Yilmaz, M., Topalli, K., Bıyıklı, N., & Okyay, A. K. (2016). All-silicon ultra-broadband infrared light absorbers. *Scientific reports*, *6*, 38589.

[128] Chen, Y. B., & Zhang, Z. M. (2008). Heavily doped silicon complex gratings as wavelength-selective absorbing surfaces. *Journal of Physics D: Applied Physics*, *41*(9), 095406.

[129] Marquier, F., Joulain, K., Mulet, J. P., Carminati, R., & Greffet, J. J. (2004). Engineering infrared emission properties of silicon in the near field and the far field. *Optics communications*, *237*(4-6), 379-388.

[130] Bouchon, P., Koechlin, C., Pardo, F., Haïdar, R., & Pelouard, J. L. (2012). Wideband omnidirectional infrared absorber with a patchwork of plasmonic nanoantennas. *Optics letters*, *37*(6), 1038-1040.

[131] Cui, Y., Fung, K. H., Xu, J., Ma, H., Jin, Y., He, S., & Fang, N. X. (2012). Ultrabroadband light absorption by a sawtooth anisotropic metamaterial slab. *Nano letters*, *12*(3), 1443-1447.

[132] Zhou, J., Kaplan, A. F., Chen, L., & Guo, L. J. (2014). Experiment and theory of the broadband absorption by a tapered hyperbolic metamaterial array. *ACS photonics*, *1*(7), 618-624.

[133] Akhter, P., Huang, M., Kadakia, N., Spratt, W., Malladi, G., & Bakhru, H. (2014). Suppressing light reflection from polycrystalline silicon thin films through surface texturing and silver nanostructures. *Journal of Applied Physics*, *116*(11), 113503.

[134] Boroumand, J., Das, S., Vázquez-Guardado, A., Franklin, D., & Chanda, D. (2016). Unified electromagnetic-electronic design of light trapping silicon solar cells. *Scientific reports*, *6*, 31013.

[135] Chen, Z. H., Qiao, N., Yang, Y., Ye, H., Liu, S., Wang, W., & Wang, Y. (2015). Enhanced broadband electromagnetic absorption in silicon film with photonic crystal surface and random gold grooves reflector. *Scientific reports*, *5*(1), 1-8.

[136] Gorgulu, K., Yilmaz, M., Topalli, K., & Okyay, A. K. (2017). Wideband 'black silicon'for mid-infrared applications. *Journal of Optics*, *19*(6), 065101.

[137] Wang, K. X., Yu, Z., Liu, V., Cui, Y., & Fan, S. (2012). Absorption enhancement in ultrathin crystalline silicon solar cells with antireflection and light-trapping nanocone gratings. *Nano letters*, *12*(3), 1616-1619.

[138] Bermel, P., Boriskina, S. V., Yu, Z., & Joulain, K. (2015). Control of radiative processes for energy conversion and harvesting. Optics Express, 23(24), A1533-A1540.

[139] Li, W., & Fan, S. (2018). Nanophotonic control of thermal radiation for energy applications. Optics express, 26(12), 15995-16021.

[140] Qu, Y., Li, Q., Cai, L., Pan, M., Ghosh, P., Du, K., & Qiu, M. (2018). Thermal camouflage based on the phase-changing material GST. Light: Science & Applications, 7(1), 1-10.

[141] Salihoglu, O., Uzlu, H. B., Yakar, O., Aas, S., Balci, O., Kakenov, N., ... & Kocabas, C. (2018). Graphene-based adaptive thermal camouflage. Nano letters, 18(7), 4541-4548.

[142] Karker, N., Dharmalingam, G., & Carpenter, M. A. (2014). Thermal energy harvesting plasmonic based chemical sensors. ACS nano, 8(10), 10953-10962.

[143] Argyropoulos, C., Le, K. Q., Mattiucci, N., D'Aguanno, G., & Alu, A. (2013). Broadband absorbers and selective emitters based on plasmonic Brewster metasurfaces. Physical Review B, 87(20), 205112.

[144] Cong, J., Zhou, Z., Yun, B., Lv, L., Yao, H., Fu, Y., & Ren, N. (2016). Broadband visible-light absorber via hybridization of propagating surface plasmon. Optics Letters, 41(9), 1965-1968.

[145] Liu, X., Tyler, T., Starr, T., Starr, A. F., Jokerst, N. M., & Padilla, W. J. (2011). Taming the blackbody with infrared metamaterials as selective thermal emitters. Physical review letters, 107(4), 045901.

[146] Liu, B., & Shen, S. (2013). Broadband near-field radiative thermal emitter/absorber based on hyperbolic metamaterials: Direct numerical simulation by the Wiener chaos expansion method. Physical Review B, 87(11), 115403.

[147] Ji, D., Song, H., Zeng, X., Hu, H., Liu, K., Zhang, N., & Gan, Q. (2014). Broadband absorption engineering of hyperbolic metafilm patterns. Scientific reports, 4, 4498.

[148] Rinnerbauer, V., Shen, Y., Joannopoulos, J. D., Soljačić, M., Schäffler, F., & Celanovic, I. (2014). Superlattice photonic crystal as broadband solar absorber for high temperature operation. Optics express, 22(107), A1895-A1906.

[149] Rinnerbauer, V., Ndao, S., Yeng, Y. X., Chan, W. R., Senkevich, J. J., Joannopoulos, J. D., ... & Celanovic, I. (2012). Recent developments in high-temperature photonic crystals for energy conversion. Energy & Environmental Science, 5(10), 8815-8823.

[150] Gan, Q., Fu, Z., Ding, Y. J., & Bartoli, F. J. (2008). Ultrawide-bandwidth slow-light system based on THz plasmonic graded metallic grating structures. Physical review letters, 100(25), 256803.

[151] Ko, H., Ko, D. H., Cho, Y., & Han, I. K. (2014). Broadband light absorption using a multilayered gap surface plasmon resonator. Applied Physics A, 116(3), 857-861.

[152] Cheng, C. W., Abbas, M. N., Chiu, C. W., Lai, K. T., Shih, M. H., & Chang, Y. C. (2012). Wide-angle polarization independent infrared broadband absorbers based on metallic multi-sized disk arrays. Optics express, 20(9), 10376-10381.

[153] Li, J., Gan, R., Guo, Q., Liu, H., Xu, J., & Yi, F. (2018). Tailoring optical responses of infrared plasmonic metamaterial absorbers by optical phonons. Optics express, 26(13), 16769-16781.

[154] Subramania, G., Fischer, A. J., & Luk, T. S. (2012). Optical properties of metal-dielectric based epsilon near zero metamaterials. Applied Physics Letters, 101(24), 241107.

[155] Vercruysse, D., Sapra, N. V., Su, L., & Vuckovic, J. (2019). Dispersion engineering with photonic inverse design. *IEEE Journal of Selected Topics in Quantum Electronics*, *26*(2), 1-6.

[156] Molesky, S., Lin, Z., Piggott, A. Y., Jin, W., Vucković, J., & Rodriguez, A. W. (2018). Inverse design in nanophotonics. *Nature Photonics*, *12*(11), 659-670.

[157] Hakansson, A., Sánchez-Dehesa, J., & Sanchis, L. (2005). Inverse design of photonic crystal devices. *IEEE Journal on selected areas in communications*, *23*(7), 1365-1371.

[158] Kim, G., Domínguez-Caballero, J. A., & Menon, R. (2012). Design and analysis of multi-wavelength diffractive optics. *Optics express*, *20*(3), 2814-2823.

[159] Shokooh-Saremi, M., & Magnusson, R. (2007). Particle swarm optimization and its application to the design of diffraction grating filters. *Optics letters*, *32*(8), 894-896.

[160] Johnson, E. G., & Abushagur, M. A. (1995). Microgenetic-algorithm optimization methods applied to dielectric gratings. *JOSA A*, *12*(5), 1152-1160.

[161] Miller, O. D. (2013). Photonic design: From fundamental solar cell physics to computational inverse design. *arXiv preprint arXiv:1308.0212*.

[162] Niederberger, A. C., Fattal, D. A., Gauger, N. R., Fan, S., & Beausoleil, R. G. (2014). Sensitivity analysis and optimization of sub-wavelength optical gratings using adjoints. *Optics express*, *22*(11), 12971-12981.

[163] Wang, J., Shi, Y., Hughes, T., Zhao, Z., & Fan, S. (2018). Adjoint-based optimization of active nanophotonic devices. *Optics express*, *26*(3), 3236-3248.

[164] Michaels, A., & Yablonovitch, E. (2018). Inverse design of near unity efficiency perfectly vertical grating couplers. *Optics express*, *26*(4), 4766-4779.

[165] Sapra, N. V., Vercruysse, D., Su, L., Yang, K. Y., Skarda, J., Piggott, A. Y., & Vučković, J. (2019). Inverse design and demonstration of broadband grating couplers. *IEEE Journal of Selected Topics in Quantum Electronics*, *25*(3), 1-7.

[166] Jin, W., Molesky, S., Lin, Z., Fu, K. M. C., & Rodriguez, A. W. (2018). Inverse design of compact multimode cavity couplers. *Optics express*, *26*(20), 26713-26721.

[167] Xiao, T. P., Cifci, O. S., Bhargava, S., Chen, H., Gissibl, T., Zhou, W., ... & Braun, P. V. (2016). Diffractive spectral-splitting optical element designed by adjoint-based electromagnetic optimization and fabricated by femtosecond 3D direct laser writing. *ACS Photonics*, *3*(5), 886-894.

[168] Sitawarin, C., Jin, W., Lin, Z., & Rodriguez, A. W. (2018). Inverse-designed photonic fibers and metasurfaces for nonlinear frequency conversion. *Photonics Research*, *6*(5), B82-B89.

[169] Hughes, T. W., Minkov, M., Williamson, I. A., & Fan, S. (2018). Adjoint method and inverse design for nonlinear nanophotonic devices. *ACS Photonics*, *5*(12), 4781-4787.

[170] Yeng, Y. X., Ghebrebrhan, M., Bermel, P., Chan, W. R., Joannopoulos, J. D., Soljačić, M., & Celanovic, I. (2012). Enabling high-temperature nanophotonics for energy applications. Proceedings of the National Academy of Sciences, 109(7), 2280-2285.

[171] Deng, H., Li, Z., Stan, L., Rosenmann, D., Czaplewski, D., Gao, J., & Yang, X. (2015). Broadband perfect absorber based on one ultrathin layer of refractory metal. Optics letters, 40(11), 2592-2595.

[172] , M., Roberts, A. S., Ding, F., Wang, D., Kristensen, P. K., Bozhevolnyi, S. I., & Pedersen, K. (2016). Multilayer tungsten-alumina-based broadband light absorbers for high-temperature applications. Optical Materials Express, 6(8), 2704-2714.

[173] Li, W., Guler, U., Kinsey, N., Naik, G. V., Boltasseva, A., Guan, J., ... & Kildishev, A. V. (2014). Refractory plasmonics with titanium nitride: broadband metamaterial absorber. Advanced Materials, 26(47), 7959-7965.

[174] Zimmermann, J. W., Hilmas, G. E., Fahrenholtz, W. G., Dinwiddie, R. B., Porter, W. D., & Wang, H. (2008). Thermophysical properties of ZrB2 and ZrB2–SiC ceramics. Journal of the American Ceramic Society, 91(5), 1405-1411.

[175] Monteverde, F. (2005). The thermal stability in air of hot-pressed diboride matrix composites for uses at ultra-high temperatures. Corrosion science, 47(8), 2020-2033.

[176] Wang, F., Cheng, L., Xie, Y., Jian, J., & Zhang, L. (2015). Effects of SiC shape and oxidation on the infrared emissivity properties of ZrB2–SiC ceramics. Journal of Alloys and Compounds, 625, 1-7.

[177] Tan, W., Petorak, C. A., & Trice, R. W. (2014). Rare-earth modified zirconium diboride high emissivity coatings for hypersonic applications. Journal of the European Ceramic Society, 34(1), 1-11.

[178] Tan, W., Adducci, M., Petorak, C., Thompson, B., Brenner, A. E., & Trice, R. W. (2016). Effect of rare-earth dopant (Sm) concentration on total hemispherical emissivity and ablation resistance of ZrB2/SiC coatings. Journal of the European Ceramic Society, 36(16), 3833-3841.

[179] Sichkar, S. M., Antonov, V. N., & Antropov, V. P. (2013). Comparative study of the electronic structure, phonon spectra, and electron-phonon interaction of ZrB 2 and TiB 2. Physical Review B, 87(6), 064305.

[180] Razavi, B., & Behzad, R. (1998). *RF microelectronics* (Vol. 1). Prentice Hall, New Jersey, USA.

[181] Balanis, C. A. (1992). Antenna theory: A review. *Proceedings of the IEEE*, *80*(1), 7-23.

[182] Pues, H. F., & Van De Capelle, A. R. (1989). An impedance-matching technique for increasing the bandwidth of microstrip antennas. *IEEE transactions on antennas and propagation*, *37*(11), 1345-1354.

[183] Marrocco, G. (2008). The art of UHF RFID antenna design: Impedance-matching and size-reduction techniques. *IEEE antennas and propagation magazine*, *50*(1).

[184] Kats, M. A., Sharma, D., Lin, J., Genevet, P., Blanchard, R., Yang, Z., ... & Capasso, F. (2012). Ultra-thin perfect absorber employing a tunable phase change material. Applied Physics Letters, 101(22), 221101.

[185] Kats, M. A., Byrnes, S. J., Blanchard, R., Kolle, M., Genevet, P., Aizenberg, J., & Capasso, F. (2013). Enhancement of absorption and color contrast in ultra-thin highly absorbing optical coatings. Applied Physics Letters, 103(10), 101104.

[186] Kats, M. A., Blanchard, R., Genevet, P., & Capasso, F. (2013). Nanometer optical coatings based on strong interference effects in highly absorbing media. Nature materials, 12(1), 20.

[187] Berk, A., Anderson, G. P., Acharya, P. K., Bernstein, L. S., Muratov, L., Lee, J., ... & Lockwood, R. B. (2006, May). MODTRAN5: 2006 update. In *Algorithms and Technologies for Multispectral, Hyperspectral, and Ultraspectral Imagery XII* (Vol. 6233, p. 62331F). International Society for Optics and Photonics..

[188] Palik, E. (1985). Handbook of Optical Constants of Solids (Academic Press Handbook Series, Elsevier Science & Tech).

[189] Siefke, T., Kroker, S., Pfeiffer, K., Puffky, O., Dietrich, K., Franta, D., ... & Tünnermann, A. (2016). Materials pushing the application limits of wire grid polarizers further into the deep ultraviolet spectral range. *Advanced Optical Materials*, *4*(11), 1780-1786.

[190] Czapla, B., Srinivasan, A., Yin, Q., & Narayanaswamy, A. (2017, October). Potential for passive radiative cooling by PDMS selective emitters. In *ASME 2017 Heat Transfer Summer Conference*. American Society of Mechanical Engineers Digital Collection.

[191] Zhou, L., Song, H., Liang, J., Singer, M., Zhou, M., Stegenburgs, E., ... & Ooi, B. (2019). A polydimethylsiloxane-coated metal structure for all-day radiative cooling. *Nature Sustainability*, *2*(8), 718-724.

[192] Gentle, A. R., & Smith, G. B. (2010, May). Optimized infra-red spectral response of surfaces for sub-ambient sky cooling as a function of humidity and operating temperature. In *Photonics for Solar Energy Systems III* (Vol. 7725, p. 77250Z). International Society for Optics and Photonics.

[193] Goldstein, E. A., Nasuta, D., Li, S., Martin, C., & Raman, A. (2018). Free Subcooling with the Sky: Improving the efficiency of air conditioning systems.

[194] H.A. Macleod, *Thin-film optical filters* (CRC press, 2001).

[195] O. Deparis, M. Rassart, C. Vandenbem, V. Welch, J.P. Vigneron, L. Dreesen, S. Lucas, "Dielectric multilayer films fabricated by magnetron sputtering: how far can the iridescence be tuned?" Plasma Processes and Polymers, 6(S1), (2009).

[196] K. N. Chopra, K. V. Narasimham, "Thin film coating design and fabrication of broadband dielectric coated laser mirror," Journal of optics, 17(2), 107, (1986).

[197] Ion Beam Deposition. (n.d.). Retrieved January 13, 2017, from http: //www.oxford-instruments.com/products/etching-deposition-and-growth/ plasma- etch- deposition/key-applications- for- ion- beam- deposition.

[198] A. J. Moses, "Refractive index of optical materials in the infrared region," (No. EPIC-DS-166). HUGHES AIRCRAFT CO CULVER CITY CA ELECTRONIC PROPERTIES INFORMATION CENTER, (1970).

[199] L. Wang, Z. Shen, G. Du, P. Wang, "The thermal stability of silver-based high reflectance coatings," Thin Solid Films, 616, 122-125, (2016).

[200] FDTD Solutions (Lumerical, 2016).

[201] Novotny, L. (2007). Effective wavelength scaling for optical antennas. Physical Review Letters, 98(26), 266802.

[202] Jacobs, T. D., Junge, T., & Pastewka, L. (2017). Quantitative characterization of surface topography using spectral analysis. Surface Topography: Metrology and Properties, 5(1), 013001.

[203] Cao, L., & Sendur, K. (2019). Surface Roughness Effects on the Broadband Reflection for Refractory Metals and Polar Dielectrics. Materials, 12(19), 3090.

[204] Pang, S. W., Rathman, D. D., Silversmith, D. J., Mountain, R. W., & DeGraff, P. D. (1983). Damage induced in Si by ion milling or reactive ion etching. Journal of applied physics, 54(6), 3272-3277.

[205] Fung, T. H., Veeken, T., Payne, D., Veettil, B., Polman, A., & Abbott, M. (2019). Application and validity of the effective medium approximation to the optical properties of nano-textured silicon coated with a dielectric layer. Optics Express, 27(26), 38645-38660.

[206] Elsayed, A. A., Sabry, Y. M., Khalil, D., Marty, F., & Bourouina, T. (2016, August). Optical diffuse reflectance of black silicon and its isotropicity. In 2016 URSI Asia-Pacific Radio Science Conference (URSI AP-RASC) (pp. 1944-1946). IEEE.

[207] Jaberansary, E., Masaud, T. M. B., Milosevic, M. M., Nedeljkovic, M., Mashanovich, G. Z., & Chong, H. M. (2013). Scattering loss estimation using 2-D Fourier analysis and modeling of sidewall roughness on optical waveguides. IEEE Photonics Journal, 5(3), 6601010-6601010.

[208] Masetti, G., Severi, M., & Solmi, S. (1983). Modeling of carrier mobility against carrier concentration in arsenic-, phosphorus-, and boron-doped silicon. IEEE Transactions on electron devices, 30(7), 764-769.

[209] Aydin, K., Ferry, V. E., Briggs, R. M., & Atwater, H. A. (2011). Broadband polarization-independent resonant light absorption using ultrathin plasmonic super absorbers. Nature communications, 2(1), 1-7.

[210] Milligan, T. Modern Antenna Design, 1985. McGraw-Hill, New York, 8-9.

[211] Wang, P., Zhao, H., Wang, X., Farrell, G., & Brambilla, G. (2018). A review of multimode interference in tapered optical fibers and related applications. Sensors, 18(3), 858.

[212] Lalau-Keraly, C. M., Bhargava, S., Miller, O. D., & Yablonovitch, E. (2013). Adjoint shape optimization applied to electromagnetic design. Optics express, 21(18), 21693-21701.

[213] O. D. Miller, PhD thesis (2012), University of California at Berkeley, http://optoelectronics.eecs.berkeley.edu/ThesisOwenMiller.pdf

[214] Smith, D. R., Vier, D. C., Koschny, T., & Soukoulis, C. M. (2005). Electromagnetic parameter retrieval from inhomogeneous metamaterials. Physical review E, 71(3), 036617.